Computational Modeling and Design of Multilayer Corrosion Coatings for Galvanic Protection of Steel

by

Samuel R. Cross

B.A. Physics and Math, Harvard University (2008)

Submitted to the Department of Materials Science and Engineering in Partial Fulfillment of the Requirements for the Degree of

Doctor of Philosophy in Materials Science and Engineering

at the

Massachusetts Institute of Technology

February 2016

Author .... Signature redacted

Department of Materials Science and Engineering
November 24, 2015

Certified by .... Signature redacted

Christopher A. Schuh
Department Head, Danae and Vasilios Salapatas Professor of Metallurgy
Thesis Supervisor

Accepted by .... Signature redacted ....

Donald R. Sadoway
Chair, Departmental Committee on Graduate Students

Computational Modeling and Design of Multilayer Corrosion Coatings for Galvanic Protection of Steel

Samuel R. Cross

Submitted to the Department of Materials Science and Engineering on November 24, 2015, in partial fulfillment of the requirements for the degree of Doctor of Philosophy in Materials Science and Engineering

Abstract

Steels represent an economically vital class of alloys for use in structural applications, due to low cost and high strength and toughness, but often suffer from high susceptibility to corrosion in relevant environments. Use of metallic coatings, particularly zinc alloys, has long been a widely employed method for corrosion protection of steel, by acting both as a physical barrier to the aggressive environment, and providing sacrificial protection due to the preferential dissolution of the coating. Recent advances in processing techniques has permitted the efficient deposition of multilayer metallic coatings, which offer tremendous potential for dramatic improvements in performance relative to single layer coatings. However, development of multilayer corrosion coatings is hampered by a number of obstacles, in particular the lack of theoretical or computational tools to predict the corrosion behavior of multilayer coating structures. While existing numerical models for corrosion are well validated for simple geometries and short timescales, there are no models with demonstrated ability to be applied to composite materials such as multilayer coatings, or to incorporate the effects of corrosion damage over time on the effectiveness of the coating. This thesis seeks to address this deficiency through development and validation of two corrosion modeling techniques. The first modeling technique uses standard techniques for numerical modeling of galvanic corrosion to produce time-dependent corrosion simulations for multilayer or compositionally graded coatings, under the assumptions of completely generalized corrosion. The second modeling technique attempts to capture the effect of localized corrosion on multilayer coatings by treating the coating material as a porous electrode with properties calculated through an effective medium approximation. The output of the corrosion models is validated through comparison to a number of quantitative and qualitative corrosion tests on a variety of coatings, and is demonstrated to accurately capture a wide range of phenomena relevant to corrosion of multilayer thin films. Finally, this thesis demonstrates the potential application of the developed corrosion models as a design tool, by applying optimization techniques to determine coating configurations with maximized protective ability.

Thesis Supervisor: Christopher Schuh

Title: Department Head, Danae and Vasilios Salapatas Professor of Metallurgy

Acknowledgements

This thesis was only possible with the generous support of many people both inside and outside of MIT. I would first like to thank the members of my thesis committee, Professor Michael Demkowicz and Professor Ronald Ballinger, for their advice and suggestions regarding this research. I am also enormously indebted to the technical staff at MIT, whose hard work maintaining equipment and providing technical assistance has been essential in enabling the experiments presented in this thesis. I am particularly grateful to Tim McClure, Shiahn Chen, Don Galler, Mike Tarkanian, Ike Feitler, Dr. Charlie Settens, and Dr. Steven Kooi, among many others, for their individual help overcoming various technical challenges over the course of my project. I am also grateful to a large number of other members of the MIT community who have helped me with the administrative aspects of my project, in particular Jazy Ma, Diane Johansen, Angelita Mireles, and Elissa Havarty.

I am also deeply grateful to my friends and family, for their love and support throughout the course of my MIT. I particularly like to express my thanks and love for my fiancée Lee Sullivan, for his unwavering encouragement and love throughout all of the day to day concerns of graduate school life. My sister Emily and my parents Liz and Fred have also been my tireless cheerleaders for my entire life, and I deeply appreciate all of the love and support they have given me over the years. I would also like to thank the many people who have made MIT a friendly home to me these last few years, in particularly the other members of the Schuh research group, who have been a constant source of entertainment, advice, and support.

The work presented in this thesis was funded by the BP-MIT Materials and Corrosion Center. A number of people at BP were instrumental in supporting this project through their advice and technical expertise in corrosion engineering. I am particularly grateful to Sai Venkateswaran, Richard Woollam, and Steven Shademan for their insightful comments and advice on this project.

Last but not least, I would like to thank my advisor Professor Chris Schuh for his tireless encouragement and insightful advice. Not only has Chris been a vital source of guidance on my project; he has also encouraged me to have the confidence and autonomy to tackle big

challenges, both in science and in life. Chris has been a hugely positive influence in shaping my experience at MIT, and I am deeply grateful for his mentorship and support in guiding my research, academic work, and career path throughout my time at MIT.

Table of Contents

List of Figures

List of Tables

1. Introduction

Corrosion is the degradation of a metal or alloy through chemical reaction with its environment. In nature, metal atoms are almost exclusively found in an oxidized state within mineral ores, and processed into metals through addition of energy. As such, metals used in engineering are in a metastable state, and there may be a considerable driving force for chemical reactions that convert metals to either metal oxides or metal ions dissolved in a liquid electrolyte. While not strictly necessarily for corrosion to occur, the presence of a liquid electrolyte in contact with the metal surface is critically important for facilitating the charge transfer reactions that underlie the corrosion process, and so for this thesis we will assume that the metal under consideration is in contact with a liquid electrolyte.

We will first consider the most direct form of corrosion damage, which occurs through the oxidation of metal which is in contact with an aggressive liquid electrolyte. The oxidation occurs through metal dissolution reactions such as:

$$\mathrm{Zn(s)} \rightarrow \mathrm{Zn^{2+}(aq)} + 2e^{-}$$

$$\mathrm{Fe(s)} \rightarrow \mathrm{Fe^{2+}(aq)} + 2e^{-}$$

These dissolution reactions convert solid metal to metal ions dissolved in the electrolyte, and release electrons into the interior of the metal. The released electrons are consumed by reduction reactions on the surface of the metal, most commonly oxygen reduction and hydrogen evolution:

$$\mathrm{2H_2O + O_2(g) \rightarrow 4OH^{-}(aq) + 4e^{-}}$$

$$\mathrm{2H^{+}(aq) + 2e^{-} \rightarrow H_2(g)}$$

The rates of all of these redox reactions is determined by the chemistry of the metal surface, composition of the electrolyte, and the electrode potential E, which gives the potential difference between the metal and the adjacent electrolyte, relative to some reference potential. The rates of the oxidation reactions, also called anodic reactions, generally increase with increasing electrode potential, while the rates of the reduction or cathodic reactions generally decrease with increasing potential. The overall corrosion potential of the system, denoted by E_{corr}, is determined by the potential at which there is zero net interfacial current density.

1.1 Metallic coatings for corrosion protection

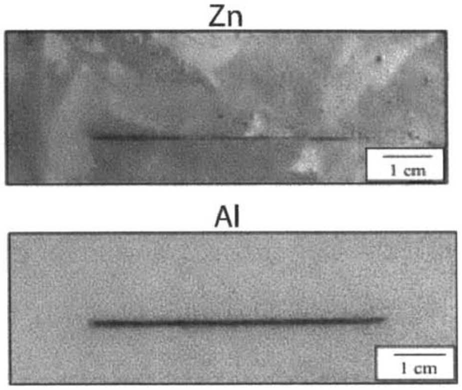

Figure 1.1 Scribed zinc and aluminum coatings on steel, following corrosion in mild atmospheric conditions [1]

In a large number of cases, it is not possible to use materials that are inherently corrosion resistant in the relevant environment, and so the use of surface treatments or coatings is necessary to achieve acceptable service life. The most widespread example of this is galvanized steel, in which mild steel, which has low cost and high strength but poor corrosion resistance, is coated in a layer of zinc, most commonly through a hot-dip method. Corrosion coatings such as these protect the substrate metal through two mechanisms. The first is barrier protection, in which the coating protects the base metal by preventing contact between the aggressive electrolyte and substrate. The second mechanism is cathodic or sacrificial protection, in which coating materials are used that are highly active, and oxidize preferentially relative to the substrate material. Cathodic protection can dramatically reduce corrosion damage to any substrate exposed to the environment, such as at a cut edge, but only does so by sacrificing the coating material in place of the substrate. The utility of cathodic protection is illustrated by the images in Figure 1.1, showing zinc and aluminum coatings on steel with a scribed scratch defect following a 24 month exposure in mild outdoor atmospheric conditions

[1]. The zinc coating readily provides cathodic protection to the steel exposed beneath the scratch, and so completely prevents the formation of visible rust. The aluminum coating, on the other hand, provides minimal cathodic protection, and so does not prevent rust from forming on exposed steel surfaces. However, the aluminum coating still acts as an effective barrier, preventing the spread of the visible rust beyond the scratched area.

Thus while providing cathodic protection is vitally important for the reliable performance of the coating, in order to reduce the overall corrosion rate, the coating materials must also have an inherently low corrosion rate. In the case of galvanized steel, for example, the total measured corrosion rate over the first year in a variety of atmospheric conditions was found by Natesan et. al. to range from 4 to 90 times slower than that of uncoated steel [7]. The reduction in corrosion rate for zinc relative to steel is largely due to the formation of a layer of zinc oxides and hyroxides on the surface, which act as an inert passive layer that significantly inhibits the rate of both metal dissolution and oxygen reduction. However, while the use of materials with high tendency to form passive surfaces is an effective strategy for decreasing the corrosion rate of the coating, it also decreases the ability of the coating to provide cathodic protection to the substrate. For instance, aluminum has a strong tendency to form a passive aluminum oxide surface, and so aluminum coatings typically have a much lower corrosion rate than zinc, but in many environments do not have sufficient anodic activity to provide cathodic protection to protect steel exposed at gaps in the coating [1,8,9]. Thus, one promising avenue for development of corrosion coatings with improved performance is through multilayer or composite coating structures, in which the cathodic protection can be provided by some layers, while other layers provide barrier protection to increase the overall lifetime of the coating.

1.2 Multilayer corrosion coatings

1.2.1 Synthesis of multilayer coatings

While there is a great variety of methods for synthesis of multilayer coatings, most techniques that promise the ability to produce a significant range of well-controlled multilayer coatings fall in two broad categories, vapor deposition and electrodeposition. Multilayer coatings produced by vacuum processes such as physical vapor deposition, or sputtering with multiple targets or controlled gas input can produce compact, adhesive coatings with layers of precisely controlled composition [2,10–14], such as the multilayer Ti/CrN coating shown in Figure 1.2 (a). However, while vapor deposited coatings often have very high quality and corrosion resistance, due to the high cost and low speed of vapor deposition, use of PVD coatings is generally limited to thin, barrier-type coatings [15]; due to the low total amount of material contained in vapor deposited coatings, they are less effective at providing sustained cathodic protection.

Electrodeposition, on the other hand, allows relatively fast and inexpensive synthesis of multilayer coatings, through reduction of metal ions from an electrodeposition bath. Generally, multilayer coatings produced through electrodeposition are produced through either a single bath technique [4,16–22], in which the composition is modulated by variation of the applied potential or deposition current density over time, or dual bath techniques , in which different layers are produced by physically moving the sample between different baths. For instance, Fei and Wilcox synthesized the Zn/Ni multilayer shown in Figure 1.2 (b) through dual bath electrodeposition, finding that they could generate coherent and distinct layers as small as 1 μm. Single bath electrodeposition, on the other hand, has significant advantages in terms of low cost, scalability, and decreased chance of inter-layer defects. For instance, Cai and Schuh used single bath electrodeposition to synthesize the multilayer Al-Mn coating shown in Figure 1.2 (c) [4]; unlike in the dual bath approach, single bath electrodeposition generally allows deposition of arbitrarily thin layers [4,23]. However, the use of a single bath also limits the composition of each layer to the range of alloys that can be codeposited from a single solution, generally restricting use to alloys in which all metals have similar reduction potential, and for which a modest range of composition is acceptable.

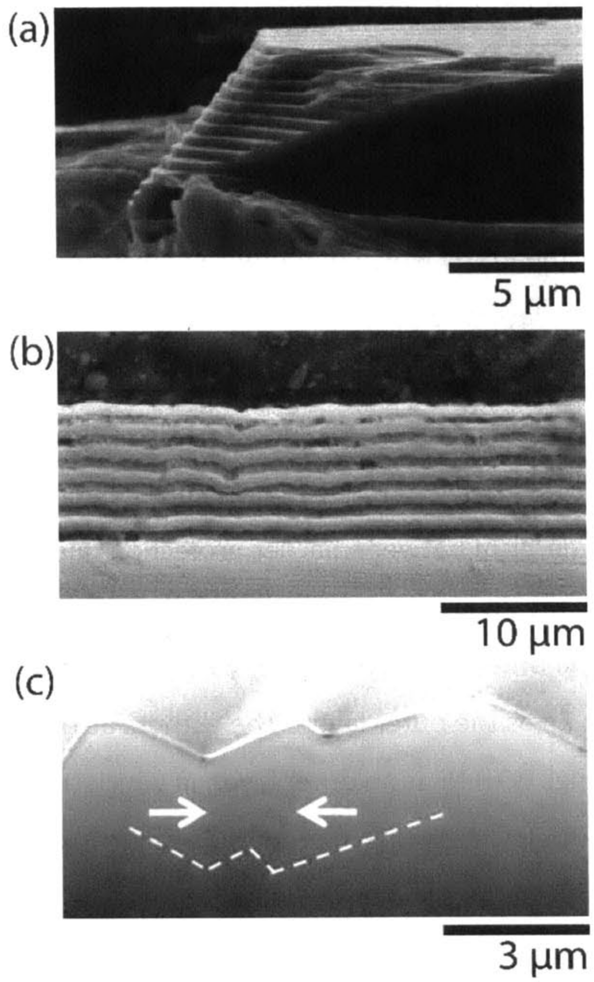

Figure 1.2 Cross sections of various multilayer coatings: (a) PVD Ti/CrN [2], (b) dual-bath electrodeposited Zn/Ni [3], (c) single-bath electrodeposited Al-Mn [4]

1.2.2 Effectiveness of multilayer coatings for corrosion protection

In recent years, a wide range of multilayer coatings have been tested for corrosion protection of susceptible substrates in a variety of conditions, and in many cases it has been shown that multilayer coatings are significantly more protective than monolithic coatings of equal thickness. For example, superior corrosion resistance of electrodeposited coatings with multilayer structures or composition gradients has been reported for Zn/Co[18], Zn/Ni [3], Zn/Zn-Mn [24],and Zn-Fe/Ni [25,26] coatings synthesized via dual bath techniques, and Zn-Ni [20,21,23,27–30], Zn-Fe [17,31], and Zn-Co [18,29] coatings synthesized via single bath techniques. A number of studies have also reported superior corrosion protection for multilayer coatings produced by vapor deposition [2,12–14,32,33], though these studies were focused primarily on thin barrier coatings, rather than the sacrificial coatings studies in this thesis.

One of the principal means by which of multilayer corrosion coatings outperform single layers is by allowing different layers to provide barrier and cathodic protection. For instance, Fei and Wilcox [3] tested multilayer Zn/Ni coatings deposited from dual bath electrodeposition. The time to red rust formation in a neutral salt spray test was increased by a factor of 10 for the best Zn/Ni multilayer coatings relative to monolithic Zn or Ni coatings of equivalent thickness, which they attributed to synergism between barrier protection due to the Ni layers and sacrificial protection due to the Zn layers. However, the effectiveness of the multilayer coatings was highly dependent on the order and number of layers, with significantly better results in particular for coatings with Zn as the outer layer. The authors attributed this difference to localized corrosion in coatings with Ni as an outer layer, in which the outer layer was undercut by corrosion of the Zn layer below resulting in premature failure, as illustrated by the optical micrographs of the corroded coatings shown in Figure 1.3.

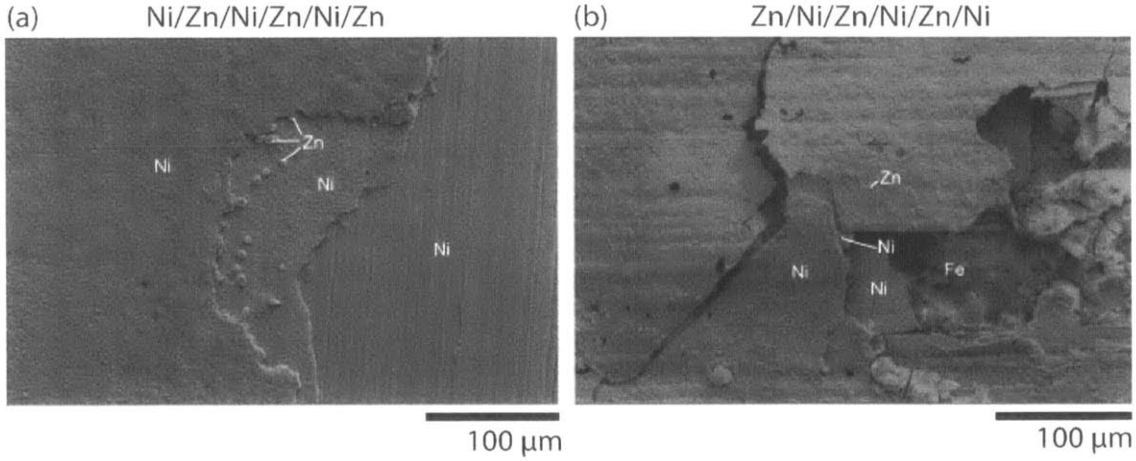

Figure 1.3 Images of multilayer Zn/Ni coatings following salt spray testing [3]. The coating shown in (a) has Zn as the outer layer, while the coating in (b) has Ni as the outer layer.

This type of undercutting is an extremely common phenomenon for multilayer coatings, and should be considered an essential design consideration for development of corrosion coatings. Even a freshly deposited coating cannot be expected to act as a perfect barrier to the underlying material; for instance, the corrosion potential of a multilayer coating is almost invariably found to be close to that of the most active material in the stack, regardless of the order of layers [3,18,25], indicating that the presence of an external barrier cannot fully prevent dissolution of underlying materials if the potential is sufficiently high. Thus the performance of multilayer corrosion coatings is highly dependent on the degree to which corrosion damage can penetrate through barrier layers, as well as the extent to which the coating will be degraded mechanically due to undercutting.

1.3 Numerical models of galvanic corrosion

Galvanic corrosion occurs any time two electrically connected dissimilar metals are exposed to the same corrosive electrolyte. In this case, the more active metal undergoes preferential oxidation, resulting in an increase in the dissolution rate of the more active metal, and a decrease in the dissolution rate of the more noble metal. This segregation of anodic and cathodic reactions is balanced by flows of dissolved ions within the electrolyte through diffusion and electromigration, in order to maintain electroneutrality. As a result, excess anodic and cathodic currents due to the galvanic coupling occur preferentially where the two metals are closest, and decay with a characteristic distance determined by the conductivity of the electrolyte and the polarizability of the two metals [34–37]. As the behavior of dissolved ions under potential and concentration gradients is well described by standard field-based equations, this represents a highly tractable scenario for numerical models, which can calculate the range and magnitude of such galvanic coupling effects, as well as the concentration of dissolved species and potential gradients.

Early work on galvanic corrosion involved calculation of exact analytical solutions to current density distributions over a galvanic couple, using assumptions of extremely simple geometry and polarization kinetics [34,38–40]. While exact analytical solutions only exist for a limited set of conditions, such models were able to produce a number of useful results, such as the concept of the Wagner parameter L_c, which is a characteristic length scale for the range of galvanic coupling based on the polarizability of the two materials, and the conductivity of the electrolyte. However, for more complex geometries and electrode kinetics, computational methods are required to solve numerically for the potential and current density distributions over galvanic couples. Thus a wide variety of computational models of galvanic corrosion have been developed, which determine the state of the electrolyte surrounding a galvanic couple using numerical integration techniques, most commonly the boundary element [41,42], finite difference [43–46] and finite element [5,47–52] methods.

The rise of efficient computational methods for modeling galvanic corrosion has dramatically increased the capability of galvanic corrosion models to capture a wide range of behavior, in particular by incorporating diffusion of dissolved oxygen and ions within the electrolyte. This allows computational models to predict, for instance, the distribution of pH over a galvanic couple, and regions of expected corrosion product precipitation based on the maximum solubility of dissolved metals. For instance, at the cut edge of galvanized steel in neutral aerated NaCl solution, formation of a zinc-based oxide film has been shown to inhibit the cathodic O_2 reduction reaction on the steel surface [36,47,53]. This effect was modeled by Thebault et al. by incorporating a region of complete cathodic inhibition on the steel surface adjacent to the zinc, reporting good agreement between calculations and in-situ current density measurements taken via the scanning vibrating electrode technique [47,53]. Likewise, a pair of computational studies by Brown and Barnard [45,46] looking at corrosion at the cut edge of steel with a 4.5 wt.-% Al zinc-based coating showed that the increased corrosion resistance associated experimentally with finer coating microstructure [54] could be explained by inhibition of O_2 mass transport through precipitated corrosion product layers.

While computational models of galvanic corrosion are well validated on steady-state measurements of freshly prepared samples, there has been very little work on validation of time-dependent models. To our knowledge, the only existing work in this area at the start of this thesis was done by Deshpande [5,49], who modeled two different galvanic couples in NaCl solution, incorporating time dependent changes in surface contours due to predicted metal dissolution. Good agreement between the model and surface profile measurements was reported following a 3 day immersion period, but only for one of the two tested couples, consisting of mild steel / magnesium alloy. For the other couple, consisting of an aluminum alloy and a magnesium alloy, the model significantly underestimated the overall corrosion rate and degree of localization of attack, as is shown in Figure 1.4. Notably, the polarization curve for the aluminum alloy was found to have a large plateau in current density, indicating a high likelihood of passivity and localized corrosion, which was not accounted for by the model. Thus, overall, while it appears that current computational models of galvanic corrosion are able to qualitatively capture the behavior of corroding systems under reasonable conditions, much work is required to apply them to longer times, and in situations in which localized corrosion and changes in surface chemistry over time are likely to play a significant role.

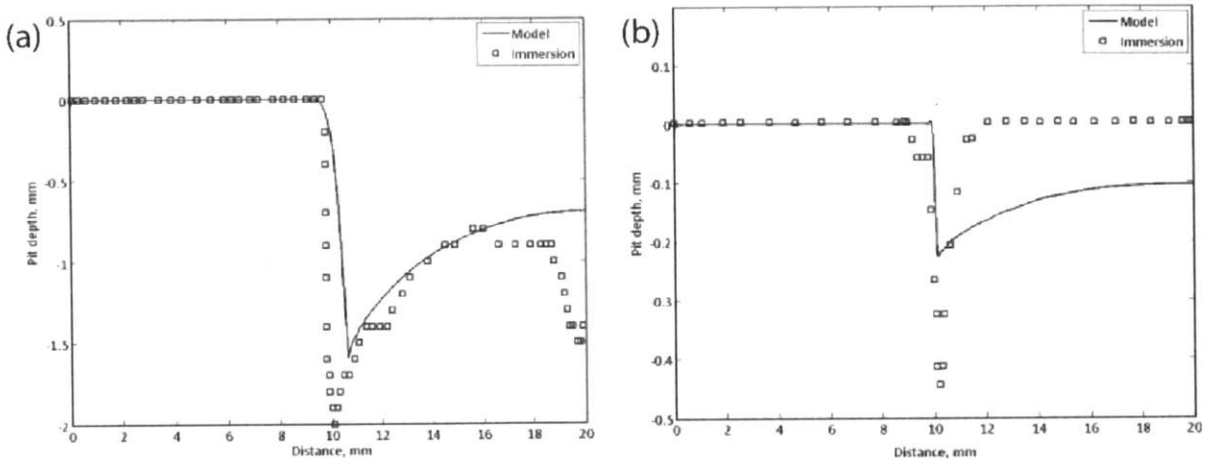

Figure 1.4 Comparison between modeled and experimental surface profiles following 72 hours corrosion in brine solution, for two galvanic couples: (a) steel/magnesium alloy, and (b) aluminum alloy/magnesium alloy [5]

1.4 Localized corrosion

While models of galvanic corrosion such as described in Section 1.3 are designed to predict the distribution of corrosion damage in a galvanic couple, they do not distinguish between different forms of corrosion damage that may occur. In particular, corrosion damage tends to occur with various degrees of localization, resulting in the formation of a damaged layer many times deeper than would be expected if the metal dissolution occurred in a smooth, top-down fashion. The extent to which localization is determined by a number of sources of inhomogeneity in corrosion, which may be broken down into (1) electrode inhomogeneity, and (2) electrochemical heterogeneity [55]. Electrode inhomogeneity refers to variability in the electrode surface, due a number of factors such as inclusions, second phases, regions of stress concentration, while electrochemical heterogeneity refers to effects due to the variation in electrolyte composition and potential.

1.4.1 Pitting corrosion

One of the most common and severe forms of localized corrosion is pitting corrosion, in which both of these two sources of inhomogeneity act in concert to favor localized corrosion, particularly for alloys for which most of the surface is normally passive in the relevant environment. It such a case, once there is a breakdown in the passive surface at some weak point, rapid metal dissolution quickly forms a corrosion pit, and local electrolyte becomes highly concentrated due to the accumulation of dissolved metal ions. The high concentration of metal cations results in a decrease in the local electrolyte pH due to hydrolysis reactions, such as:

$$\mathrm{Fe^{2+} + H_2O \rightarrow FeOH^+ + H^+}$$

as well an increase in the concentration of aggressive anions, most prominently $\mathrm{Cl^-}$, in order to maintain electroneutrality. The decrease in pH and increase in $\mathrm{Cl^-}$ concentration inhibit reformation of the passive oxide film, and so the corrosion pit remains a preferential site for additional metal dissolution. Such corrosion pits can propagate in a stable fashion for a very considerable distance [56–59], resulting in penetration of corrosion damage far deeper into the metal than would be expected based on overall rates of metal loss. The morphology of corrosion pits, such as shown in Figure 1.5, tends to vary widely depending on the materials and conditions under which the pit was formed.

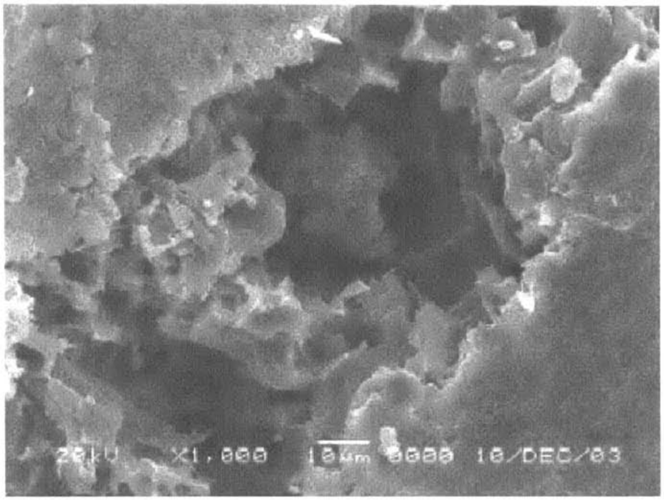

Figure 1.5 SEM micrograph of a corrosion pit in pure aluminum [6].

1.4.2 Models of pitting corrosion

Localized corrosion is a challenging problem for theoretical models, due to its inherently unstable nature, and high dependence on the nature and distribution of relevant defects that act as nucleation points. Theoretical treatment of pitting corrosion generally splits the process into two separate stages: an initiation stage, during which an anodic site is formed due to local breakdown of the passive film, and a propagation stage, during which an initiated corrosion pit experiences stable growth due to its aggressive internal environment [59]. In general, pit initiation events are considered to occur at a finite number of defects that act as weak points for preferential nucleation of pits [60,61].

A number of statistical models have been successful at describing many aspects of the process of pitting corrosion [62–67]. For instance, Valor et. al. used extreme value analysis to generate predictions of the distribution of pit depths over time, based on a Markov-chain model which assigned a population of pits a chance of propagation or extinction with each time step [66]. This model was shown to be effective at reproducing the measured distribution of pits in a number of experimental samples of carbon steel. A similar approach was taken by Murer and Buchheit to stochastically model pitting in aluminum, by simulating a population of pits with time-dependent probabilities of birth, death, and propagation [67]. This model was shown to account well for the observed distribution of pit depths following corrosion in NaCl solution, as well as the frequency of observed pit initiation events measured over an array of aluminum microelectrodes.

Computational attempts to directly model the pitting process have generally relied on a similar approach to the galvanic corrosion models described in Section 1.3, solving field-based equations for diffusion and conductivity in an electrolyte bordering a defect or corrosion pit of predefined geometry [68–72]. For example, Xiao et. al. used a finite element model to solve for the distribution of dissolved species within the electrolyte of simulated pits, starting from initial defect states shown in Figure 1.6 [72]. The model developed by Xiao et. al. solved for steady state diffusion conditions for all dissolved ions in the electrolyte, including the numerous metal-chloride and metal-hydroxide complexes formed through association reactions, producing a highly detailed description of the internal state of the pit. However, it is often challenging to convert detailed simulation of individual pits such as this to predictions of the behavior of bulk materials, particularly as the predictions regarding the internal pit environment are generally not possible to directly compare to experimental measurements. However, these models can be used to accurately calculate how expected properties of corrosion pits will vary with changing conditions; for instance, Laycock et. al. used a computational model to calculate criteria for stable pit propagation in stainless steel, and showed that the model could explain variations in pitting potential for stainless steels with different surface roughness, and density of inclusions [70,71].

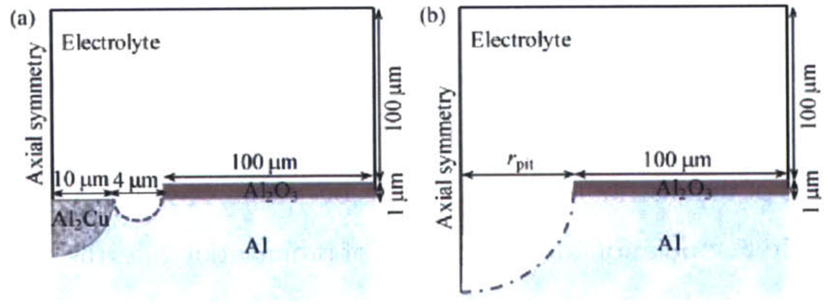

Figure 1.6 Geometry used for finite element model of pitting corrosion of aluminum [72].

However, although both statistical and computational models of pitting corrosion have been successful in a number of areas, they suffer from several significant limitations. In particular, both approaches rely on a description of the material as a solid, uniform bulk material, with the presence of a discrete number of well-defined corrosion pits. While this may be a good approximation in several instances, it does not apply well for weakly passive materials such as are used in corrosion coatings that supply cathodic protection. For example, Baumgartner and Kaesche found that the morphology of aluminum pits formed under relatively mild conditions takes the form of a complex network of tunnels that follow crystallographically preferred directions, resulting in a porous structure with a fractal surface [73]. However, even in pits with roughly hemispherical dimensions, such as shown in Figure 1.5, it is clear that crystallography has a significant effect in determining the evolving shape of the pit.

1.5 Structure of thesis

1.5.1 Problem statement

While multilayer corrosion coatings, such as were described in Section 1.2, have great potential for vast improvements in corrosion protection, they also present an extremely large possible design space. The effectiveness of multilayer coatings is highly dependent not only on the properties of the layers used, but also on the number, order, and thickness of each layers, resulting in many degrees of freedom in design of candidate coatings. Thus, this thesis seeks to apply the techniques of numerical corrosion modeling to the problem of multilayer corrosion coating design. In order to move towards this goal, this thesis seeks to develop a computational modeling approach that can generate useful predictions of coating lifetime, and test the predictions of the developed model in standardized corrosion tests. The chapters of this thesis address the various challenges involved with development and validation of a time dependent corrosion model with meaningful predictive ability.

1.5.2 List of thesis chapters

- Chapter 2: This chapter provides a detailed description of the experimental techniques used in this thesis for electrodeposition of aluminum alloy multilayers, which are used as the principal coating materials for testing of the computational model. The microstructure and corrosion properties of the electrodeposited coatings are discussed, as well as strategies to improve electrodeposit quality through variation of deposition conditions and alloying.

- Chapter 3: This chapter describes the development of a basic computational model for galvanic corrosion of compositionally graded sacrificial coatings. The model is applied to a hypothetical test system consisting of a graded zinc alloy coating on steel, to assess the effects of composite coating structures.
- Chapter 4: This chapter describes the validation of the galvanic corrosion model described in Chapter 3 based on quantitative comparison between model predictions and time-dependent experimental measurements of zinc and aluminum undergoing galvanic corrosion on steel.
- Chapter 5: This chapter describes the development of a 1-D computational model of localized corrosion of multilayer films, and its application to single and multilayer aluminum alloy coatings in 50 mM NaCl solution. The model is validated through comparison with experimental measurements of a range of phenomena that are difficult to capture using traditional corrosion modeling techniques. The generation of optimized coating structures and the overall predictive ability of the model are discussed.

2. Electrodeposition of aluminum and zinc alloy thin films

In this chapter, we present an overview of the various techniques used in this thesis for synthesis of single and multilayer aluminum alloy and zinc alloy thin films. Aluminum and zinc alloys have a number of highly attractive properties for use in corrosion coatings for steel substrates, in particular the balance between sacrificial protection provided by the zinc and high corrosion resistance provided by the aluminum. In addition, zinc and aluminum are very low cost and have widely studied corrosion behavior. However, synthesis of multilayer aluminum-zinc alloy electrodeposits of sufficiently high quality to use for corrosion coatings presented a number of technical challenges, which are discussed in greater detail below.

2.1 Experimental procedures for aluminum alloy electrodeposition

Electrodeposition of all aluminum alloys was performed from an anhydrous 2:1 molar mixture of $AlCl_3$ and EMIC (>98%, Iolitec) in a glovebox under an inert nitrogen atmosphere. The ionic liquid was purified for three days through gentle stirring with a strip of pure aluminum (99.99%, Sigma-Aldrich), resulting in a clear light yellow liquid. Anhydrous $ZnCl_2$ was added to a concentration of 0.1 mol l^{-1}. Anhydrous $ZrCl_4$ and $MnCl_2$ were also added to a concentration of 0.02 mol l^{-1} for the Al-Zn-Zr and Al-Zn-Mn baths, respectively. In addition, a separate aqueous bath was prepared for electrodeposition of pure zinc as a comparison material. The composition of the aqueous zinc bath was 1 mol l^{-1} sodium citrate, 0.2 mol l^{-1} zinc sulfate, and 0.001 mol l^{-1} L-cysteine.

The substrates for electrodeposition were 1018 steel (McMaster-Carr) for the immersion corrosion tests, and high purity copper (99.9%, McMaster-Carr) for all other samples. Prior to electrodeposition, each substrate was ground with SiC papers, then polished sequentially with 3, 1, and 0.25 μm diamond polishing compound to obtain a mirror finish, following by ultrasonic degreasing in acetone for 60 seconds. The samples were painted using an enamel spray paint to expose an active area of 1.2 x 2 cm. The samples were then pickled for 30s using 10% H_2SO_4 for the copper and 18% HCl for the steel, dried thoroughly, and placed in a nitrogen-filled glovebox (with oxygen concentration below 2 ppm) for electrodeposition. The steel substrates were activated by 30 seconds of anodic conditioning at 40 Am^{-2} in the electrodeposition bath, just prior to the start of electrodeposition. All electrodeposition was performed galvanostatically in unstirred electrolyte at ambient temperature (23±2 °C), using a 99.9% Zn strip (Sigma-Aldrich) as an anode. Samples used for characterization of surface morphology and roughness were deposited to a total passed charge of 30 Ccm^{-2}, for a nominal thickness of 8-12 μm, while samples for potentiostatic polarization measurements were deposited to a total passed charge of 10 Ccm^{-2}. Following electrodeposition, the samples were immediately removed from the glovebox, rinsed quickly in deionized water, and dried thoroughly with compressed air.

The above procedures were used to create single-layer coatings, as well as multilayer coatings effected by alternating the applied current. A wide variety of coatings were produced, and in the rest of this chapter we will label these with a shorthand notation as follows:

- Zn, Al: nominally pure coatings of Zn or Al, respectively
- AZxx: Al-Zn alloy coating produced with applied current density of xx Am^{-2}
- AZMxx: Al-Zn-Mn alloy coating produced with applied current density of xx Am^{-2}
- AZZxx: Al-Zn-Zr alloy coating produced with applied current density of xx Am^{-2}
- Mxa: Al-Zn-Zr multilayer coating with x layers, produced by alternating the applied current density between 40 and 80 Am^{-2}, with the base layer deposited at 40 Am^{-2}
- Mxb: Al-Zn-Zr multilayer coating with x layers, produced by alternating the applied current density between 40 and 80 Am^{-2}, with the base layer deposited at 80 Am^{-2}

Characterization of surface morphology and composition was performed using scanning electron microscopy with energy-dispersive spectroscopy (SEM/EDS; JEOL JSM-6610LV). Cross-sections for SEM observation were prepared through focused ion beam milling (FIB; Helios Nanolab 600). X-ray diffractometry (XRD; X'Pert PANalytical) of electrodeposits was performed using Cu K_α radiation at 45 kV and 40 mA. Measurements of surface roughness and film thickness were performed using surface contact profilometry (KLA Tencor P-16), with a 2 μm tip diameter and a scan rate of 50 $\mu m\ s^{-1}$. Reported surface roughness values were calculated from the root-mean-square deviation of 51 parallel surface height profiles with 2 μm spacing, covering a 100 x 500 μm region taken from the center of each coating.

Potentiostatic polarization measurements were taken in aerated 50 mM NaCl electrolyte solution, using a standard 3 electrode setup in a Gamry multiport corrosion cell, connected to an AutoLab potentiostat controlled using GPES software. A graphite rod (Gamry) was used as a counter electrode, and potentials were measured using a silver/silver chloride electrode (SSCE; Gamry). Prior to polarization measurements, freshly deposited coatings were immersed in electrolyte solution for 15 minutes while air was gently bubbled through the solution. Anodic polarization curves were then taken at a scan rate of 100 mV min^{-1}, starting from at least 200 mV below the open circuit potential, to a maximum potential at least 200 mV above the open circuit potential.

Immersion corrosion tests were performed in naturally aerated 50 mM NaCl electrolyte solution, until the formation of red rust on 5% of the visible surface. Each sample was immersed in a separate container with 200 mL electrolyte, which was refreshed every 48 hours for the duration of the tests. Each sample was gently dipped in DI water for approximately 10 seconds during each electrolyte change to remove excess corrosion products. The corrosion potential of each sample was measured manually every 24 hours using a high-impedance voltmeter (Fluke) and a SSCE reference electrode.

2.2 *Electrodeposition of Al-Zn binary alloys*

Electrodeposition of Al-Zn was performed at constant current densities ranging from 24 to 100 Am^{-2} for a total passed charge density of 30 Ccm^{-2}. All of the tested electrodeposits were compact and showed good adhesion to the substrate. The electrodeposits from 60 to 100 Am^{-2} had a bright silver surface appearance, while the lower current density deposits had duller surfaces ranging from light gray at 48 Am^{-2} to dark gray at 24 Am^{-2}. Particularly at lower current densities, the Al-Zn electrodeposits exhibit a dual-phase microstructure, with zinc dendrites embedded in an aluminum-rich matrix, quite similar to the microstructures reported by Pan et al. [74,75]. As shown in Fig. 2.1 (a-c), the size and density of the zinc dendrites increases with decreasing current density, ranging from occasional submicron particles in the AZ80 coating to 10 μm zinc dendrites covering much of the surface in the AZ24 coating. A close-up of the characteristic matrix-dendrite microstructure, shown in Fig. 2.1 (d) for AZ32, illustrates the distinct topographical contrast between the zinc particles and aluminum-rich matrix.

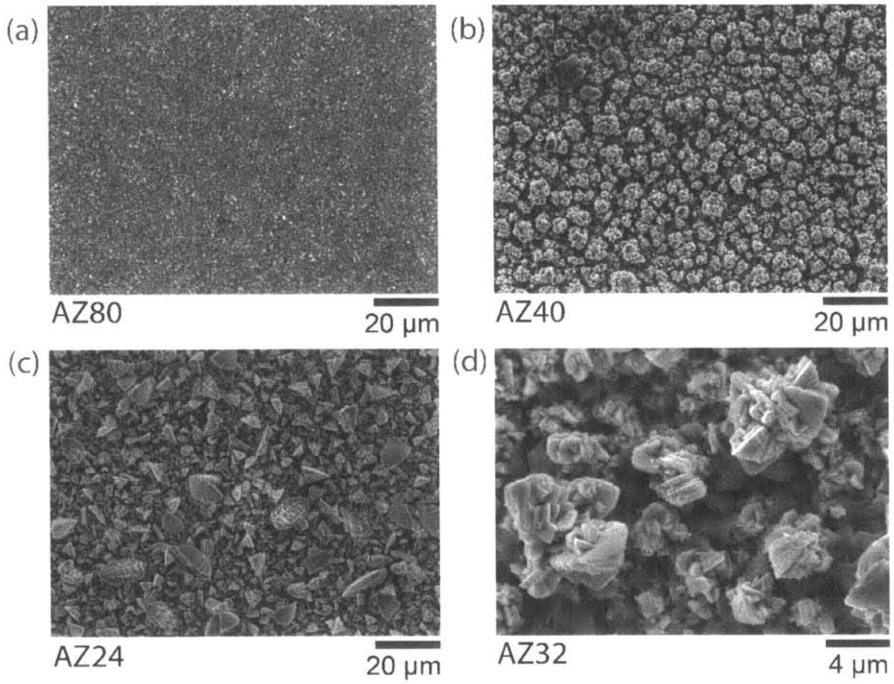

Figure 2.1 SEM micrographs of Al-Zn binary electrodeposits for different deposition rates: (a) AZ80, (b) AZ40, and (c) AZ24. A close-up of a typical dendrite/matrix microstructure is shown in (d), for AZ32.

Quantitative surface EDS measurements were taken from several points in the matrix phase and dendrites for each current density. For all of the tested deposits, measured point compositions for the dendrites range from 90-100 at.% Zn, while compositions for the matrix are spread widely, but fall in the range of 10-40 at.% Zn. In addition, a quantitative EDS linescan was taken over a 100 µm interval, to obtain an average composition for each coating. The black circles and error bars in Figure 2.2 (a) show the average and standard deviation of the zinc content measured in each EDS linescan. The overall composition is determined primarily by the ratio of the two phases, varying from approximately 25 at.% Zn for the AZ100 electrodeposit to 74 at.% Zn for the AZ24 electrodeposit.

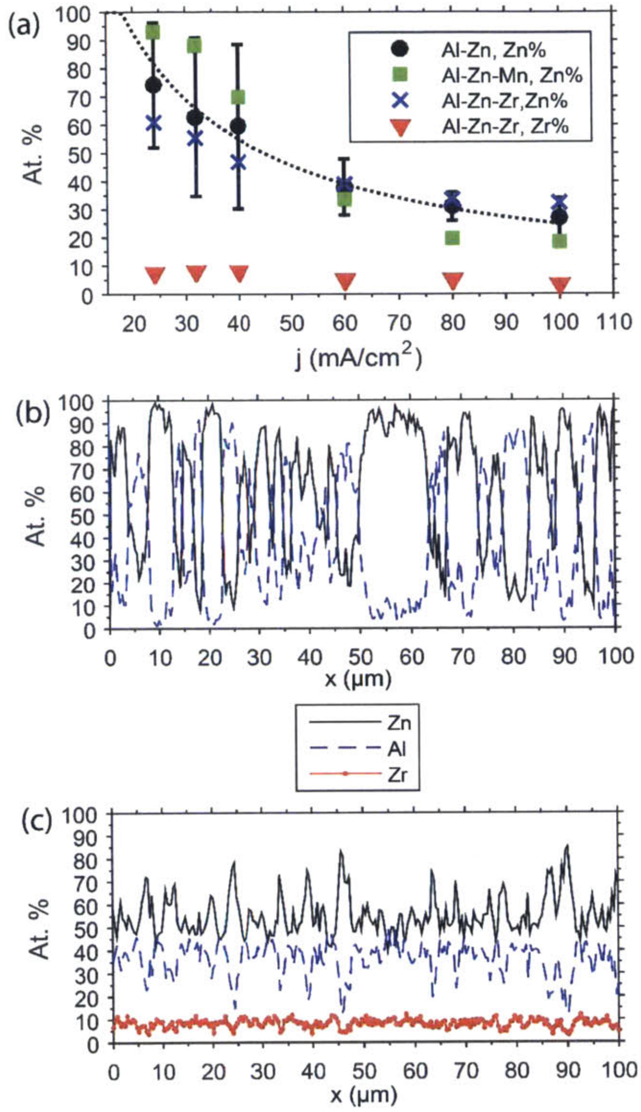

Figure 2.2 (a) Surface EDS composition versus deposition current density, for Al-Zn, Al-Zn-Mn, and Al-Zn-Zr electrodeposits. The dotted line indicates the composition calculated according to Eq. (2.3), for a constant Zn deposition current of 16 Am^{-2}. (b) EDS surface composition line scan for AZ32. (c) EDS surface composition line scan for AZZ32.

By the Faraday equation, the rate of zinc plating r_{Zn} is related to the zinc deposition current density j_{Zn} by:

$$r_{\mathrm{Zn}} = \frac{j_{\mathrm{Zn}}}{z_{Zn}F} \tag{2.1}$$

where $z_{\mathrm{Zn}} = 2$ is the number of electrons transferred with each deposited atom of zinc, and F is the Faraday constant. Likewise the rate of aluminum plating r_{Al} is given by:

$$r_{\mathrm{Al}} = \frac{j_{\mathrm{Al}}}{z_{\mathrm{Al}} F} \tag{2.2}$$

where $z_{\mathrm{Al}} = 3$ is the number of electrons transferred with each deposited atom of aluminum. Thus the atomic concentration of zinc in the deposit will be given by:

$$c_{\mathrm{Zn}} = \frac{z_{\mathrm{Zn}} z_{\mathrm{Al}} j_{\mathrm{Zn}}}{z_{\mathrm{Zn}} j_{\mathrm{Al}} + z_{\mathrm{Al}} j_{\mathrm{Zn}}} \tag{2.3}$$

The dashed line in Figure 2.2 (a) shows the Zn composition predicted by Eq. 3 for a constant zinc deposition current of 16 Am^{-2}, with Al deposition responsible for the balance. The close agreement with the measured composition of the Al-Zn electrodeposits shows that the rate of zinc deposition is close to this value for all electrodeposition conditions, suggesting that the zinc deposition process is primarily diffusion limited in this system, while Al deposition is primarily activation controlled. However, the low current density electrodeposits show a very large variability in the measured composition over the 100 μm linescans, as illustrated in Figure 2.2 (b), which shows a bimodal distribution in composition between points with >90 at.% Zn corresponding to zinc dendrites, and points with 10-40 at.% Zn corresponding to measurements taken at points in the matrix.

2.3 Electrodeposition of ternary alloys

Electrodeposition of Al-Zn-Mn and Al-Zn-Zr was performed in identical conditions to the electrodeposition of Al-Zn, with the addition of either 0.02 mol l^{-1} $MnCl_4$ or $ZrCl_4$ to the bath. Visually, the Al-Zn-Mn electrodeposits appeared quite similar to Al-Zn, ranging from a bright silver surface at 100 Am^{-2} to a rough, dark gray surface at 24 Am^{-2}. Typical surface morphology for the Al-Zn-Mn electrodeposits is illustrated by SEM micrographs of AZM80, AZM40, and AZM24 in Figure 2.3 (a) - (c). As in the case of Al-Zn, the Al-Zn-Mn electrodeposits exhibit a dual phase microstructure consisting of zinc dendrites embedded in an aluminum-rich matrix, shown in close-up in Figure 2.3 (d). However, the microstructure of the Al-Zn-Mn electrodeposits is significantly coarser at lower current densities, and the surface zinc coverage is much greater. The overall Zn composition vs. deposition current density curve for the Al-Zn-Mn electrodeposits, shown as the green squares in Figure 2.2 (a) and summarized in Table 1, show a similar trend to that of the Al-Zn deposits, though with a greater range of variation. The Mn content of all films was in the range of 0.5-2 at.%. For the lowest current density deposits, the zinc-rich surface layer was porous and brittle, and could be largely removed through gentle abrasion to reveal an aluminum-rich matrix phase beneath. Thus, the very high Zn content measured through EDS for the lower current density Al-Zn-Mn deposits is more likely a reflection of surface plating of Zn, rather than the true average composition of the deposit. The higher current density deposits, on the other hand, show depletion of Zn relative to the Al-Zn binary deposits. This suggests that ternary alloying with Mn decreases the ability of Zn to incorporate into the aluminum matrix, and instead encourages and exacerbates phase separation within the electrodeposit.

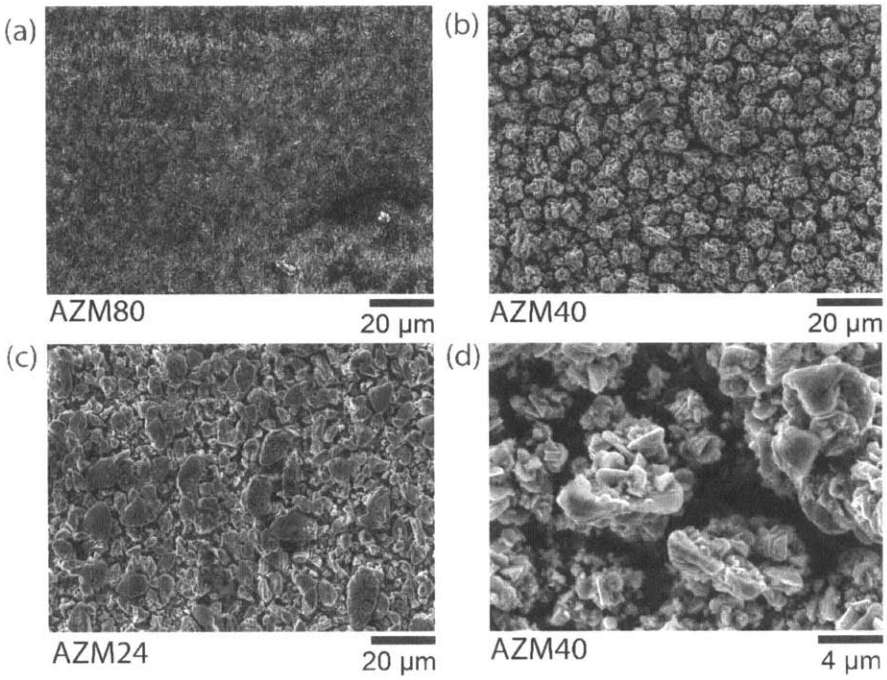

Figure 2.3 SEM micrographs of Al-Zn-Mn ternary electrodeposits for different deposition rates: (a) AZM80, (b) AZM40, and (c) AZM24. A close-up of a typical dendrite/matrix microstructure is shown in (d), for AZM40.

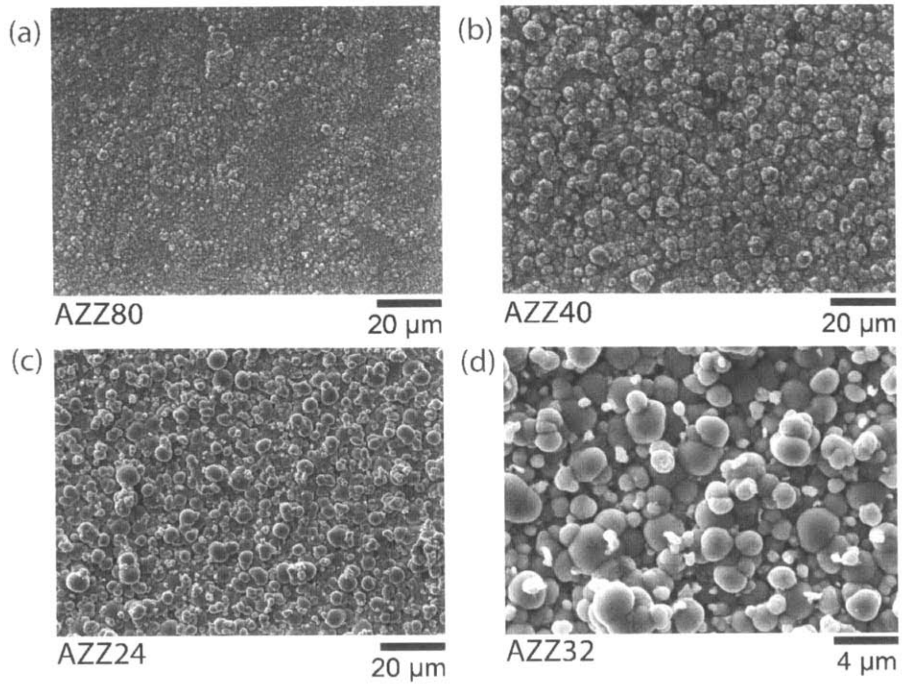

Figure 2.4 SEM micrographs of Al-Zn-Zr ternary electrodeposits for different deposition rates: (a) AZZ80, (b) AZZ40, and (c) AZZ24. The micrograph (d) for AZZ32 shows the nodular surface characteristic of nanocrystalline or amorphous electrodeposits.

In contrast to Al-Zn and Al-Zn-Mn, the Al-Zn-Zr electrodeposits appeared a dull light gray at all current densities, getting only slightly darker at the lowest current density of 24 Am^{-2}. The average surface composition, shown in Figure 2.2 (a), is similar to that of the Al-Zn electrodeposits at the same current density, with the addition of 5-10 at.% Zr. SEM surface micrographs of the AZZ80, AZZ40, and AZZ24 deposits are shown in Figure 2.4 (a) - (c). The AZZ80 electrodeposit showed a similar character to that of AZ80, with the exception of the appearance of nodules approximately 1-2 μm in diameter. These nodules were not associated with any obvious variation in composition or second phase formation. At lower current densities, the Al-Zn-Zr electrodeposits show rounded crystallites with diameters of up to 4 μm, in clear contrast to the faceted dual-phase microstructures observed in Al-Zn. Such microstructures are generally considered to be highly suggestive of nanocrystalline or amorphous electrodeposits [4,76]. This conclusion is supported by the XRD spectra for Al-Zn, Al-Zn-Zr, and Al-Zn-Mn electrodeposits, shown in Figure 2.5 for a range of current densities. All spectra show clear peaks for Al fcc and Zn hcp phases, as well as the Cu fcc substrate, with the relative intensity of the Al peaks increasing and Zn peaks decreasing with increasing deposition current density. However, the Al-Zn-Zr electrodeposits at low current density also exhibit a low, broad hump in the range 35-45 degrees, as well as decreased intensity for the Al and Zn crystal peaks, suggesting that a significant fraction of the deposit has a nanocrystalline or perhaps even amorphous microstructure.

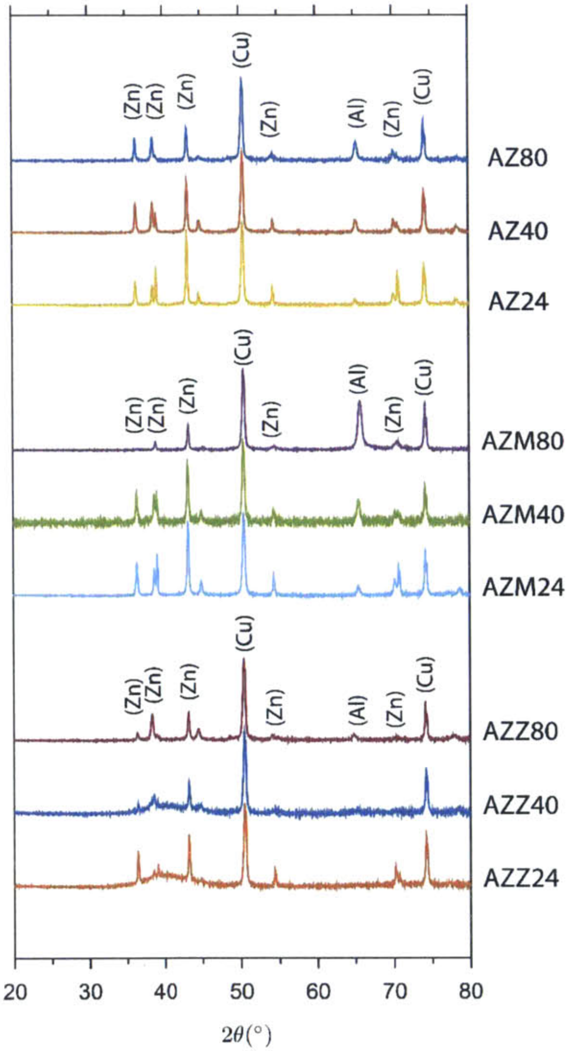

Figure 2.5 XRD scans of binary and ternary Al-Zn electrodeposits. The arrows denote the appearance of a broad hump around the nearest-neighbor reflection in the AZZ40 and AZZ24 alloys, suggesting a fine nanostructure or an amorphous phase.

2.4 Surface roughness

To evaluate electrodeposit surface roughness, 3-D height profiles were taken on 100 x 500 μm regions in the center of each coating, using 50 line scans spaced 2 μm apart. Figure 2.6 (a) shows a representative 3-D height profile for the binary AZ48 deposit, while the associated marked line scan is shown in Figure 2.6 (b). In both the 3-D and line scans, the dendrites are clearly visible as sharp peaks of up to 6 μm height, while the regions of matrix in between are quite flat and show variations in height of less than 1 μm. Evidently, at least in the case of Al-Zn, the density and size of zinc dendrites is the dominant factor determining the surface roughness.

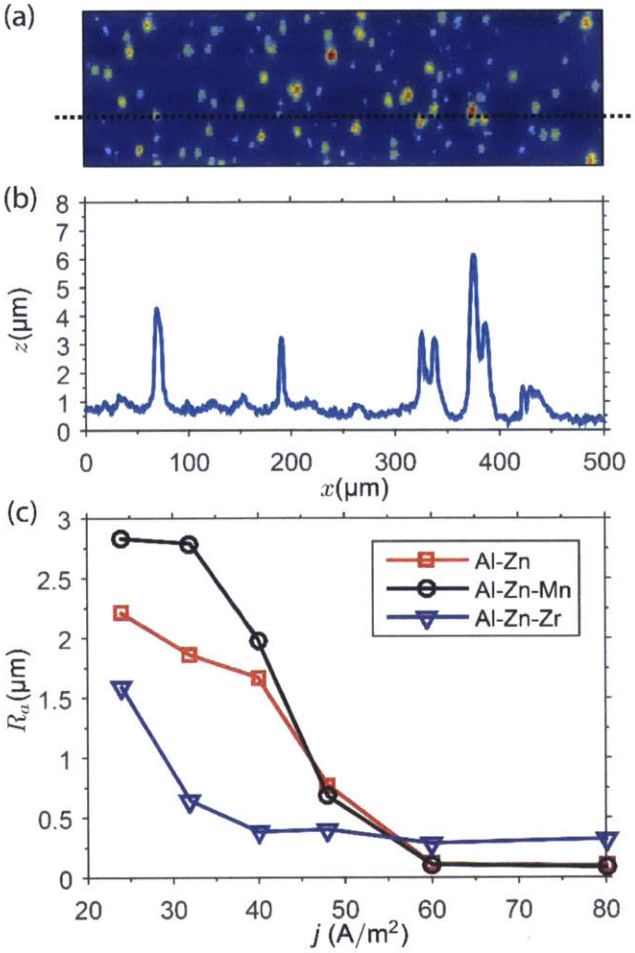

Figure 2.6 (a) Surface topology map for a representative Al-Zn electrodeposit AZ48. (b) Surface height profile associated with the line marked in (a). (c) Surface roughness measurements at different deposition current densities.

The calculated surface roughness as a function of current density for Al-Zn, Al-Zn-Mn, and Al-Zn-Zr is shown in Figure 2.6 (c). The surface roughness results closely mirror the surface morphology observed via SEM. For Al-Zn, the surface roughness increases significantly as the deposition current density drops from 60 to 40 Am^{-2}, which is the same range over which large zinc dendrites become visible in the deposits. The Al-Zn-Mn deposits show a similar, though larger, trend toward increased roughness with decreasing current density, consistent with the increased dendrite formation observed in the low current density Al-Zn-Mn coatings.

The Al-Zn-Zr deposits, however, show virtually no increase in surface roughness down to a deposition current density of 40 Am^{-2}, after which the roughness increases but remains significantly lower than that of Al-Zn. The Al-Zn-Zr deposits do, however, have slightly higher roughness at 60 and 80 Am^{-2}, which is likely due to the nodular surface observed in the micrographs. The full set of measured composition and structural parameters for the binary and ternary electrodeposits is summarized in Table 2.1.

Table 2.1 Measured structural parameters and compositions for selected Al-Zn binary and ternary electrodeposits.

Electrodeposit	R_a	Al	Zn	Mn	Zr
AZ24	2.21 μm	25.9±22.1 at.%	74.1±22.1 at.%	0	0
AZ40	1.67 μm	40.6±29.1 at.%	59.4±29.1 at.%	0	0
AZ60	0.113 μm	61.8±9.5 at.%	38.2±9.5 at.%	0	0
AZ80	0.097 μm	65.9±4.4 at.%	34.1±4.4 at.%	0	0
AZM24	2.83 μm	6.0±7.7 at.%	93.2±8.4 at.%	0.7±1.2 at.%	0
AZM40	1.98 μm	28.3±25.7 at.%	70.1±26.9 at.%	1.5±1.9 at.%	0
AZM60	0.108 μm	65.2±2.4 at.%	33.7±2.3 at.%	1.1±0.1 at.%	0
AZM80	0.103 μm	79.0±1.1 at.%	19.4±1.0 at.%	1.6±0.1 at.%	0
AZZ24	1.59 μm	31.1±12.6 at.%	61.1±14.6 at.%	0	7.8±2.8 at.%
AZZ40	0.382 μm	46.0±5.3 at.%	45.6±4.9 at.%	0	8.4±2.0 at.%
AZZ60	0.287 μm	54.5±3.5 at.%	39.1±3.8 at.%	0	6.4±1.0 at.%
AZZ80	0.322 μm	61.4±4.8 at.%	33.5±4.9 at.%	0	5.0±1.5 at.%

2.4 Cyclic voltammetry

Because ternary alloying with Zr, but not Mn, was found to significantly improve electrodeposit homogeneity and surface morphology and increase the range of useful deposition rates, we chose to focus on Al-Zn with and without Zr additions as the most viable candidates for use in multilayered corrosion coatings. The corrosion resistance of the Al-Zn and Al-Zn-Zr electrodeposits was first examined using cyclic voltammetry in aerated 50 mM NaCl solution, as well as pure Al foils (99.99%, Alfa Aesar), a pure Zn electrodeposit from the aqueous Zn solution, and a bare 1018 steel substrate (McMaster). The cyclic voltammogram of the AZ80 electrodeposit, shown in Figure 2.7 (a), illustrates the typical corrosion behavior observed in these tests. Partial passivity is observed on the first anodic scan, with a rapid increase in current density above a pitting potential E_{pit}. Above the pitting potential, visible gas bubbles emerged from pores in the surface, presumably due to hydrogen evolution from acidified pit interiors. Subsequent scans following the initiation of pitting show reproducible behavior, with moderate anodic current observed for several hundred mV below E_{pit}, increasing rapidly for potentials above E_{pit}. This pattern suggests that the anodic currents below E_{pit} on the second and third scans are due to active dissolution within the interior of pits that were formed during the first scan, while the rapid increase in current density observed above E_{pit} is due to the formation of additional stable pits. The kinetics of the active dissolution show an excellent fit to an exponential relation between potential and current density:

$$j_{\mathrm{a}} = j_{0,a} \exp\left(\frac{E - E^0}{\beta_{\mathrm{a}}}\right)$$

$$j_{\mathrm{c}} = j_{0,\mathrm{c}} \exp\left(\frac{E - E^0}{\beta_{\mathrm{c}}}\right)$$

$$j_{\mathrm{net}} = j_{\mathrm{a}} - j_{\mathrm{c}}$$

where j_a, j_c, and j_{net} are the anodic, cathodic, and net current density, $j_{0,\mathrm{a}}$ and $j_{0,\mathrm{c}}$ are the anodic and cathodic current densities at the reference potential E^0, and β_{a} and β_{c} are the anodic and cathodic Tafel slopes. It should be noted, however, that measured cathodic currents may be due to a number of different reduction reactions, including oxygen reduction, hydrogen evolution, reduction of surface oxides, and redeposition of zinc ions. Therefore, the cathodic kinetic parameters j_c and β_c are used only for fitting and for estimation of the corrosion current, and should not be construed to represent the kinetics of a specific reaction. For the sake of comparison, the value of the reference potential is fixed at $E^0 = -0.76$ V vs SHE for all deposits, equal to the standard reduction potential for zinc. The Tafel fit for the representative deposit is shown inset in Figure 2.7 (a), with associated kinetic parameters included in Table 2.

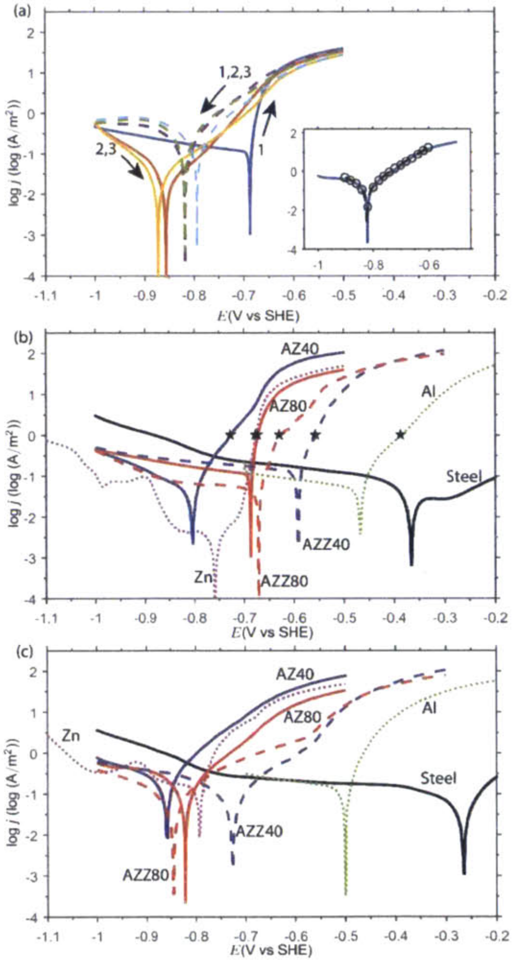

Figure 2.7 (a) Cyclic voltammogram for AZ80 electrodeposit, showing three cycles in aerated 50 mM NaCl solution. Inset – Tafel fit for averaged second scan. (b) First anodic scans, with pitting potentials marked with a star. (c) Averaged second scans.

As this general pattern is shared among all the tested electrodeposits, the corrosion behavior of the different materials is compared quantitatively based on the pitting potentials, determined from the initial anodic polarization curves shown in Figure 2.7 (b), and the exponential dissolution kinetics fit to the averaged second scans shown in Figure 2.7 (c). Although not all of the polarization curves in Figure 2.7 (b) exhibit a clear active-passive transition, in all cases the second and subsequent scans exhibit substantially higher anodic dissolution currents starting at a lower applied potential, suggesting a significant disruption of passivity during the first scan. Therefore, for the sake of comparison, pitting potentials for each sample are assessed by the applied potential at which the net anodic current density first surpassed 1 Am^{-2}, marked by the stars in Figure 2.7 (b). The values of E_{pit} and kinetic Tafel parameters for each deposit are included in Table 2.2.

Table 2.2 Measured pitting potential and electrochemical kinetics for selected Al-Zn and Al-Zn-Zr electrodeposits and reference materials.

Electrodeposit	E^0_{ref}	$j_{0,\mathrm{a}}$	β_{a}	E_{corr}	E_{pit}
AZ40	-0.76 V vs SHE	2.6 Am^{-2}	0.130 V	-0.86 V vs SHE	-0.73 V vs SHE
AZ80	-0.76 V vs SHE	0.58 Am^{-2}	0.108 V	-0.82 V vs SHE	-0.67 V vs SHE
AZZ40	-0.76 V vs SHE	0.16 Am^{-2}	0.204 V	-0.71 V vs SHE	-0.56 V vs SHE
AZZ80	-0.76 V vs SHE	0.48 Am^{-2}	0.223 V	-0.85 V vs SHE	-0.63 V vs SHE
Zn	-0.76 V vs SHE	2.3 Am^{-2}	0.045 V	-0.80 V vs SHE	-0.66 V vs SHE
Al	-1.6 V vs SHE	N/A	N/A	-0.49 V vs SHE	-0.39 V vs SHE
Steel	-0.45 V vs SHE	0.025 Am^{-2}	0.200 V	-0.27 V vs SHE	N/A

The Al foil was significantly more noble than any of the tested Al-Zn alloys, with a sharp and reproducible pitting transition at $E = -0.38$ V vs SHE. The Zn electrodeposit, on the other hand, showed weakly passive behavior initially, followed by rapid active dissolution on subsequent scans. In the case of the binary Al-Zn deposits, the dissolution kinetics and measured pitting potential are remarkably similar to that of pure zinc. This is likely due to the presence of zinc particles within the deposit, which are known to act as pitting nucleation sites in Al-Zn alloys [77]. The alloying of 15-30 at.% zinc into the aluminum matrix may also act to destabilize the passive film, resulting in increased susceptibility to pitting. In fact, both of the binary Al-Zn electrodeposits were observed to have dissolved completely after several scans, suggesting that the anodic behavior in the polarization curve is due to the dissolution of the matrix as well as the zinc phase. In addition, the AZ40 electrodeposit shows slightly greater activity than AZ80, with a lower corrosion potential, lower pitting potential, and faster dissolution kinetics. This is likely due to the higher Zn content in AZ40, which is generally observed to result in decreased corrosion resistance in Al-Zn alloys [78].

In comparison to the binary Al-Zn deposits, the Al-Zn-Zr deposits show an increase in the pitting potential and a significant decrease in the kinetics of the dissolution reaction. Also in contrast to the binary alloy, the AZZ40 electrodeposit shows improved corrosion resistance relative to AZZ80, despite the higher zinc content. The further improvement in corrosion resistance may be due to the transition from a coarse grained to a nanocrystalline or amorphous microstructure, which has been widely reported to increase resistance to localized corrosion [79]. The difference in corrosion susceptibility between the AZZ40 and AZZ80 deposits suggests that they are promising candidates for use in multilayer electrodeposits for corrosion protection, since the AZZ40 layers would be cathodically protected by the AZZ80, and should therefore act as effective barriers for limiting penetration of corrosion damage, by, for instance, slowing pit propagation, or reducing infiltration of dissolved oxygen to cathodically active sites on the substrate.

2.6 Multilayer Electrodeposits

Figure 2.8 shows cross sections of multilayer Al-Zn and Al-Zn-Zr electrodeposits with deposition current density alternating between 80 and 40 Am^{-2}, with 5 Ccm^{-2} of passed charge for each layer and 30 Ccm^{-2} for the full deposit, resulting in a total of three layers at each deposition current density. In both cases, the electrodeposits appear compact and well adhered to the substrate. For the Al-Zn deposit in Figure 2.8 (a), Zn particles are visible in thin horizontal rows embedded within the Al matrix. Although the density of the Zn particles is higher in the AZ40 layers, it is quite difficult to distinguish distinct layers within the cross section. In comparison, the layered structure of the Al-Zn-Zr deposit in Figure 2.8 (b) is much more apparent. Although the layers become rougher as the deposit becomes thicker, they maintain distinctly different microstructures, with the rounded nodular character visible in the AZZ40 layers. This suggests that the Al-Zn-Zr electrodeposit may be able to attain superior corrosion protection due to the presence of continuous and distinct barrier layers, while merely varying the phase fractions in the Al-Zn deposit is less likely to produce a continuous barrier following the dissolution of the more susceptible phase.

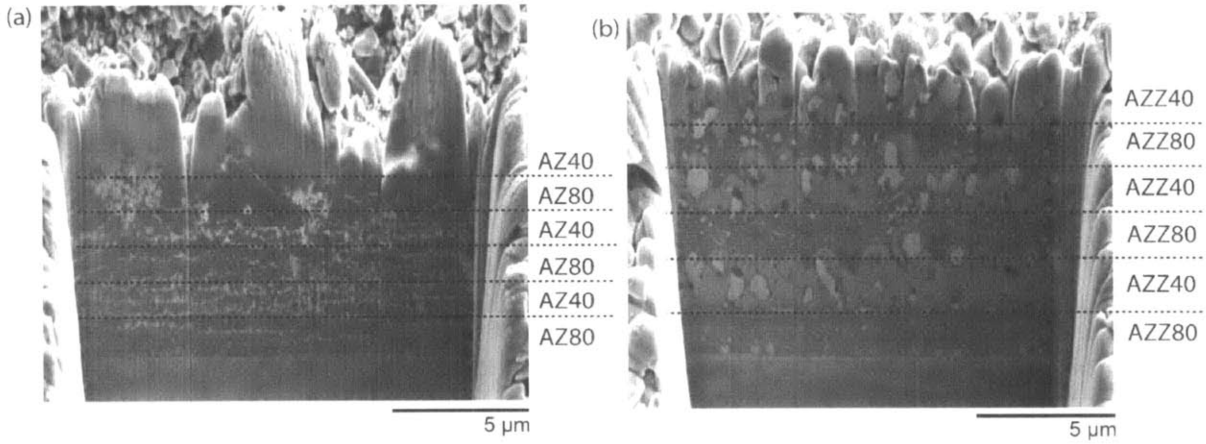

Figure 2.8 FIB cross sections showing (a) Al-Zn and (b) Al-Zn-Zr multilayer electrodeposits produced through modulation of deposition current density between 40 and 80 Am^{-2}. Dashed lines indicate approximate location of interfaces between layers.

2.7 Immersion testing

To evaluate the ability of Al-Zn-Zr single and multilayer coatings to protect a steel substrate, immersion corrosion tests were performed on single layer AZZ40 and AZZ80 electrodeposits, as well as the multilayer deposits with two and four layers formed by alternating between the AZZ40 and AZZ80 materials. All electrodeposits were plated to a total passed charge of 30 Ccm^{-2}, with the passed charge divided evenly between layers for the multilayer coatings. For simplicity, these multilayer coatings will be denoted as M2a and M4a, for the two and four layer coatings with AZZ40 as the base material, and M2b and M4b, for the two and four layer coatings with AZZ80 as the base material. A pure zinc coating, electrodeposited from the aqueous zinc bath, was included for comparison. The immersion tests were continued until red rust was observed on at least 5% of the surface of each sample. A description of the tested electrodeposits is included in Table 2.3, along with the observed protection times for the steel substrate, and the average of the corrosion potentials measured in days 6-10.

Table 2.3 Electrodeposits used for 50 mM NaCl immersion testing.

Label	Deposition Protocol	E_{corr}	Cathodic protection time	Time to red rust
Zn	40 $\mathrm{Am^{-2}}$, 30 $\mathrm{Ccm^{-2}}$	-0.749 V vs SHE	21 d	21 d
AZZ80	80 $\mathrm{Am^{-2}}$, 30 $\mathrm{Ccm^{-2}}$	-0.582 V vs SHE	36 d	37 d
AZZ40	40 $\mathrm{Am^{-2}}$, 30 $\mathrm{Ccm^{-2}}$	-0.611 V vs SHE	43 d	75 d
M2a	40 $\mathrm{Am^{-2}}$, 15 $\mathrm{Ccm^{-2}}$ 80 $\mathrm{Am^{-2}}$, 15 $\mathrm{Ccm^{-2}}$	-0.614 V vs SHE	64 d	86 d
M2b	80 $\mathrm{Am^{-2}}$, 15 $\mathrm{Ccm^{-2}}$ 40 $\mathrm{Am^{-2}}$, 15 $\mathrm{Ccm^{-2}}$	-0.617 V vs SHE	65 d	73 d
M4a	40 $\mathrm{Am^{-2}}$, 7.5 $\mathrm{Ccm^{-2}}$ 80 $\mathrm{Am^{-2}}$, 7.5 $\mathrm{Ccm^{-2}}$ 40 $\mathrm{Am^{-2}}$, 7.5 $\mathrm{Ccm^{-2}}$ 80 $\mathrm{Am^{-2}}$, 7.5 $\mathrm{Ccm^{-2}}$	-0.669 V vs SHE	69 d	89 d
M4b	80 $\mathrm{Am^{-2}}$, 7.5 $\mathrm{Ccm^{-2}}$ 40 $\mathrm{Am^{-2}}$, 7.5 $\mathrm{Ccm^{-2}}$ 80 $\mathrm{Am^{-2}}$, 7.5 $\mathrm{Ccm^{-2}}$ 40 $\mathrm{Am^{-2}}$, 7.5 $\mathrm{Ccm^{-2}}$	-0.631 V vs SHE	51 d	59 d

During the immersion tests, the corrosion potential of each sample was measured at 24 hour intervals, as shown in Figure 2.9. The bare steel electrode was found to have an initial corrosion potential of -0.29 V vs SHE, dropping to a steady state of approximately -0.41 V vs SHE after 72 hours. Thus potentials below the horizontal dotted line in Figure 2.9, drawn at -0.51 V, indicate that the coating induces more than 100 mV of cathodic polarization, which is generally considered to signify substantial cathodic protection. The 'x' markings in Figure 2.9 indicate the points at which red rust was observed to cover at least 5% of the sample surface, and is considered the point of failure for each coating in this study.

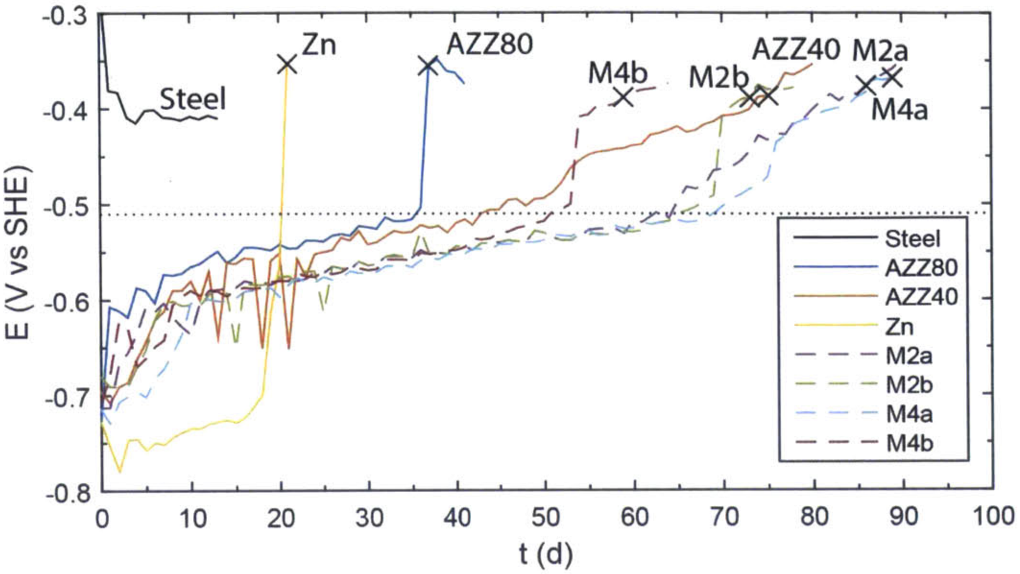

Figure 2.9 Corrosion potential of Al-Zn-Zr alloy single and multilayer electrodeposits during immersion in 50 mM NaCl solution. The formation of red rust on 5% of the visible surface is marked with an 'x'.

All of the electrodeposited coatings were initially found to provide significant cathodic protection to the steel substrate. The strongest cathodic protection was provided by the pure zinc coating, which had the lowest corrosion potential of all the tested coatings for the first 19 days of the test. During this time the zinc coating became rapidly covered with voluminous white corrosion products, w hich detached easily from the surface with gentle rinsing. However, the zinc coating also exhibited the shortest lifetime of the tested coatings, with abrupt failure of cathodic protection and red rust formation observed at day 21.

The Al-Zn-Zr single layer electrodeposits, in comparison, exhibited a more modest degree of cathodic protection but substantially increased overall protection time relative to pure zinc. The coarse-grained AZZ80 deposit had an initial corrosion potential of -0.69 V, which increased to rapidly to -0.60 V after 24 hours, followed by a slow but steady increase to -0.51 V after 38 days. During this period, the coating became covered with a highly adherent layer of black corrosion products. The coating then underwent abrupt failure similar to that observed in the pure zinc coating, with a jump in the corrosion potential to -0.35 V and the immediate formation of visible red rust. The corrosion potential of the nanocrystalline AZZ40 deposit showed an initially similar pattern, rising quickly from -0.69 V to -0.60 V over 5 days, then much more slowly to -0.51 V after 43 days. The surface of the AZZ40 coating was covered with a highly adherent layer of white corrosion products during this period. However, whereas the AZZ80 coating experienced abrupt failure after cessation of cathodic protection, the potential of the AZZ40 coating drifted up slowly and gradually to that of bare steel, and the formation of red rust was delayed until day 75, just over twice the protection time observed for the AZZ80 coating.

The observed patterns of corrosion damage to the AZZ80 and AZZ40 coatings in Figure 2.10 (a-f) show a few characteristic differences. The image of the AZZ80 coating after 20 days immersion indicates that the coating experienced highly localized damage, with a heterogeneous distribution of corrosion products, and steel substrate visible beneath through-going pits and in areas where the coating had receded from the edges of the sample. Accordingly, the red rust in the image of the AZZ80 coating after 40 days is largely concentrated in two corners of the sample, while a sizable area in the center remains apparently intact. The corrosion damage to the AZZ40 coating, by contrast, appeared to occur quite uniformly over the surface, and the image in Figure 2.10 (e) shows that even after 40 days the steel substrate was almost completely covered, while the red rust visible in Figure 2.10 (f) emerged slowly and uniformly over a large area.

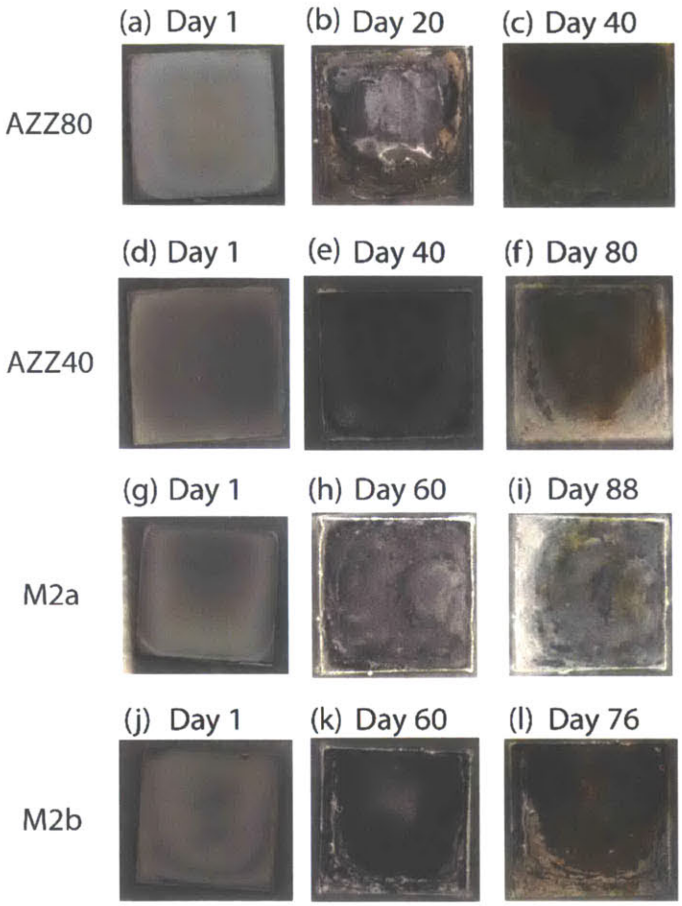

Figure 2.10 Images of Al-Zn-Zr electrodeposits following immersion in 50 mM NaCl.

In general, the tested multilayer electrodeposits exhibited improved corrosion protection relative to their monolithic counterparts. The multilayer electrodeposits had cathodic protection times ranging from 51 to 69 days, all of which exceeded the 43 days observed for the highest performing monolithic AZZ40 coating. In addition, the two deposits M2a and M4a, both of which used the nanocrystalline/amorphous AZZ40 as a base layer, were able to delay red rust formation for 86 and 90 days respectively, relative to 75 days for the AZZ40 monolithic coating. However, the two deposits M2b and M4b, which used the coarse-grained AZZ80 as a base layer, showed red rust after 73 and 59 days, and so both slightly underperformed the monolithic AZZ40 coating according to this measure. This observed trend is consistent with results in other studies of multilayer corrosion coatings, which generally find that multilayer coatings perform better when more corrosion-resistant materials are used as a base [80,81], and is likely explained by the preferential dissolution of the AZZ80 base layer, resulting in the undercutting and mechanical failure of the AZZ40 layers on top. This is supported by a comparison between the corrosion behavior of the M2a and M2b bilayer coatings. While the cathodic protection times for M2a and M2b were very similar, the images of the corroded M2a and M2b coatings in Figure 2.10 (g-l) show starkly different distributions of corrosion damage and failure mechanism. The corrosion damage to the M2a coating after 60 days shown in Figure 2.10 (h) is almost completely uniform in appearance, while the M2b coating after 60 days shown in Figure 2.10 (k) has numerous pits and has receded substantially away from the edge of the sample, exposing steel substrate. Accordingly, in the M2a coating, red rust formation was delayed for 22 days following the loss of cathodic protection, and occurred gradually and uniformly over the surface, as shown in Figure 2.10 (i). The M2b coating, in contrast, developed red rust only 8 days after the loss of cathodic protection, and was accompanied by substantial mechanical failure, i.e., visible as cracks in the outer AZZ40 layer in Figure 2.10 (l). The distribution of red rust in Figure 2.10 (l) also indicates that the most severe corrosion damage occurred in regions where the outer layer was largely intact, while the exposed steel in the bottom of the image was largely free of red rust. This suggests that the geometry of the M2b bilayer deposit may have exacerbated localized corrosion by causing crevice corrosion in the highly concentrated electrolyte trapped below the intact AZZ40 barrier layer. The use of the more resistant AZZ40 material as a base in the M2a bilayer, conversely, appears to act to distribute corrosion damage more evenly over the surface and delays the exposure of steel substrate, maximizing the useful lifetime of the coating.

2.8 Conclusion

The following conclusions can be drawn from this investigation of electrodeposition of binary Al-Zn and ternary Al-Zn-Mn and Al-Zn-Mn alloys from $AlCl_3$-EMIC:

- Binary Al-Zn thin films were successfully produced with zinc content ranging from 31 to 75 at.%, and current densities ranging from 24 to 100 Am^{-2}. The binary electrodeposits exhibit a dual phase microstructure consisting of a mixture of hcp Zn dendrites and an fcc Al matrix. Dendrite growth is associated with high surface roughness and porosity in the high zinc binary deposits. Zinc dendrite formation would be expected to degrade the properties of single and multilayer aluminum alloy corrosion coatings, by providing initiation points for pit formation, and increasing the chance of through-going pores and defects in the coating.

- The undesirable structure of binary Al-Zn deposits is not improved by ternary alloying with Mn, which instead decreases incorporation of Zn into the Al matrix, resulting in larger zinc dendrites and increased surface roughness for the low current density deposits.
- An improved structure is promoted by ternary alloying with 5-10 at.% Zr, which significantly refines the microstructure and promotes chemical homogeneity in the deposit; XRD peak broadening suggests the formation of nanostructured or even amorphous regions in these deposits. This results in decreased surface roughness for the low current density deposits, with a nodular surface morphology. This structure is viewed as beneficial for corrosion protection. When produced under nominally similar deposition conditions, coarse-grained Al-Zn-Zr electrodeposits have a pitting potential ~40 mV higher than the Al-Zn binary deposits, and when the nanocrystalline/amorphous phase appears in the ternary deposit there is a further increase of ~70 mV in the pitting potential.
- The ternary Al-Zn-Zr electrodeposits have substantially improved ability to protect steel substrates when immersed in 50 mM NaCl solution, delaying the formation of red rust for 75 days, in comparison to 21 days for pure Zn. What is more, such homogeneous alloys can be used to great effect in multilayer stacks that further enhance the protection time. Specifically, multilayer Al-Zn-Zr electrodeposits show additional improvement in protection time up to 90 days for a four layer deposit, when the nanocrystalline/amorphous ternary alloy is used as a base layer.

Based on this work, the Al-Zn-Zr electrodeposition protocol examined here appears to be a viable approach to single-bath Al-Zn alloy coatings, due to the ability to deposit high quality layers, with tunable corrosion properties. This in turn permits the modulation of both composition and microstructure, with demonstrated improvements in corrosion protection as compared with monolithic coatings.

3. Time-dependent simulation and optimization of galvanic corrosion of multilayered coatings

In this chapter, we describe our general approach to simulation of galvanic corrosion of multilayered coatings via the finite element method. The model is first applied to a test system consisting of a galvanic couple consisting of a multilayered or functionally graded zinc alloy coating, and an exposed area of mild steel substrate, as at a scar, cut edge, or other defect. The materials used in this model are hypothetical, with typical corrosion kinetics taken from the literature, and thus the simulations are not intended to apply directly to any real-world scenario; instead this chapter may be viewed as a demonstration and proof of principle of the modeling and optimization technique that we have developed.

3.1 Model

3.1.1. Model system geometry

We select for our demonstration system a substrate coated with a sacrificial (galvanic) coating. We envision a multilayer coating in which each layer is more active than the one beneath it, and all layers are expected to undergo active dissolution in the electrolyte. The basic geometry of the system is selected to capture the effect of localized galvanic protection near a scar in the coating which penetrates to the substrate. The prospect for improved corrosion resistance in this system is thus based on the galvanic interaction not only between coating and substrate, but between the various layers in the coating structure, which may coordinate their sacrificial corrosion rates in complex ways to control the recession of the coating structure from the scar. The requirement for outer layers to be more active than inner ones is chosen for simplicity and to improve the stability of the model results, since more active inner layers will tend to increase variability due to localized corrosion of the underlying layers at pores or flaws in the more noble outer layers.

We consider a radially symmetric system consisting of a coated substrate, under an aerated electrolyte solution of constant depth $D = 1\ \mathrm{mm}$, and surrounded by insulated walls at radius $R = 10\ \mathrm{mm}$. The dimensions of the system were chosen to approximate the semi-infinite condition, as increasing either was not found to significantly affect model results. It is assumed that the variation in the thickness of the coating is small relative to the lateral dimensions of the system, so that variations in the z-coordinate of the metal-electrolyte interface can be neglected. Thus, the system is 2-D axisymmetric, and the geometry of the electrolyte is approximated as a cylinder as shown in Figure 3.1 (a).

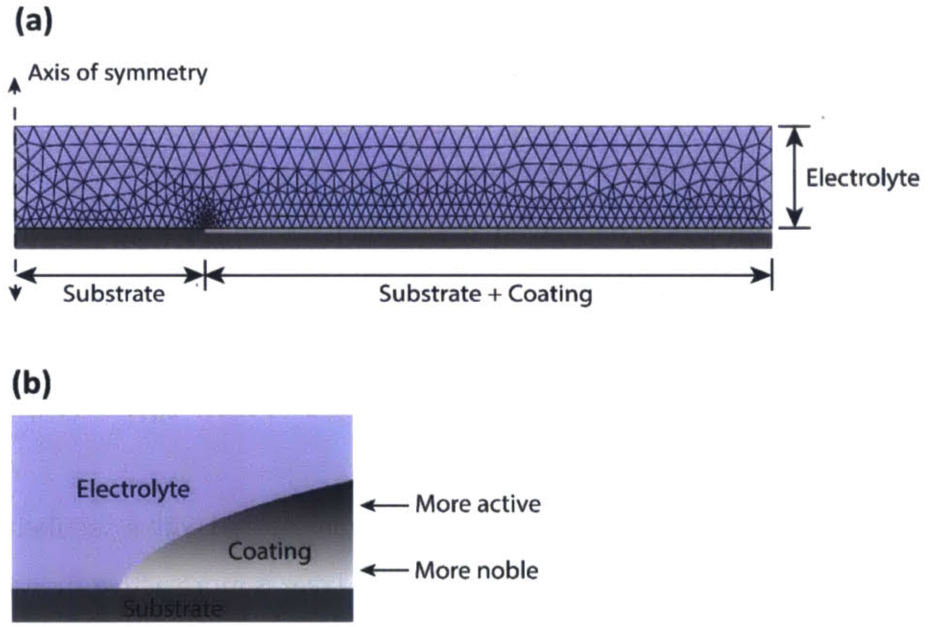

Figure 3.1 (a) Finite element mesh used for model calculations. (b) Schematic of edge of compositionally graded coating adjacent to exposed substrate.

For any given time *t*, the coating geometry is described by a function $h(r,t)$, giving the coating thickness at a radial distance *r* from the center of the defect. The initial coating has a thickness of $h_0 = 20\ \mu\text{m}$, and there is a gap in the coating around the center of the system with inner radius $r_0 = 0.5\ \text{mm}$, outer radius $r_1 = 1\ \text{mm}$, and linearly sloped sides. This initial geometry is described analytically as:

$$h(r,t=0) = \begin{cases} 0\ \mu\text{m} & \text{if } r \leq 0.5\ \text{mm} \\ \left(\dfrac{r - 0.5\ \text{mm}}{0.5\ \text{mm}}\right) \times 20\ \mu\text{m} & \text{if } 0.5\ \text{mm} < r < 1.0\ \text{mm} \\ 20\ \mu\text{m} & \text{if } r \geq 1.0\ \text{mm} \end{cases} \qquad (3.1)$$

The r-coordinate is discretized into 10,000 cells spaced equally at $\Delta r = 1$ μm, and the value of $h(r,t)$ stored independently for each cell. $h(r,t)$ is also permitted to be negative, to represent penetration into the substrate. The initial coating thickness function $h(r,0)$, along with a representative thickness function from a later time $h(r,t_0)$ are shown in Figure 3.2.

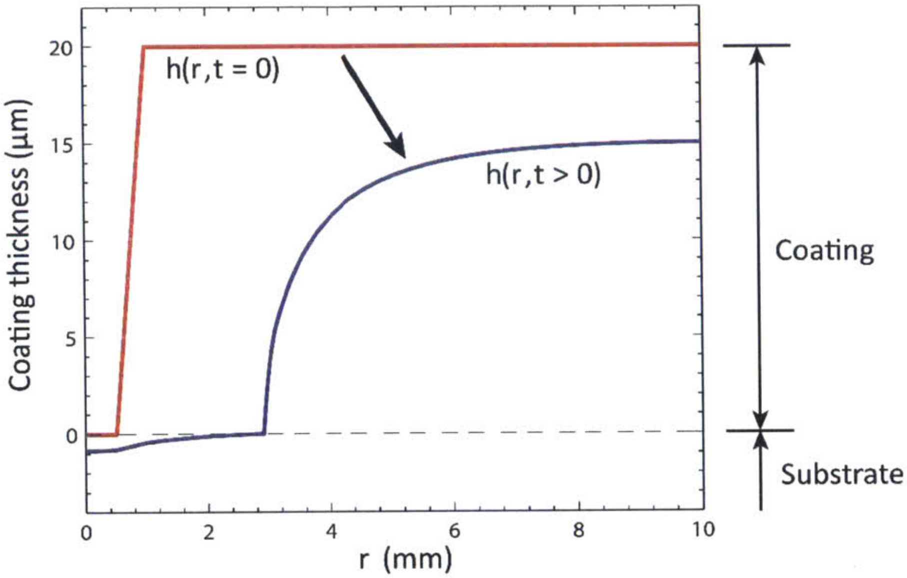

Figure 3.2 Coating thickness function $h(r,t)$ at $t = 0$ and at a representative future time $t > 0$.

For the simulation of layered and graded structures, we allow the electrochemical properties of the coating to vary based on depth. For this study, in order to qualitatively capture the effects of compositional gradients on corrosion behavior, the rate of coating dissolution is allowed to vary exponentially based on a depth-dependent composition parameter $\alpha(h)$, as further described in the next section. This permits the model to account for the effects of alloying elements that either inhibit or enhance the dissolution of the coating in a straightforward way, though it neglects possible complications such as dealloying and phase separation.

3.1.2. Governing equations

For the sake of simplicity we assume that the variation in conductivity is negligible throughout the electrolyte, and therefore the electrolyte behaves as a uniform ohmic conductor with conductivity κ. The local potential of the electrolyte is given by the potential field ϕ. Thus within the electrolyte the current density is given by:

$$\vec{\imath} = -\kappa \cdot \nabla\phi \tag{3.2}$$

Therefore, in order to maintain local electroneutrality, the potential ϕ must satisfy the Laplace equation:

$$\nabla^2\phi = 0 \tag{3.3}$$

within the electrolyte.

At each metal/electrolyte interface, we assume that the available electrochemical reactions are oxygen reduction and metal oxidation:

$$\mathrm{O_2 + 2H_2O + 4e^- \rightarrow 4OH^-} \tag{3.4}$$

$$\mathrm{M} \rightarrow \mathrm{M}^{n+} + n\mathrm{e}^- \tag{3.5}$$

Both of these reactions are taken to be irreversible, due to the large gap between the standard reduction potential for oxygen reduction ($E^0 = +1.22$ V vs SHE), and that of iron or zinc dissolution ($E^0 = -0.45$ V vs SHE for iron, and $E^0 = -0.76$ V vs SHE for zinc). The rate of the oxidation reaction is assumed to have an exponential dependence on potential, resulting in an anodic current density of the form:

$$i_{\mathrm{a,Fe}} = 2Fk_{\mathrm{Fe}} \exp\left(\frac{E - E^0_{\mathrm{Fe}}}{\beta_{\mathrm{Fe}}}\right) \tag{3.6}$$

$$i_{\mathrm{a,Zn}} = 2Fk_{\mathrm{Zn}} \exp\left(\frac{-\alpha(h)}{\beta_{\mathrm{Zn}}}\right) \exp\left(\frac{E - E_{\mathrm{Zn}}^{0}}{\beta_{\mathrm{Zn}}}\right) \tag{3.7}$$

where F is the Faraday constant, E is the local electrode potential, k_{Fe} and k_{Zn} are are the interfacial rate constants for iron and zinc dissolution, E_{Fe}^{0} and E_{Zn}^{0} are the standard reduction potentials for iron and zinc, and β_{Fe} and β_{Zn} are the anodic Tafel parameters for iron and zinc. Equation (3.6) is employed along the interface where $h(r,t) \leq 0$, as the iron substrate is exposed to the electrolyte, while Equation (3.7) is employed in regions where $h(r,t) > 0$, where the zinc-alloy coating is present. The composition parameter $\alpha(h)$ in Equation (3.7) modifies the dissolution current of the zinc-alloy coating based on the composition of the exposed region of the coating. The parameter $\alpha(h)$, expressed in units of potential, is normalized by the Tafel slope β_{Zn} for convenience, so that α corresponds to the expected change in corrosion potential for the alloy relative to that of pure zinc. Thus, regions of the coating with positive values for $\alpha(h)$ are more noble, and dissolve more slowly, while regions of the coating with negative $\alpha(h)$ are more active.

The local electrode potential E gives the difference in potential between charge in the metal and charge in the electrolyte just outside the double layer, as measured relative to the Standard Hydrogen Electrode (SHE). Due to the high conductivity of the metal, variations of potential are expected to be negligible within the metal, and thus the potential of the metal can be taken to be zero everywhere. Thus

$$E(r) = -\phi(r, z = 0) \tag{3.8}$$

We assume in this model that the cathodic reaction, oxygen reduction, is fully rate-limited by mass transport of dissolved oxygen to the metal surface. This has been shown to be quite a good approximation for the great majority of sacrificially coated systems the model is intended to simulate, in particular Zn coatings on steel or Fe substrates [82–84]. Therefore, the cathodic current density is considered to be independent of potential:

$$i_{\mathrm{c}} = i_{\mathrm{L,O_2}} \tag{3.9}$$

where $i_{\mathrm{L,O_2}}$ is the limiting current density associated with the maximal rate of oxygen diffusion to the metal surface.

3.1.3. Boundary conditions

The sides and top of the systems are insulted, and so a zero-current condition is imposed

$$\hat{n} \cdot \nabla\phi = 0 \tag{3.10}$$

where $\hat{n}$ is a unit vector normal to the boundary.

These equations and boundary conditions were used to solve for the steady state potential distribution, and hence determine local anodic dissolution rates. Along the electrolyte/metal interface, subtracting the cathodic current density in Equation (3.9) from the anodic current density in Equation (3.6) or Equation (3.7), depending on the locally exposed metal, gives total local current density due to electrochemical reactions:

$$i_{\mathrm{tot}} = \begin{cases} 2Fk_{\mathrm{Fe}} \exp\left(\dfrac{E - E_{\mathrm{Fe}}^0}{\beta_{\mathrm{F}}}\right) - i_{\mathrm{L,O_2}} & \text{if } h \leq 0 \\ 2Fk_{\mathrm{Zn}} \exp\left(\dfrac{-\alpha(h)}{\beta_{\mathrm{Zn}}}\right) \exp\left(\dfrac{E - E_{\mathrm{Zn}}^0}{\beta_{\mathrm{Zn}}}\right) - i_{\mathrm{L,O_2}} & \text{if } h > 0 \end{cases} \tag{3.11}$$

while comparison with Equation (2) generates the boundary condition:

$$\frac{\partial\phi}{\partial z} = -\frac{1}{\kappa} i_{\mathrm{tot}} \tag{3.12}$$

3.1.4. Kinetic parameters

Due to its ubiquity and high level of scientific and industrial significance, parameters were selected to approximate a system comprising a zinc-alloy coating on an iron substrate, in a neutral aerated electrolyte containing NaCl. Parameter values were taken from the literature, in experimental conditions matching the modeled system as closely as possible. The concentration of Na^+ and Cl^- ions was set to 10 mM, in order to observe changes in the efficiency of galvanic protection over the length scales used in the model. Kinetic parameters for the coating were taken to be the same as for pure zinc, with the effect of the alloying seen in modification of the dissolution rate of the zinc-alloy coating by the depth-dependent factor $\exp(\alpha(h))$. We permit $\alpha(h)$ to vary in the range $-50\ \mathrm{mV} \leq \alpha(h) \leq +50\ \mathrm{mV}$, such that the corrosion potential of the alloy varies by $\pm 50\ \mathrm{mV}$ relative to that of pure zinc. This variation is attributed to minor alloying effects presumably used to induce structure in the coating; this range of tenability is well within the range reported experimentally [29,85].

It has been found experimentally that for both carbon steel and zinc the limiting current for O_2 reduction is dependent on the surface condition of the metal, in particular the existence of oxide films and precipitated corrosion products, which act as a barrier to mass transfer [82–84]. In addition, zinc-based corrosion products have been shown to be more strongly protective than iron-based corrosion products in neutral aerated sodium chloride solutions, resulting in decreased corrosion of zinc relative to carbon steel in atmospheric and immersed corrosion [84]. In this study the limiting O_2 reduction current is taken to be constant for each metal, and equal to average experimentally observed rates of O_2 reduction in long-term studies of corrosion of each metal in seawater [86]. This approach allows the model to account for the effect of surface modification due to corrosion in a straightforward and computationally tractable way, but neglects factors such as the accumulation of corrosion products over time and the effect of pH variations in the coupled system. Thus, the present simulations are not intended to show exact quantitative agreement with experiments, particularly in conditions of high corrosion rates. A list of the kinetic parameters used for the model results presented in this paper is given in Table 3.1. The theoretical polarization curves associated with these parameters are shown in Figure 3.3.

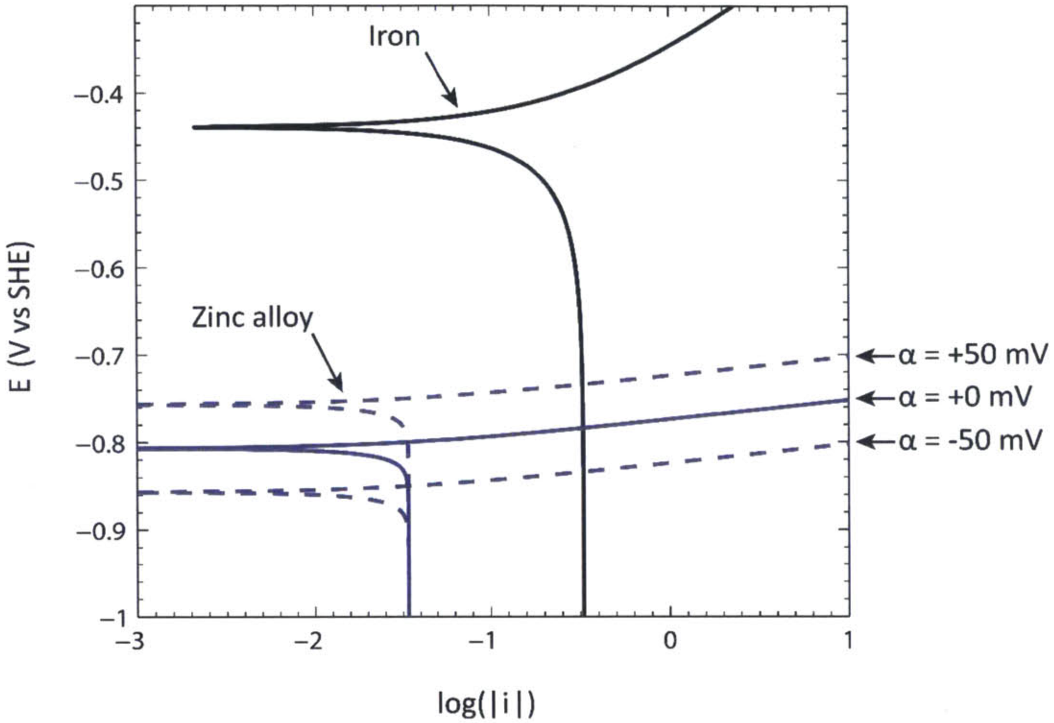

Figure 3.3 Simulated polarization curves for iron substrate, zinc alloys with composition parameter α ranging from -50 mV to 50 mV

Table 3.1 Electrochemical parameter values used in the model.

κ	0.013 S/m [49]
k_{Zn}	2.32×10^{-5} mol/(m^{2}s) [4]
i_{L,O_2}(Zn surface)	0.33 A/m^2 [44]
k_{Fe}	1.45×10^{-6}mol/(m^{2}s) [4]
i_{L,O_2}(Fe surface)	0.034 A/m^2 [44]
$E^0_{Zn^{2+}/Zn}$	-0.76 (V vs SHE)
$E^0_{Fe^{2+}/Fe}$	-0.45 (V vs SHE)
β_{Zn}	0.022 V [4]
β_{Fe}	0.154 V [4]

3.1.5. Generation of time-dependent corrosion simulations

Given a coating geometry function $h(r, t_0)$, the geometry and basic equations described in sections (3.1.1)-(3.1.4) are input into the COMSOL Multiphysics solver via the LiveLink for Matlab software package. The COMSOL software generates a triangular finite element mesh over the electrolyte geometry, with finer elements used near the substrate-coating interface and coarser elements in the bulk electrolyte. As the coating thickness is much smaller than the system dimensions, the electrolyte domain is approximated as a cylinder for all values of $h(r, t_0)$. The electrolyte potential function satisfying all the governing equations and boundary conditions is then computed and returned to Matlab for further analysis. An example of the finite element mesh over the electrolyte geometry for a representative Fe-Zn galvanic couple is shown in Figure 3.1 (a), along with a schematic diagram of the geometry of the coating edge in Figure 3.1 (b). The potential field is used to calculate the local electrode potential $E(r)$ along the surface according to Equation (3.8).

In order to simulate time-dependent evolution of the coating geometry, steady state solutions are repeatedly calculated, and used to determine local dissolution rates, which are then integrated to evolve the coating structure. Given a steady state solution to the model with input geometry function $h(r, t_0)$ the calculated local anodic currents $i_a(r)$ are used to calculate the updated coating thickness $h(r, t_0 + \Delta t)$. Since the anodic current is assumed to come from irreversible metal dissolution, the instantaneous rate of change to the thickness of the coating is:

$$\frac{\partial h(r, t_0)}{\partial t} = -i_{\mathrm{a}}(r)\left(\frac{A_{\mathrm{M}}}{nF\rho_{\mathrm{M}}}\right) \tag{3.13}$$

where A_M is the atomic mass, ρ_M is the density, *n* is the valence, and *F* is the Faraday constant.

During each time step, a first-order approximation is used to to generate a new coating geometry via Equation (13). In order to do this, the potential $E_0(r, t_0)$ is first determined from the initial geometry $h(r, t_0)$. The time derivative $\frac{\partial E}{\partial t}$ is estimated from a finite difference of the electrode potentials from the start and end of the previous time step. These values are used to give a first order approximation for *E* over the time interval:

$$E(r,t) = E_0(r,t_0) + \frac{\partial E}{\partial t}(t - t_0) \tag{3.14}$$

This is used to calculate the final coating geometry $h(r, t + \Delta t)$ by integrating Equation (3.13) over the time interval. In order to maximize both computational efficiency and control error, an adaptive time step size algorithm is applied to the integration time step. The estimated electrode potential function at the end of a time step is compared to the computed steady state potential function for the updated coating geometry. In order to maintain an appropriate time step size, tolerances δ_0 and δ_1 were determined such that:

$$\delta_0 \leq \max\{|E_0(r) - E_1(r)|\} \leq \delta_1 \tag{3.15}$$

The time step is adjusted so that this condition is satisfied during each step. As it is difficult to place a rigorous bound on overall error using this method, convergence testing was performed over a range of coating compositions and choices of tolerances. Tolerance values of $\delta_0 = 2$ and $\delta_1 = 5$ mV were found to deliver an average of less than 2% error, and less than 5% in all cases, over a wide range of different coatings at a reasonable computational cost, and so were used in all of the simulations reported below.

3.2.1 Demonstration of coating layering effects

As a first demonstration of the potential benefit of layering or grading a coating structure for galvanic protection, we compared three simple coating structures depicted in Figure 3.4, all of which have the same average reduction potential and the same total thickness: (a) a monolithic pure Zn coating, (b) a bilayer structure with a noble inner layer and active outer layer, and (c) a naïve gradient structure with a linear potential profile through the coating thickness. The associated composition parameter function for each of the three coatings is shown in Figure 3.4. Simulations were run to model the dissolution of each of the coatings over a period of up to 80 days. The evolution of the coating geometry and local electrode potential for each of the coatings can be seen in Figure 3.4. The corrosion potential of uncoated iron is shown as well in Figure 3.4 (c), to illustrate the degree of cathodic protection afforded by each of the coatings over the simulation period. The evolution of the diameter of exposed substrate and maximum penetration of corrosion into the substrate for each of the coatings are shown in Figure 3.5 (a) and (b), respectively.

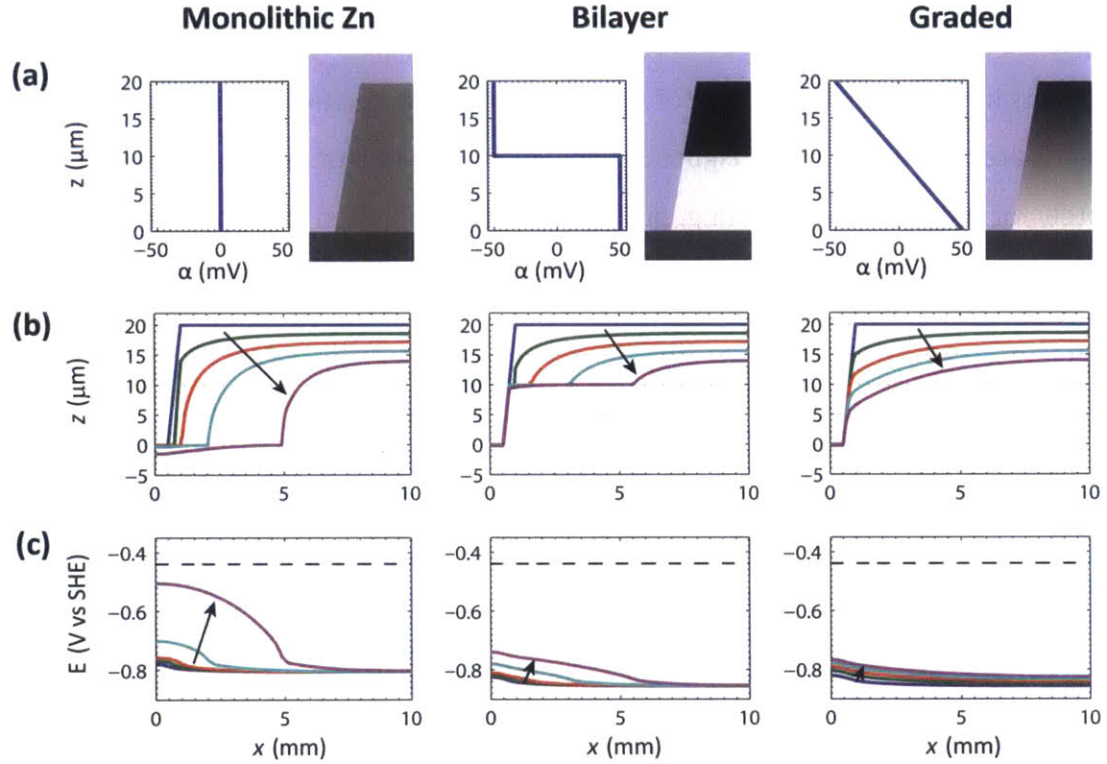

Figure 3.4 (a) Coating composition, (b) evolution of simulated coating geometry, and (c) evolution of simulated electrode potential for monolithic, bilayer, and smoothly graded coatings. The corrosion potential of uncoated iron is shown as the dashed line in (c). Lines are drawn at 0, 10, 20, 30, and 40 days.

Cathodic protection due to a sacrificial coating is generally considered to be effective when the level of cathodic polarization exceeds 100 mV [87]. Thus it is clear from Figure 3.5 that all three coatings are successful at protecting the exposed iron at the beginning of the simulation period. However, examination of Figure 3.5 shows dramatically different behavior of the coatings as the simulation progresses. In the case of the monolithic coating, coating dissolution occurs preferentially at the coating-substrate interface. As a result, the coating rapidly recedes, increasing the area of exposed substrate. In contrast, in the bilayer coating the noble inner layer is initially sacrificially protected by the active outer layer. Therefore coating dissolution occurs preferentially above the interface between the two coating layers, and exposure of additional substrate is inhibited until the outer layer has receded significantly. The same effect can be observed in the graded coating, in which the active outer portions of the coating sacrificially protect the nobler inner portions. Although the graded coating distributes corrosion more continuously than the bilayer, in both cases the composite structure of the coating results in substantial inhibition of substrate exposure, relative to the monolithic case. These trends are clearly evident in Figure 3.5, in which the width of exposed substrate increases immediately for the monolithic coating, but is almost fully inhibited for approximately 40 days for the bilayer and 60 days for the graded coating.

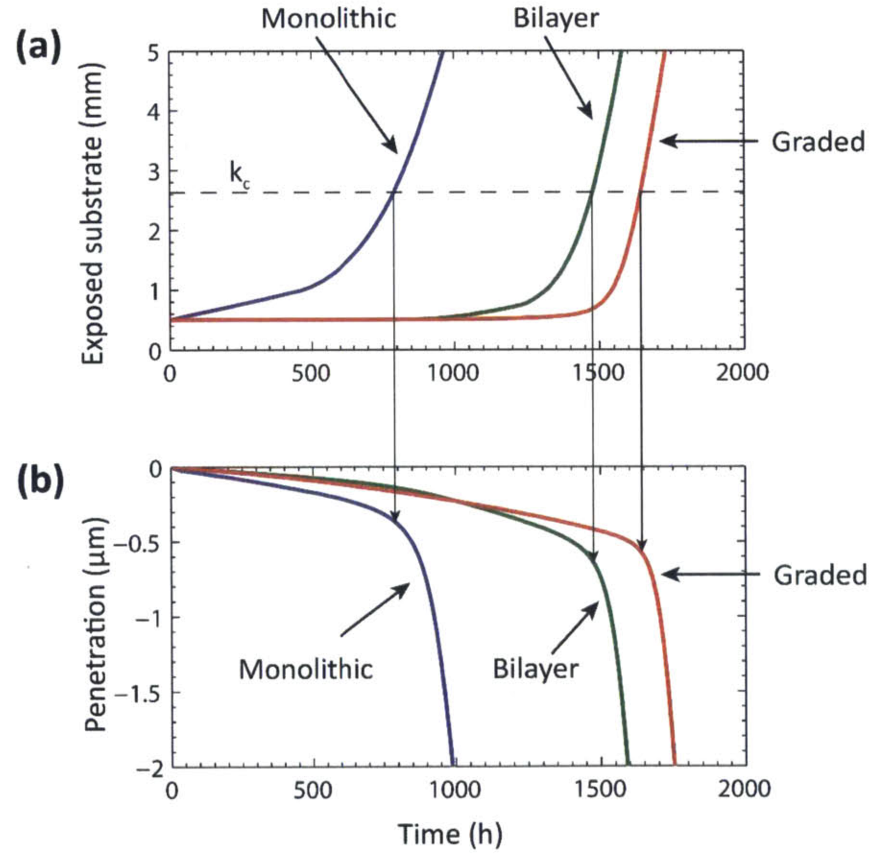

Fig 3.5 Radius of exposed substrate and penetration depth of corrosion into the substrate for monolithic, bilayer and smoothly graded coatings.

In each of the simulations, as the coating recedes its effectiveness at applying cathodic protection to the center of the defect decreases. One commonly used measure of the range of cathodic protection is given by the Wagner parameter, which gives the characteristic length scale over which the electrode potential can be expected to remain relatively constant over a coplanar galvanic couple [34]. The Wagner parameter is defined as

$$k_{\mathrm{c}} = \kappa |\mathrm{d}E/\mathrm{d}J| \tag{3.16}$$

where κ is the solution conductivity, and $|\mathrm{d}E/\mathrm{d}J|$ is the polarization resistance of the electrode. For the simulated system, the calculated Wagner parameter for the iron surface at its free corrosion potential is equal to $k_{\mathrm{c}} = 2.63\ \mathrm{mm}$. This length scale is plotted for reference on the substrate exposure curves of Figure 3.5, with a horizontal dashed line. For each of the three simulations, soon after the radius of exposed substrate reaches this value, the rate of substrate penetration increases very rapidly, indicating a loss of cathodic protection at the center of the defect.

3.2.2 Quantification of coating performance

In order to quantitatively compare coating structures, it is useful to define a criterion to evaluate the effectiveness of each coating at protecting the substrate from corrosion. In experimental studies of galvanic coatings, a wide array of measures of the effectiveness of corrosion protection or corrosion resistance have been employed, such as weight loss measurements, polarization resistance, or the neutral salt spray test [3,18,23,27,88]. However, all of these metrics have the potential to produce misleading results, since they only indirectly account for the effects of corrosion damage. For instance, the widely used neutral salt spray test evaluates coatings on their ability to inhibit surface rust formation, but does not consider whether they are able to prevent localized corrosion at pores or flaws in the coating. This is a particular concern for composite coatings that incorporate elements such as Ni that are noble relative to the iron substrate. A Ni barrier layer that confines corrosive attack of the substrate to the small surface area accessible through pores in the coating may minimize the appearance of red rust and improve performance on the salt spray test, but decrease the ultimate service life of the iron due to rapid localized corrosion. Thus, particularly as simulations can provide complete information about the state of the system, it is beneficial to define a criterion that evaluates the performance of the coating based on direct measurement of the desired outcome.

In a wide range of engineering applications, such as pipelines, ship hulls, or storage tank walls, the purpose of a sacrificial coating is to delay failure due to leaks caused by penetration of corrosive attack through the depth of the steel. Therefore in this study we have chosen to measure the protectiveness of the coating based on the length of time for which the coating prevents penetration of the substrate beyond a threshold value. Based on the patterns in Figure 3.5, there is period of cathodic protection during which substrate penetration occurs slowly, followed by a sudden rapid increase as cathodic protection is lost due to the recession of the coating. During this protected period, the total substrate penetration remained under ~400 nm in all cases, whereas following the loss of cathodic protection the penetration rate quickly approached a constant, coating-independent value: the free corrosion rate of the iron surface. Therefore, for this study we define coating failure to have occurred when substrate penetration reaches 1 μm. Since this is significantly greater than the maximum penetration during the protected phase, this failure criterion should act as a robust indicator of the duration of cathodic protection. As the rate of substrate loss becomes independent of the coating following loss of cathodic protection, increasing the threshold value further would increase the calculated time to failure for all coatings uniformly, and so would not be expected to provide additional information on the relative performance of the various coatings.

Applying this measure to the three simulations shown above, the calculated time to failure for each of the coatings is 920 hours for the monolithic coating, 1530 hours for the bilayer, and 1700 hours for the linearly graded coating, constituting an increase in effective life of 66% and 84% for the bilayer and linearly graded coating, respectively, over monolithic zinc of the same average composition.

3.2.3 Effect of oxygen reduction rate on coating surface

The beneficial effect of composite coating structures in these simulations is enhanced by the relatively low rate of cathodic reactions on the coatings, as compared with the substrate.

As the rate of O_2 reduction on the coating is an order of magnitude less than on the substrate, inhibition of exposure of additional substrate results in significantly lower overall metal dissolution, and therefore increases the lifetime of the coating. This suggests that the improvement in corrosion protection exhibited by the composite coatings is due to synergy between two factors: (i) the wider distribution of coating dissolution, and inhibition of substrate exposure, and (ii) the decreased rate of the oxygen reduction reaction on the coating. To examine the effect of these two factors independently, the simulations of the monolithic Zn, bilayer, and linearly graded coatings were repeated, with the oxygen reduction rate (ORR) on the coating set to be equal to that of the substrate. Due to the higher rate of cathodic reactions, the simulated time period for these coatings was 12 days, after which the coatings had undergone a similar level of dissolution as in the previous cases. The maximum penetration of corrosion into the substrate and extent of substrate exposure for each of the simulations is shown in Figure 3.6.

Comparison of the pattern of coating loss seen in Figure 3.5 and Figure 3.6 show a similar qualitative pattern for the high ORR-rate and low ORR-rate coatings. In both cases, the bilayer and graded coating structures successfully inhibit substrate exposure at the start of the simulation, and distribute the metal dissolution over a wider area. However, in contrast to the results for the low ORR-rate coatings, the composite coating is not effective at decreasing the overall corrosion rate in the high ORR case. The linearly graded coating is only marginally more effective than the monolithic one at delaying substrate loss, while the bilayer coating is more effective than the monolithic one only at short timescales, as can be seen in the substrate exposure and penetration curves in Figure 3.6. The calculated time to failure for each of the coatings was 430 hours for the monolithic and bilayer coatings, and 460 hours for the linearly graded coating, an increase of only 7.0%. Thus, in this analysis, use of coating materials that inhibit cathodic reactions is necessary to realize significant benefit from graded coating structures.

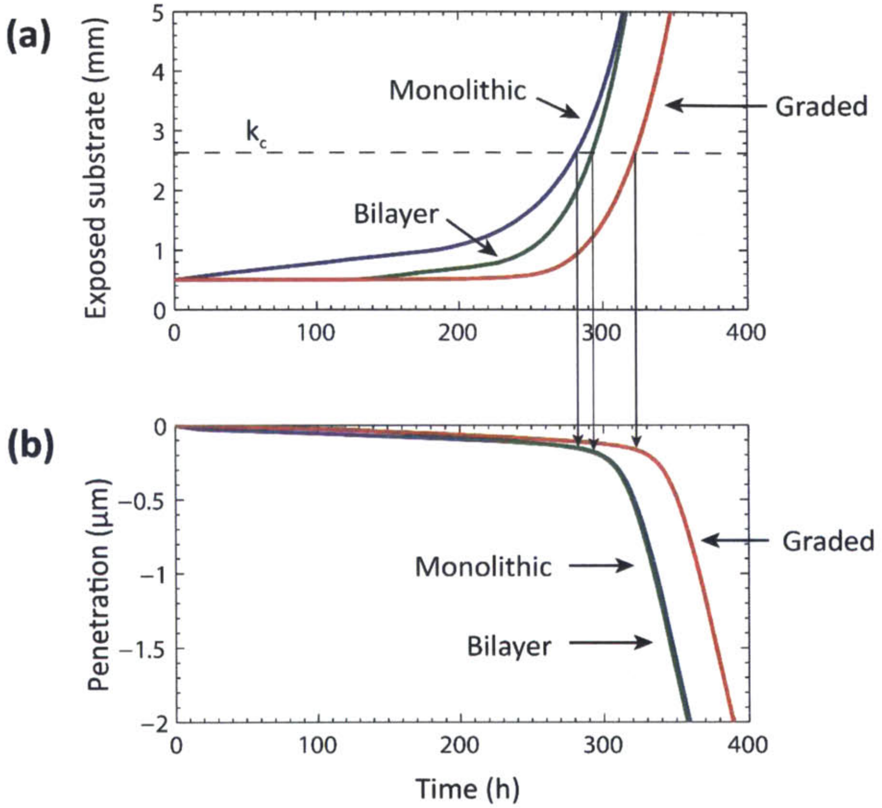

Figure 3.6 (a) Radius of exposed substrate and (b) maximum penetration of corrosion for high ORR-rate coatings. The bilayer and monolithic curves for substrate penetration are indistinguishable.

While these simulations employ an idealized Zn-alloy coating structure that cannot be directly compared to available experimental studies, they suggest a key mechanism that likely contributes to the superior corrosion protection observed for many multilayer coatings. While more active outer layers tend to distribute corrosion over a wider area, coatings with more active inner layers and noble outer layers would be expected to experience exacerbated localized corrosion of the coating at pores and flaws in the outer layer, resulting in degradation of coating performance. In addition, the simulation results provide an explanation for the commonly reported pattern that multilayer coatings with active outer layers and noble inner layers outperform similar coatings with the order of layers reversed [13, 19].

3.2.4. Monte Carlo analysis

The comparison of the continuously graded, bilayer, and monolithic coatings suggests that there is potential for significant improvement in corrosion resistance through compositional modulation of coatings, even among coatings with the same average composition or corrosion potential. However, it is not immediately apparent whether it is possible to further improve performance using an arbitrary non-linear coating structure.

In order to get a sense of trends in performance throughout the space of possible coatings, a Monte Carlo analysis was run on 150 randomized coatings. The coatings were all taken to be 20 μm in thickness, and the composition parameter α was taken to fall in the range $\pm 50\mathrm{mV}$, in accordance with the hypothetical compositions treated by the model. The composition parameter was required to be monotonically decreasing, due to the stability requirements for the model. For this analysis, the coating structure was parameterized by the composition parameter α at 41 equally spaced points throughout thickness of the coating, and the composition parameter function $\alpha(h)$ interpolated from the values at these 41 points. These parameter values are represented as a vector $(\alpha_1, \alpha_2, \cdots, \alpha_{41})$ with the monotonicity requirement $\alpha_j \geq \alpha_{j+1}$. In order to generate random composition vectors representative of the range of possible coatings, a standard recursive subdivision algorithm was employed [89]. For this algorithm, the composition parameter values of the endpoints were first selected randomly, and then the parameter vector was filled in by repeatedly selecting element j among those not yet specified, and then randomly selecting a parameter value α_j for that element, from the range satisfying the monotonicity requirement relative to the already specified elements. The composition parameter function of a sample of the randomized coatings is shown in Figure 3.7 to illustrate the range of coatings produced by this algorithm.

For each of the randomly generated coatings, a simulation was run to measure the time to failure due to penetration of corrosion 1 μm into the substrate. The time to failure was recorded and compared to the average composition parameter value of the coating, given by the mean of the α_j. In addition, 20 monolithic coatings with constant α ranging from $-50\mathrm{mV}$ to $+50\ \mathrm{mV}$ were simulated for comparison. The distribution of time to failure as a function of mean composition parameter for all these simulations is shown in Figure 3.8. The shaded area in Figure 3.8 shows the convex hull of the points sampled in the Monte Carlo analysis, graphically representing the range of coating performance found by the random search.

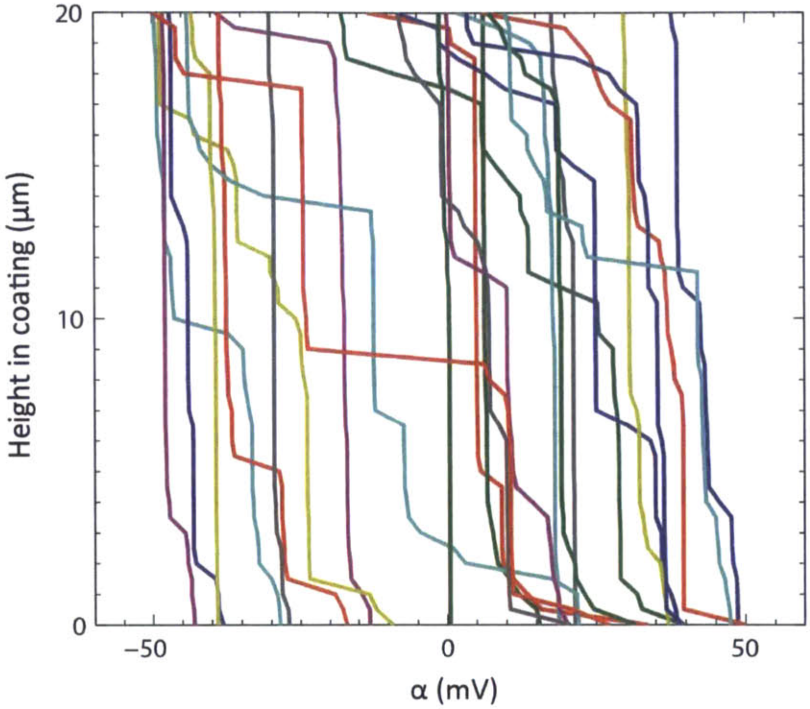

Figure 3.7 Sample of randomized coatings used for Monte Carlo analysis.

The results of the Monte Carlo analysis show that the simulated randomized coatings, in general, significantly outperformed monolithic coatings of the same average composition, and in no cases were found to do worse. This is not surprising, given the results of the simulations of the coatings described in the previous section, and the monotonicity constraint imposed upon the coatings. Since any gradient towards a more active composition on the outer layers of the coating tends to distribute corrosion more widely, and inhibit exposure of additional substrate, any non-uniform monotonic coating will exhibit improved performance over a monolithic coating of equivalent average composition.

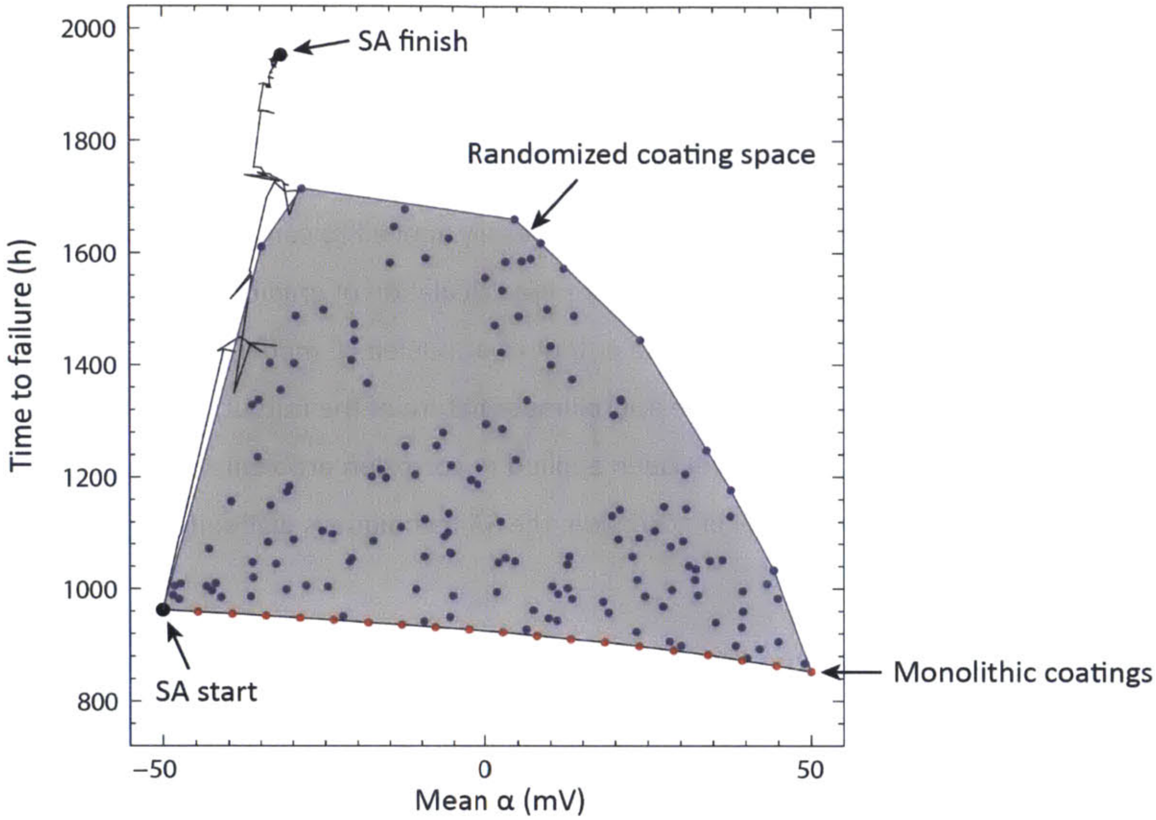

Figure 3.8 Mean α and time to failure for monolithic and randomized coatings. The shaded region represents the space of possible coating performance based on the randomized Monte Carlo sample. The path traced by a representative SA optimization run is shown on the left.

3.3.1. Simulated Annealing (SA)

Given the wide range of coating performance shown by the Monte Carlo analysis, it is reasonable to expect that it may be possible to improve the coating further through use of optimization techniques. Therefore, a SA algorithm is run on the coating structure, to determine a predicted optimal coating and compare its performance to the naïve linear gradient and randomized coatings analyzed thus far.

The SA class of algorithms, first described by Kirkpatrick et al. [90] and by Černý [91], work by analogy with the physical annealing process, with the value of the objective function corresponding to an effective "energy" of the system. Steps that increase the total "energy" are accepted with a finite probability, allowing escape from local minima. SA techniques have been successfully applied to a number of practical optimization problems in engineering, such as design of efficient acoustic filters [92], low cost truss structures [93], and many others [93–96]. Due to its flexibility, SA has several advantages over traditional gradient-based techniques for optimization of engineering designs, as it can be easily applied to complex or non-continuous search spaces, and it does not require the calculation of gradients. Thus SA is often the technique of choice when optimizing the output of a coupled FE model [94,95,97], as gradients cannot be calculated due to the approximate nature of the outputs. While this approach, to our knowledge, has not yet been applied to corrosion problems or coatings, when coupled with a computational model of corrosion, the SA technique is well suited to optimization of coating structures.

As in the case of the Monte Carlo analysis, SA is performed over the space of monotonic coatings of 20 μm thickness, where the composition of the coating was allowed to vary continuously with composition parameter $\alpha(h)$ ranging from $-50\ \mathrm{mV}$ to $+50\ \mathrm{mV}$. As above, 41 design variables denoted $(\alpha_1, \alpha_2, \cdots, \alpha_{41})$ parameterize the coating at evenly spaced points throughout the depth of the coating. The simulated time to failure for a given set of design variables is denoted $t_f(\alpha_1, \alpha_2, \cdots, \alpha_{41})$. Thus the optimization problem may be stated as follows:

Maximize: $t_f(\alpha_1, \alpha_2, \cdots, \alpha_{41})$

Subject to: $50\ \mathrm{mV} \geq \alpha_1 \geq \alpha_2 \geq \cdots \geq \alpha_{41} \geq -50\ \mathrm{mV}$

In each iteration of the SA implementation used in this study, the parent coating is mutated to generate a candidate coating; candidates with higher time to failure are always adopted, while candidates with lower time to failure are adopted with finite probability based on the difference and a temperature parameter T. Several mutation operators have been examined in the literature, including uncorrelated random perturbation of some or all design variables [92,96], and more complex schemes involving coarser steps in the earlier iterations of the algorithm, and finer steps in the later iterations [93,97]. It has been reported in many cases that SA implementations with dynamically adjusted steps result in increased efficiency, by pairing rapid exploration of the search space during the initial iterations and efficient refinement to a local optimum during the later iterations [93,97]. Due to the high computational cost of each function evaluation in the present study, a similar dynamic stepping scheme is used, as described in detail below.

During each step, the perturbation to each design variable is the sum of two components. The first, $\Delta\, \alpha_{\text{bias}}$, is common to all of the design variables, while the second, Δ α_j, is selected individually for each. Each of these variables is drawn independently from a uniform distribution $\left[-\frac{\varepsilon}{2}, \frac{\varepsilon}{2}\right]$. This technique creates a balance between the need to allow the design variables to change independently, as captured in the different $\Delta\, \alpha_j$ chosen for each variable, and the need to impose a meaningful net displacement, captured by the shared Δ α_{bias}. In addition, the perturbations are multiplied by a Gaussian window of width σ, centered around a randomly chosen point, to generate steps that change local portions of the coating. For a given parent with composition parameter vector $(\alpha_1, \alpha_2, \cdots, \alpha_{41})$, this mutation algorithm is summarized below:

1. Select a random integer j_{mid} in the range 1 to 41.
2. Select a bias displacement $\Delta\, \alpha_{\text{bias}}$ from a uniform distribution in the range $\left[-\frac{\varepsilon}{2}, \frac{\varepsilon}{2}\right]$.
3. For each integer j in the range 1 to 41, select a random displacement $\Delta\alpha_j$ from a uniform distribution in the range $\left[-\frac{\varepsilon}{2}, \frac{\varepsilon}{2}\right]$.
4. Set the candidate $\alpha'_j = \alpha_j + \left(\Delta\, \alpha_{\text{bias}} + \Delta\, \alpha_j\right) \exp \frac{-(j-j_{\text{mid}})^2}{2\sigma^2}$
5. Sort the new α'_j to satisfy the monotonicity requirement
6. If any $\alpha'_j < -50$ mV V, set it to -50 mV; if any $\alpha'_j > +50$ mV, set it to $+50$ mV.

The parameters determining the size of the step are ε, giving the maximum magnitude change in any of the individual design variables, and σ, giving the width of the Gaussian window. Both of these parameters are decreased exponentially by a factors τ_ε and τ_σ, respectively, so that after N iterations, $\varepsilon = \varepsilon_0 \tau_\varepsilon^N$ and $\sigma = \sigma_0 \tau_\sigma^N$. All of these parameters were selected heuristically to balance exploration of the search space, speed of convergence, and reproducibility; a full list of the selected values can be found in Table 2.

Once a candidate coating is generated, a simulation is run to calculate the time to failure. The probability that the candidate coating is adopted is given by the Metropolis criterion:

$$\exp\left(\frac{t_{\text{candidate}} - t_{\text{parent}}}{T}\right) > \mu \tag{17}$$

where μ is a random variable chosen uniformly from the interval $[0,1)$, and T is the temperature parameter during that iteration. As in the case of the stepping parameters, T is decreased exponentially each iteration, so that *after* N iterations, $T = T_0 \tau_T^N$. The initial temperature was selected using a criterion proposed by Medina [98], that 20-40% of steps from randomized starting points to higher energy solutions would be accepted. This was accomplished by taking single steps from 50 different random coatings, calculating $t_{\text{candidate}} - t_{\text{parent}}$ for all cases in which $t_{\text{parent}} > t_{\text{candidate}}$, and then selecting T_0 such between 20-40% of these steps would be accepted. The values of T_0 and τ_T used in this study are included in Table 3.2.

Table 3.2 Annealing parameters for SA optimization

ε_0	20 mV
τ_ε	0.99
σ_0	40
τ_σ	0.99
T_0	10^4 s
τ_T	0.99

If the candidate is adopted, it replaces the parent and is used to seed the next SA iteration. The SA algorithm is run for a total of 400 iterations. The best coating, and highest time to failure, are recorded throughout the procedure, and returned as the optimized solution.

3.3.2. Simulated Annealing results

The SA algorithm described above was first run using the monolithic pure Zn coating, with $\alpha(h) = 0\ \mathrm{mV}$ thoughout, as a seed. The full range of candidate coatings tested during the optimization run is shown in Figure 3.9 (a). In the early iterations, during which the temperature and step size are high, the algorithm quickly searches a wide range of coatings. It does, however, display a strong preference for more strongly graded structures, with the composition spreading out over the full permitted range within a couple iterations and only rarely deviating from that pattern. In the later iterations, with a lower temperature and step size, the coating converges onto a quasi-bilayer structure, approximately described by a 2 μm noble layer adjacent to the substrate, a 13 μm active layer on the exterior, and a 5 μm transition zone between the two with a fairly smooth compositional gradient.

The calculated time to failure for this optimized coating is 1956 hours, or 81.5 days. This represents an improvement of 112% over the 38.5 days calculated for the monolithic coating used as a seed for the SA algorithm, and even an additional 15% improvement over the 71.0 days calculated for the linearly graded coating. Thus the SA optimized coating is a clear improvement over any of the naïve coating structures tested, indicating the potential of optimization techniques to discover coating structures superior to those that are likely to be tested by an empirical search.

To examine the robustness of the SA optimization, two additional optimization runs were performed seeded by monolithic coatings of the most active ($\alpha = -50\ \mathrm{mV}$) and most noble ($\alpha = +50\ \mathrm{mV}$) compositions. The initial and optimized coatings from all three SA runs are shown in Figure 3.9 (b). Although the three optimized coatings are not identical, they all share the same quasi-bilayer structure, with the sizes of the various regions varying by under 1 μm between runs. This suggests that these coating structures do in fact represent the neighborhood of an optimum solution, which the SA optimization procedure is able to robustly identify.

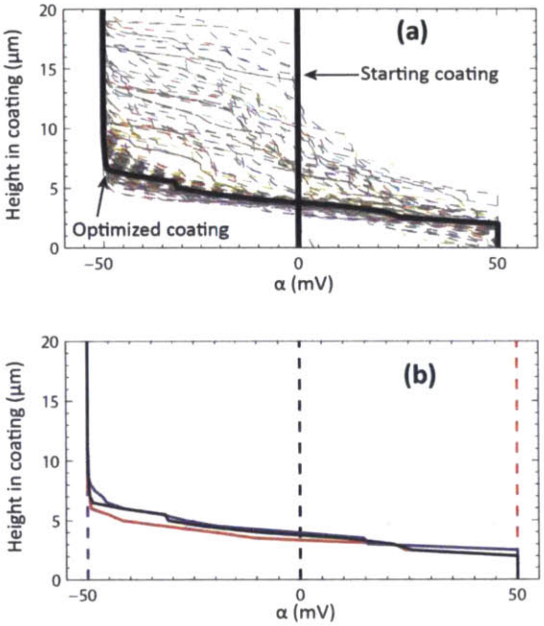

Figure 3.9 (a) All 400 coatings tested over the course of a representative SA run. Starting and final coatings are shown as solid lines. (b) Starting coatings (dashed lines) and optimized coatings (solid lines) for three separate SA runs.

The calculated time to failure of the candidate coatings over the first 200 SA iterations for all three optimization runs in Figure 3.10. The second 200 iterations are not shown, as any subsequent changes in the time to failure were negligible. In all cases, the time to failure increases very rapidly over the first 100 iterations, then continues to improve much more slowly as the coating structure is refined. As would be expected from the structural similarity between the highest performing coating identified in each run, the optimal time to failure found by the SA algorithm was quite similar in each case, differing by less than 1%. The path of coatings tested in a representative SA run is also shown Figure 3.8 overlaid on the results of the Monte-Carlo analysis. The SA optimized coatings lies well outside the convex hull of the Monte-Carlo results, showing that the SA algorithm successfully found solutions that improve upon any that might reasonably be discovered via a limited random search.

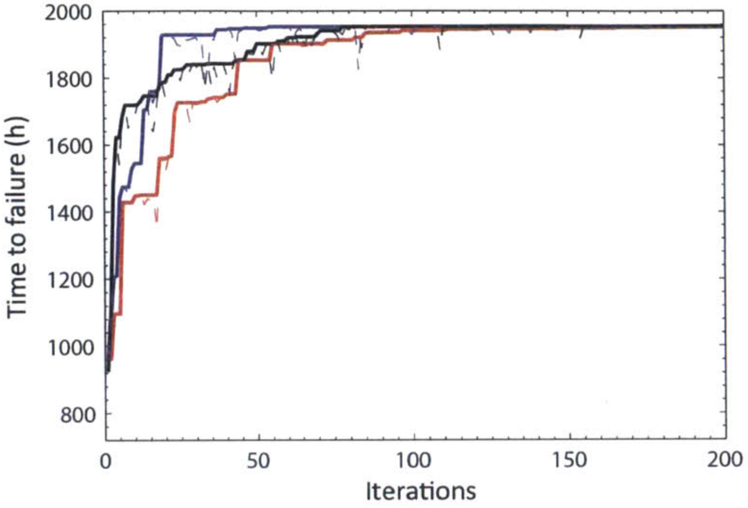

Figure 3.10 Improvement in objective function (time to failure) as a function of SA iteration number, for the first 200 iterations of each optimization run. No significant change was observed for higher iteration numbers. Solid lines show best coating discovered. while dashed lines show tested candidates.

As the accuracy of the model is on the order of 2%, it is not possible to confidently select the best coating from among the various coatings in the neighborhood of the optimal structure based on the time to failure results. Nonetheless, the results in Figure 3.10 show that the SA optimization procedure is able to reliably find "good" solutions, i.e. optimal to within the error rate of the model, after 200 iterations, each of which requires a single function evaluation. This represents a quite efficient search of the 41-dimensional design space; in contrast, standard gradient-based optimization algorithms would require 41 extra function evaluations per iteration to calculate the gradient at each point.

Examination of the optimized coating reveals several interesting features which account for the improvement in performance relative to the smoothly graded coating, the most protective of the three coating structures tested in the first part of this study. The linearly graded coating improved upon monolithic coating structures by allowing the outer layers to corrode sacrificially, decreasing the rate of substrate exposure and the available surface area for oxygen reduction. The optimized coating improves upon this strategy via its quasi-bilayer structure, in which the barrier layer is of more uniformly noble composition and the sacrificial layer is of more uniformly active composition, so that each performs its role more effectively.

In addition, the active sacrificial layer has been widened at the expense of the noble barrier layer, resulting in a downward shift of the average composition parameter, to -32 mV, relative to a mean of 0 mV for the smoothly graded coating. Since the sacrificial layer is consumed over time, while the barrier layer is largely protected, increasing the thickness of the sacrificial layer increases the time interval during which additional substrate exposure is inhibited. However, the SA results show consistently better performance for barrier layers of no less than 2 μm, as thinner barriers are unable to fully protect the substrate despite the cathodic protection of the outer layers.

It is important to note, however, that the barrier layer proposed by this analysis is still sacrificial relative to the substrate itself. Barrier layers that are noble relative to the substrate, such as Ni, are outside the scope of the model, since they present the possibility of localized corrosion of exposed substrate in preference to the barrier layer, resulting in undercutting of the coating and instability in the model results. Such localized corrosion and undercutting have been observed experimentally, and often significantly compromise the ability of noble coatings to protect substrates from corrosion [3,26]. However, the present study suggests that many of the benefits of composite coating structures can be realized without the use of coating materials noble to the substrate, and may only require a relatively small range of variation of composition within the coating. Therefore, it appears that composite coatings comprised of purely sacrificial materials may have the potential to significantly improve coating performance without the associated risk of exacerbating localized corrosion.

The results of this optimization suggest an additional design principle for compositionally modulated coatings for corrosion protection, namely that improved performance may be obtained by tailoring the thickness of layers of varying compositions to reflect their individual roles in providing protection. In particular, increasing the thickness of sacrificial layers with high corrosion rates in the coupled system, at the expense of barrier layers with low corrosion rates, may increase protection time without increasing overall coating thickness. This is in contrast to the approach taken by most corrosion studies of multilayer or graded coatings in the literature, in which all layers are taken to be equal thickness [3,23,26,31].

3.4 Conclusion

This chapter presents a computational modeling approach for simulation of time-dependent galvanic corrosion of compositionally graded coatings, as well as computational optimization of such coatings. The model simulates the progress of corrosion through a coupled finite element electrochemical model, using calculated rates of metal dissolution to update coating geometry over time. Optimization of coating structure to maximize the desired protective properties is accomplished through the simulated annealing technique. This approach is applied to a hypothetical zinc-alloy coating on an iron substrate with a radially symmetric defect, in an aerated NaCl electrolyte.

The results of this approach to modeling and optimization, applied to this test system, exhibit several interesting features. A wide range of graded coating structures, with outer layers more active than inner ones, significantly improve the duration of cathodic protection, by up to a factor of ~2. This improvement can be attributed primarily to the inhibition of substrate exposure, which results when the outer layers cathodically protect the inner layers as well as the substrate itself. The improved performance of these graded structures is largely contingent on the use of coating materials that exhibit sluggish oxygen reduction rates relative to the substrate, so that the inhibition of substrate exposure can result in reduction of the overall corrosion rate of the system.

Optimization of coating structure using simulated annealing is shown to be both efficient and robust for the test system. The optimized coating structure consists of a quasi-bilayer structure, with a thin inner layer of the most noble composition, and a thicker outer layer of the most active composition. This improves protection time of the substrate relative to a naïve linear gradient or bilayer, as thickening the sacrificial layer allows the beneficial compositional gradient to be maintained for a longer period of time.

Overall, based on the results from the test system studied here, this modeling approach predicts significant potential for improvement in corrosion protection by development of compositionally graded coating structures, and elucidates several useful design principles that contribute to the performance of a composite coating. Furthermore, the simulated annealing technique is a powerful tool for optimization of coating structures, able to efficiently discover non-obvious designs that significantly improve upon any of the simpler or randomized designs tested. Thus, although it is very difficult to use computational methods to generate exact quantitative predictions, especially over long periods of time, this computational modeling and optimization technique has great potential to inform and guide the development of compositionally graded coatings for corrosion protection.

4 Validation of galvanic corrosion model on vapor-deposited zinc and aluminum coatings

4.1 Introduction

While computational models of galvanic corrosion, such as was presented in chapter 3, have been well validated for short timescales [47,48], there has been very little work directly comparing the outputs of time-dependent computational models with measurements on the changes in coating structure. As calculated distributions of potential allow prediction of instantaneous metal dissolution rates, time-dependent simulations of galvanic corrosion can be generated through a variety of moving boundary techniques [5,45,46,49,51,52,70,71,99], which account for the changes in the geometry of the system over time. Brown and Barnard used a time-dependent model to simulate corrosion of a Zn - 5 wt.% Al coatings coupled to a steel substrate [45,46], showing that refinement of coating microstructure decreases zinc loss over time, in agreement with experimentally observed trends, but not directly comparable to the experiments in a quantitative sense [54]. Deshpande [5,49] used a time-dependent model with moving boundaries to simulate galvanic corrosion of coplanar magnesium alloy AE44-steel and AE44-aluminum alloy couples in neutral NaCl solution. He compared the model results with current density measurements taken using the scanning vibrating electrode technique, and surface profiles taken following a three day immersion test. Good agreement was reported between predicted and measured current densities, and surface profiles were found to match well for the AE44-mild steel, but the model underestimated the corrosion rate in the AE44-aluminum alloy couple. In our recent work, we proposed that time-dependent galvanic corrosion modeling could be combined with optimization algorithms, to design preferred coating architectures with, e.g., functional gradients in corrosion potential built into them [99]. That work was however only computational, and experiments on multilayered or functionally graded coated in general have not been compared with any predictive simulation.

Despite the widespread deployment and significant commercial value of galvanic coatings, in particular zinc-based coatings, for protection of steel, to our knowledge there have not been any attempts to directly compare experimental measurements of corrosion of galvanic coatings to time-dependent models. Such validation is critically important to confidently use computational modeling as a tool for prediction of coating performance and design of coatings with improved properties. Thus, in the present study, the accuracy of time-dependent simulations of the galvanic corrosion of zinc and aluminum coatings over steel substrates is investigated, through direct comparison of model outputs and experimental measurements.

4.2 Experimental procedures

4.2.1 Synthesis of coatings

Coatings were deposited on mild steel substrates using electron beam deposition. Steel specimens 20 x 10 x 1 mm in size were ground sequentially with 240, 600, 1200, 2400, and 4000 grit emery papers. Subsequently the specimens were polished with 6, 3 and 1 micron diamond suspensions to achieve a mirror finish, ultrasonicated in ethanol for 2 minutes and etched for 5-10 seconds with mild hydrochloric acid. The specimens were again cleaned with ethanol and dried before being plasma cleaned for a period of 3 minutes. The plasma was generated in an oxygen atmosphere at a pressure of 0.5 torr and 200 W power. The specimens used for corrosion tests were masked with a thin strip of steel, 20 x 1.5 x 0.5 mm, held in tight contact with the steel substrate by clamps, and placed across the sample surface so as to divide it into two equal halves. The specimens were loaded into an electron beam deposition chamber (Varian 904/Sloan Pak-8). The chamber was initially purged with nitrogen and then pumped down with a roughing pump followed by a diffusion pump to a vacuum of approximately 10^{-6} torr. Deposition was carried out at a voltage of 8 kV and a current of 0.25 A and 0.02 A for aluminum and zinc, respectively. The deposition rate was maintained at 3-4 Å/s for aluminum and 2-3 Å/s for zinc. Following deposition, the specimens were allowed to cool inside the chamber under vacuum conditions for approximately 45 minutes. Subsequently they were removed from the chamber and the masks were unclamped. The resulting geometry was a coating over the sample surface except for an exposed strip down the center of the specimen, as shown in Figure 4.1 (a). In order to improve adhesion, the zinc coatings were heat treated at

300 °C for 15 minutes in an argon atmosphere. The coated steel specimens were then characterized through profilometry, scanning electron microscopy and corrosion tests.

4.2.2 Polarization Curves

Polarization curves were measured for a bare steel substrate as well as zinc and aluminum deposited on glass so as to remove any possible contribution from the substrate. The samples were masked to expose a 1 x 1 cm area, and immersed in 10 mM H_2SO_4 electrolyte solution in a Gamry multiport corrosion cell. The solution was deaerated by purging with nitrogen gas for 2 hours.

The polarization curves were captured at a scan rate of 0.5 mV/s in the anodic direction, using a PARSTAT 2273 potentiostat (Princeton Applied Research). The potential was measured using a silver/silver chloride reference electrode (Gamry), coupled to the electrolyte through a fritted capillary tube with its tip placed adjacent to the sample. For the aluminum and zinc samples, the potential was swept from -200 mV to +200 mV relative to the initial open circuit potential. For the steel sample, the potential was swept from -400 mV to +250 mV relative to the open circuit potential. Measurements for the steel substrate and aluminum on glass were taken following 30 minutes of immersion in the electrolyte. However in the case of the zinc coating, due to its high rate of dissolution, measurements were taken immediately following immersion in acid.

4.2.3 Corrosion Testing

Corrosion tests were performed on steel with zinc and aluminum coatings, deposited on the samples partially masked as described above, to expose a strip of substrate of approximate width 1.5 mm after deposition, shown schematically in Figure 4.1 (a). For corrosion testing the samples were masked to expose a 1 x 1 cm area, bisected by the strip of exposed substrate. The coated samples were immersed in deaerated 10 mM H_2SO_4, and the open circuit potential measured throughout the period of immersion. The tests were interrupted and the samples removed periodically for profilometry measurements using a KLA Tencor P-16 surface profilometer. Immediately after removing the coated samples from the electrolyte, they were immersed in ethanol to wash away the electrolyte and dried with a gentle draft of air. They were scanned with the profilometer stylus at a rate of 50 μm/s under a load of 20 mg. The range and resolution were set at 131 μm and 0.0781 °A respectively. For each sample, scans were taken at three different locations to check for repeatability of data. The data were slope-corrected for better visualization and quantitative comparisons.

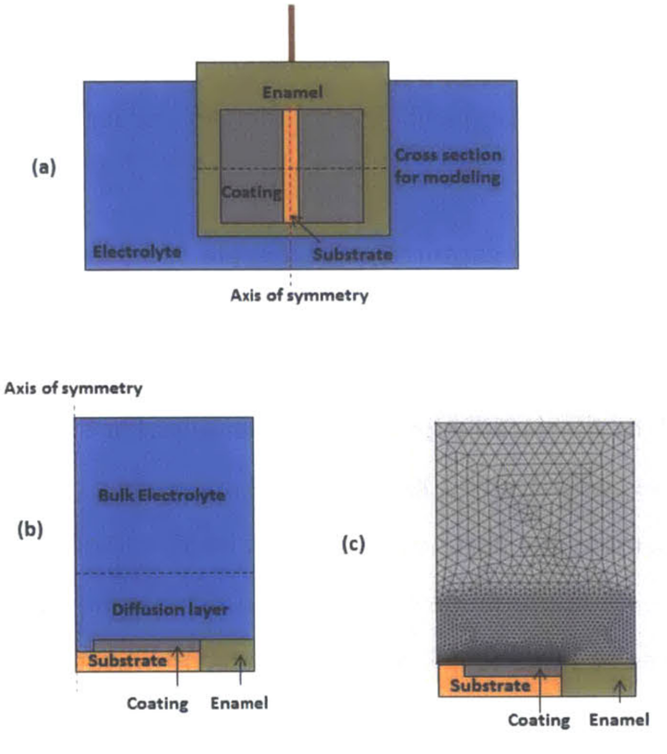

Figure 4.1: (a) Setup for corrosion test (front view). (b) Schematic of modeled electrolyte domain. (c) Finite element mesh over electrolyte domain.

4.3 Computational model of galvanic corrosion

The modeling techniques used in this chapter are similar to those described in Chapter 3, with a number of modifications. The most significant is the inclusion of mass transport modeling, to calculate the distribution of H^+ ions and dissolved metals, which is important in this system as hydrogen evolution is generally under mixed activation-diffusion control. The model is described in greater detail in the following sections.

4.3.1 Model system

Corrosion simulations were performed on a geometry modeling a 1 cm wide strip of coated steel, with a half centimeter insulating surface on either side, i.e. a geometry designed to match that of the experimental system as shown in Figure 4.1 (a). The coatings were taken to be either pure zinc or pure aluminum, and the initial coating geometry for each simulation was taken to match the profilometry measurements of the associated coating as closely as possible, including the central masked region.

The electrolyte was modeled as a 1 cm thick layer of deaerated 10 mM H_2SO_4 electrolyte solution. Due to symmetry, modeling was performed on the right half of the electrolyte domain only, represented schematically in Figure 4.1 (b). The geometry was discretized into 10,000 cells in the *x* direction, spanning the range from the center of the strip to the coating/insulator interface, so that each cell spanned a lateral distance of 0.5 µm. At a given time t, the height of the system at each of the cells was stored in a height vector $h(x, t)$, which was used to determine which metal was exposed to the electrolyte; $h > 0$ corresponds to coating being present over the substrate, while $h < 0$ corresponds to a bare steel surface. Because variations in coating thickness were very small relative to the lateral dimensions of the system, for modeling purposes the surface was considered to be flat, and so the electrolyte domain was approximated as a rectangle.

Experimental measurements of concentration profiles of dissolved species in corroding systems show that the concentrations of all species tend to rapidly approach bulk concentrations outside of a diffusion layer adjacent to the surface [100–102]. Therefore, a diffusion layer of fixed thickness δ was introduced into the model in which gradients in concentrations were permitted to vary. The concentration of all dissolved species was maintained at bulk values outside of the diffusion layer by setting a boundary condition fixing the concentration of all species at the diffusion layer boundary. The electrolyte was discretized using a triangular finite element mesh, with finer elements near the electrode surface where the potential and concentration gradients would be expected to be largest, and coarser elements in the bulk electrolyte. A representative mesh of the electrolyte domain is shown in Figure 4.1 (c).

4.3.2 Governing equations

For a given coating configuration, the finite element method was used to solve for the concentration of the following dissolved species: H^+, HSO_4^-, Fe^{2+}, Zn^{2+}, Al^{3+}, as well as the electrolyte potential ϕ. Several other possible species were considered, including OH^-, SO_4^{2-}, and metal ion-hydroxide complexes such as $ZnOH^-$, $Zn[OH]_2$, $AlOH^{2-}$, $Al[OH]_2^-$, $Al[OH]_3$, and $Al[OH]_4^+$, but in all cases these species would be expected to be present in negligible concentrations based on published stability constants [103], and were therefore not included in the model. The flux of dissolved species i in the electrolyte due to diffusion and electromigration is described by the Nernst-Planck equation:

$$N_i = -D_i \nabla \mathrm{c_i} - \frac{D_i z_i F}{RT} c_i \nabla \phi \tag{1}$$

where c_i is the concentration of species i, D_i is the diffusion coefficient, z_i is the valence, F is the Faraday constant, R is the ideal gas constant, and T is the temperature. A list of the diffusion coefficients and other constants used in the model is included in Table 4.1.

Table 4.1 Table of constants used in the model.

Constant	Description	Value
$c_{H^+}^*$	Bulk hydrogen ion concentration	10 mol/m^3
$c_{Fe^{2+}}^*$	Bulk iron ion concentration	0 mol/m^3
$c_{Zn^{2+}}^*$	Bulk zinc ion concentration	0 mol/m^3
$c_{Al^{3+}}^*$	Bulk aluminum ion concentration	0 mol/m^3
$c_{HSO_4^-}^*$	Bulk hydrogen sulfate concentration	10 mol/m^3
D_{H^+}	Hydrogen ion diffusion coefficient	9.3×10^{-9} m^2/s [28]
$D_{Fe^{2+}}$	Iron ion diffusion coefficient	10^{-9} m^2/s [28]
$D_{Zn^{2+}}$	Zinc ion diffusion coefficient	0.7×10^{-9} m^2/s [28]
$D_{Al^{3+}}$	Aluminum ion diffusion coefficient	0.54×10^{-9} m^2/s [28]
$D_{HSO_4^-}$	Hydrogen sulfate diffusion coefficient	1.33×10^{-9} m^2/s [28]

Since no association/dissociation reactions between dissolved species were expected, the steady state solution to the Nernst-Planck equation was then given by:

$$\frac{\partial c_i}{\partial t} = -\nabla \cdot N_i = 0 \tag{4.2}$$

The electrolyte was also subject to the electroneutrality condition:

$$\sum z_i c_i = 0 \tag{4.3}$$

which relates the concentrations of the dissolved ions. The concentration of the HSO_4^- was then calculated indirectly from the concentrations of the other ions.

4.3.3 Boundary conditions

At all insulating surfaces (see Figure 4.1 (b)) the flux of all species was set to zero:

$$-N_i \cdot \hat{n} = 0 \tag{4.4}$$

where $\hat{n}$ is the inward unit vector normal to the surface.

At the diffusion layer boundary the concentrations of all species were set to their bulk concentrations:

$$c_i = c_i^* \tag{4.5}$$

The electrochemical reactions permitted at the electrode surfaces were hydrogen evolution $2\mathrm{H}^+ + 2\mathrm{e}^- \rightarrow \mathrm{H}_2$ and metal oxidation ($\mathrm{Zn} \rightarrow \mathrm{Zn}^{2+} + 2\mathrm{e}^-$, $\mathrm{Al} \rightarrow \mathrm{Al}^{3+} + 3\mathrm{e}^-$, $\mathrm{Fe} \rightarrow \mathrm{Fe}^{2+} + 2\mathrm{e}^-$), depending on which metal was exposed at the surface. It was assumed that the resistivity of the metal is negligible, relative to that of the electrolyte, so the electrical potential of the metal could be set to 0 everywhere. So, at any point along the metal/electrolyte interface, the local electrode potential was given by:

$$E = -\phi \tag{4.6}$$

The rate of the metal oxidation was taken to have an exponential dependence on potential:

$$i_a = k_{0,a} n F \exp \frac{E - E_a^0}{\beta_a} \tag{4.7}$$

where i_a is the anodic current density, E_a^0 is the standard electrode potential and $k_{0,a}$ the interfacial rate constant for metal oxidation, n is the valence, F is the Faraday constant, and β_a is the anodic Tafel parameter.

The rate of hydrogen evolution was also taken to have an exponential potential dependence, with first order dependence on the surface H^+ concentration:

$$i_c = k_{0,c} c_{\mathrm{H}^+}^s F \exp \frac{E - E_c^0}{\beta_c} \tag{4.8}$$

where i_c is the cathodic current density, $c_{\mathrm{H}^+}^s$ is the hydrogen ion concentration adjacent to the electrode surface, E_c^0 is the standard electrode potential and $k_{0,c}$ the interfacial rate constant for hydrogen reduction, and β_c is the cathodic Tafel slope. The kinetic Tafel parameters for hydrogen evolution were measured independently for each metal surface.

The above equations for anodic and cathodic current densities determined the associated flux of metal ions into the solution, or hydrogen ions out of solution:

$$-N_i \cdot \hat{n} = \frac{i_a}{n_i F} \tag{4.9}$$

$$-N_{\mathrm{H}^+} \cdot \hat{n} = \frac{i_c}{F} \tag{4.10}$$

4.3.4 Time-dependent modeling

In order to simulate the evolution of the system over time as it undergoes galvanic corrosion, at the start of each time step, the height function was used to determine the regions of each metal exposed to the electrolyte. A finite element (FE) solver, implemented in the commercial code COMSOL, was then run to solve the Nernst-Planck equations for the given geometry, and calculate the distribution of potential and dissolved ions throughout the electrolyte. Using the metal dissolution current i_a calculated from the Tafel equation, the rate of change in height was:

$$\frac{\partial h}{\partial t} = -i_a \left(\frac{A_{w,i}}{z_i F \rho_i} \right) \tag{4.11}$$

where ρ_i is the density, and $A_{w,i}$ is the atomic weight. The new coating geometry was then returned to the FE solver to initiate the next time step.

In order to control the error introduced by the time-integration, an adaptive step size algorithm was applied. Following each time step, the estimated electrode potential at the beginning $E_0(x)$ and end $E_0(x)$ were compared. Tolerances δ_0 and δ_1 were determined such that

$$\delta_0 \leq \max\{|E_0(x) - E_1(x)|\} \leq \delta_1 \tag{4.12}$$

The time step was then adjusted so that this condition was satisfied during each time step. The tolerances were decreased until good convergence in model output was observed, which was found for values of $\delta_0 = 1\ \mathrm{mV}$ and $\delta_1 = 3\ \mathrm{mV}$.

4.3.5 Kinetic parameters

The kinetic parameters for the rates of each electrochemical reaction were inferred from polarization curves taken for each metal surface immersed in 10 mM H_2SO_4. Figure 4.2 shows polarization curves taken for each surface. Due to the lack of a supporting electrolyte, significant deviations from Tafel behavior are expected due to solution resistance and the limited rate of diffusion of H^+ to the electrode surface. Thus, in order to extract Tafel parameters from the polarization curves, a simple 1-D model of the electrolyte was employed. If the electrode potential at the electrode surface is taken to be E_s, the expected anodic current and cathodic current densities, in the absence of concentration effects, are:

$$i_a = k_{0,a} n F \exp\left(\frac{E_s - E_a^0}{\beta_a}\right) \tag{4.13}$$

$$i_{c,K} = k_{0,c} c_{\mathrm{H}^+}^{*} F \exp\left(\frac{E_s - E_c^0}{\beta_c}\right) \tag{4.14}$$

where $i_{c,K}$ is the kinetic hydrogen evolution current density.

The hydrogen evolution reaction is assumed to have first order concentration dependence, so that the adjusted cathodic current density is given by:

$$i_c = \frac{c_{\mathrm{H}^+}^{s}}{c_{\mathrm{H}^+}^{*}} i_{c,K} \tag{4.15}$$

where $c^s_{H^+}$ is the hydrogen ion concentration adjacent to the electrode surface. Assuming a linear concentration gradient in the diffusion layer, the ionic current associated with hydrogen ion diffusion is given by:

$$i_c = \frac{FD_{H^+}}{\delta}(c^*_{H^+} - c^s_{H^+}) \tag{4.16}$$

with limiting current density:

$$i_{c,L} = \frac{FD_{H^+}}{\delta}c^*_{H^+} \tag{4.17}$$

Under steady state conditions, the ionic and interfacial cathodic current densities are equal:

$$i_c = \frac{c^s_{\mathrm{H}^+}}{c^*_{\mathrm{H}^+}} i_{c,K} = i_{c,L}\left(1 - \frac{c^s_{\mathrm{H}^+}}{c^*_{\mathrm{H}^+}}\right) \tag{4.18}$$

and the adjusted hydrogen evolution current is then:

$$i_c = \frac{i_{c,K}\, i_{c,L}}{i_{c,K} + i_{c,L}} \tag{4.19}$$

In addition to the mass transfer limitations, the potential E_m measured at the reference electrode is offset from the electrode surface potential due to solution resistance, proportional to current density:

$$E_m = E_s + (i_a - i_c)R_s \tag{4.20}$$

This model was applied to the polarization curve for steel, and a least-squares curve fitting algorithm was applied to calculate the anodic and cathodic Tafel parameters, solution resistance, and limiting cathodic current. The best fit for the limiting cathodic current was $80.4\ \mathrm{A/cm^2}$, corresponding to the maximum rate of diffusion through a layer of thickness 0.233 mm. This is on the lower end of most estimates of diffusion layer thickness, most commonly taken to be 0.2-0.5 mm [100–102,104]. This discrepancy may reflect increased stirring of the solution due to vigorous hydrogen evolution on the steel surface at cathodic potentials.

However, since hydrogen bubbling from the steel surface was observed during corrosion tests, we chose to use the smaller value to match experimental conditions as closely as possible. The value of δ calculated from the steel surface was then fixed, and used to fit the polarization curves of the aluminum and zinc surfaces. The best fit Tafel parameters for each surface are listed in Table 4.2. The expected polarization curves based on the fit values are also plotted in Figure 4.2.

Table 4.2 Kinetic parameters based on fits to polarization curves.

Material	Parameter	Description	Value
Steel	$k_{0,a}$	Interfacial rate constant for oxidation of iron	1.85×10^{-7}mol/(m^{2}s)
Steel	$k_{0,c}$	Interfacial rate constant for reduction of hydrogen (steel surface)	3.24×10^{-9}m/s
Steel	β_a	Anodic Tafel parameter for oxidation of iron	0.058 V vs SHE
Steel	β_c	Cathodic Tafel parameter for reduction of hydrogen (steel surface)	-0.152 V vs SHE
Steel	E_a^0	Equilibrium potential for oxidation of iron	-0.45 V vs SHE
Zinc	$k_{0,a}$	Interfacial rate constant for oxidation of zinc	1.51×10^{-6}mol/(m^{2}s)
Zinc	$k_{0,c}$	Interfacial rate constant for reduction of hydrogen (zinc surface)	9.10×10^{-18}m/s
Zinc	β_a	Anodic Tafel parameter for oxidation of zinc	0.041 V vs SHE
Zinc	β_c	Cathodic Tafel parameter for reduction of hydrogen (zinc surface)	-0.079 V vs SHE
Zinc	E_a^0	Equilibrium potential for oxidation of zinc	-0.76 V vs SHE
Aluminum	$k_{0,a}$	Interfacial rate constant for oxidation of aluminum	6.42×10^{-8}mol/(m^{2}s)
Aluminum	$k_{0,c}$	Interfacial rate constant for reduction of hydrogen (aluminum surface)	4.83×10^{-8}m/s
Aluminum	β_a	Anodic Tafel parameter for oxidation of aluminum	0.890 V vs SHE
Aluminum	β_c	Cathodic Tafel parameter for reduction of hydrogen (aluminum surface)	-0.347 V vs SHE
Aluminum	E_a^0	Equilibrium potential for oxidation of aluminum	-1.6 V vs SHE
All	E_c^0	Equilibrium potential for reduction of hydrogen	0.0 V vs SHE

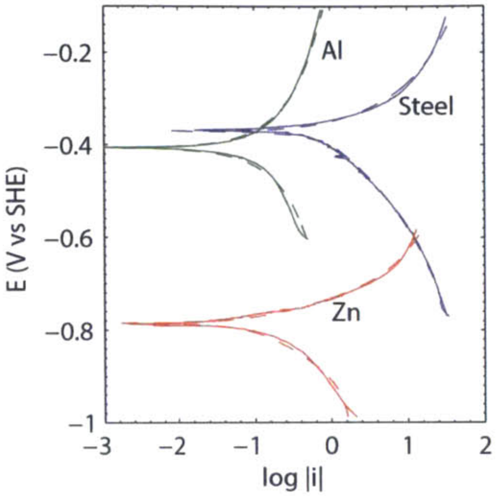

Figure 4.2 Polarization curves for Al on glass, Zn on glass, and steel substrate, with best fits based on calculated Tafel parameters.

4.4 Corrosion simulations

The behavior of the simulated zinc coating on steel is shown in Figure 4.3. At the start of the simulated corrosion test, the calculated open circuit potential, shown in Figure 4.3 (e), was approximately -0.7 V vs SHE, close to the corrosion potential of zinc. This suggests that the zinc coating was able to provide effective cathodic protection of the steel substrate. The cathodic protection was maintained for approximately 80 minutes, at which point the entire zinc coating was consumed, and the potential rose sharply to match that of uncoated steel.

The steady state coating thickness, electrode potential, current, and dissolved ion concentrations after 20 minutes for the simulated zinc/steel system are shown in Figure 4.3 (a)-(d). The time was selected to fall well within the period of cathodic protection, so as to illustrate the behavior of the simulated zinc coating as it provides sacrificial protection. Due to the cathodic protection supplied by the zinc, the steel surface showed a strongly net cathodic current, and the concentration of dissolved Fe^{2+} in the electrolyte is very low. The zinc, however, dissolved rapidly, with preferential dissolution adjacent to the zinc/steel interface, as can be seen in the selective thinning of the coating edge in Figure 4.3 (a), and the non-uniform distribution of anodic current in Figure 4.3 (c).

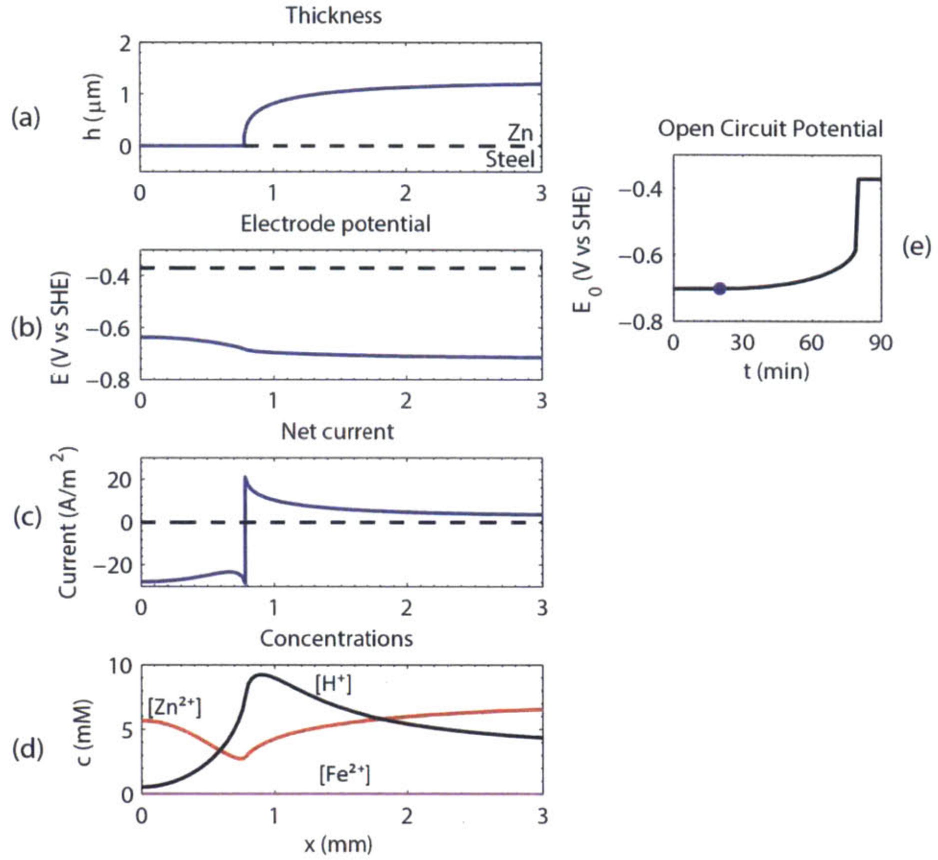

Figure 4.3: Representative steady state solution for the simulated zinc coating on steel, after 20 minutes immersion. The left column shows the calculated (a) coating thickness, (b) electrode potential, (c) net current, and (d) concentrations of dissolved species along the metal/electrolyte interface. (e) The corrosion potential throughout the simulation. The marked point shows the corrosion potential corresponding to the steady state solutions on the left.

The behavior of the simulated corrosion test on the aluminum coated steel, shown in Figure 4.4, was qualitatively quite different than that of the zinc coated steel. The aluminum coating did not dissolve quickly enough to provide effective cathodic protection, which can be seen in the higher corrosion potential, and increased concentration of Fe^{2+} ions in the electrolyte. Due to the low potential dependence of the aluminum dissolution, the dissolution rate of the aluminum coating was quite uniform, and did not show preferential dissolution near the coating/substrate interface. The simulated coating corroded at roughly half of the rate of the substrate, resulting in significant dissolution of the exposed steel.

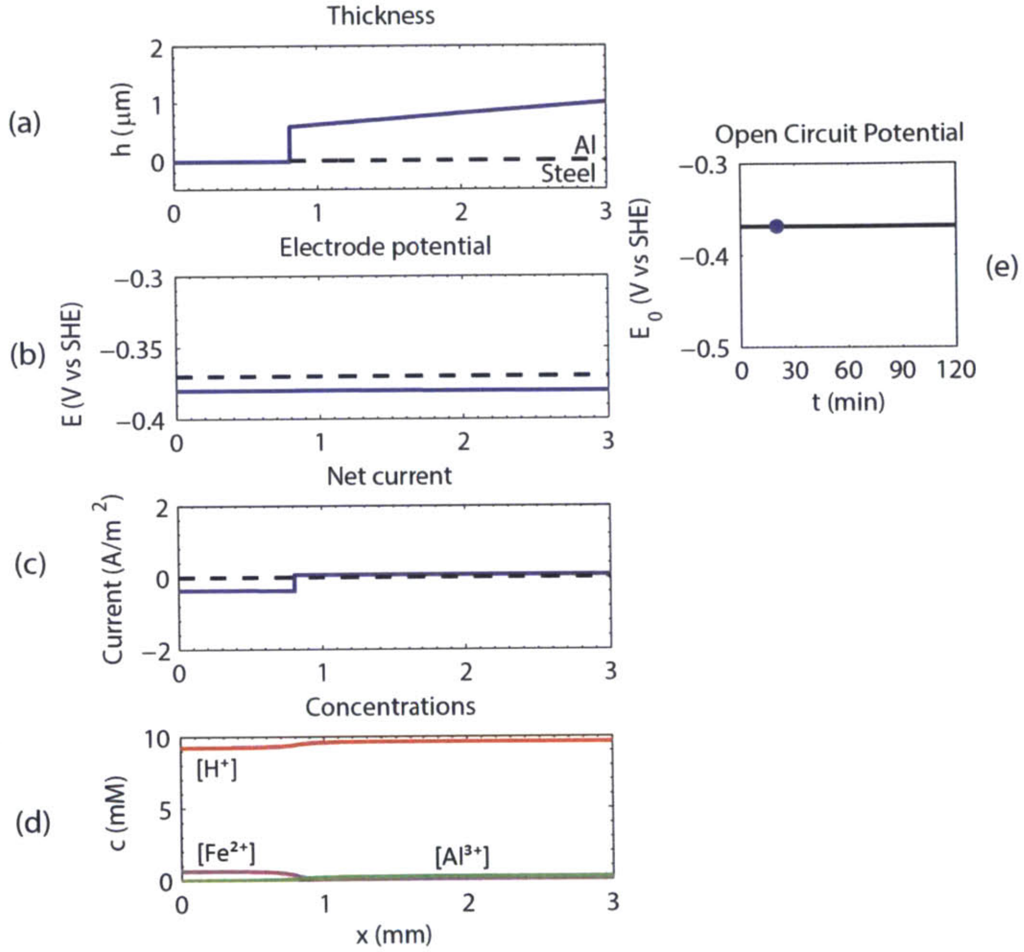

Figure 4.4 Representative steady state solution for the simulated aluminum coating on steel, after 20 minutes immersion. The left column shows the calculated (a) coating thickness, (b) electrode potential, (c) net current, and (d) concentrations of dissolved species along the metal/electrolyte interface. (e) The corrosion potential throughout the simulation. The marked point shows the corrosion potential corresponding to the steady state solutions on the left.

In both cases, the concentration profiles show some depletion of H^+ ions over the steel surface, due to efficient catalysis of the hydrogen evolution reaction by the steel. The depletion of H^+ is minimal for the aluminum coated steel but significant for the zinc coated steel, as the low corrosion potential of the zinc coating accelerates the reaction rate, with a minimum calculated concentration of 2.7 mM at the zinc/steel interface. This suggests that the hydrogen evolution reaction is under mixed diffusion/activation control in this case, and so consideration of mass transfer of H^+ in the electrolyte is necessary to accurately model this system.

Calculation of concentration profiles also permits the model to account for effects of variations in electrolyte composition on the corrosion process. A wide range of corrosion phenomena are critically dependent on electrolyte composition, such as the precipitation of corrosion products, onset of passivity, and changes in electrode kinetics due to surface modification. In the cases reported in this study, the calculated pH adjacent to the metal surface was found to fall in the range of 2.0 to 2.6. As published Pourbaix diagrams [105] show no passive regions for iron, zinc, or aluminum for electrode potential less than 0 V vs SHE and pH less than 4, active corrosion may be confidently assumed for all cases. Likewise the calculated concentration of dissolved species allow the prediction of regions of association reactions and corrosion product precipitation, based on published stability constants [103]. In the cases studied here the calculated concentrations are too low to cause association reactions to occur, and so effects such as corrosion product precipitation or pH buffering due to hydrolysis reactions may be neglected.

4.5 Comparison with experiments

The corrosion experiment on the zinc coating showed similar qualitative behavior to the model prediction, marked by an initial period of low open circuit potential during which the coating dissolved rapidly, with preferential thinning of the coating adjacent to the steel. Hydrogen gas was observed bubbling rapidly from the exposed steel. As in the case of the simulated coating, this period of cathodic protection was followed by a sharp rise in potential to approximately that of bare steel. The measured coating height profiles after 0, 10, 25, and 40 minutes, as well as those predicted by the model, are shown in Figure 4.5 (a). The measured and simulated open circuit potential over the course of the corrosion test is shown in Figure 4.5 (b), with the points marked corresponding to the times of the profilometry measurements.

The profilometry measurements at 0, 10, and 25 minutes agreed well with the model results. However, the profilometry measurement taken at 40 minutes showed different behavior than expected based on the model results. Rather than continuing the uniform active corrosion seen during the first 30 minutes, the remaining coating began to show localized corrosion and pitting. This coincided with the increase in the open circuit potential seen in Figure 4.5 (b), indicating a loss of effective cathodic protection. The switch from uniform to localized corrosion, and decrease in the corrosion rate, suggests that the remaining coating surface had become passive. The reason for the loss of reactivity of the remaining coating is unclear.

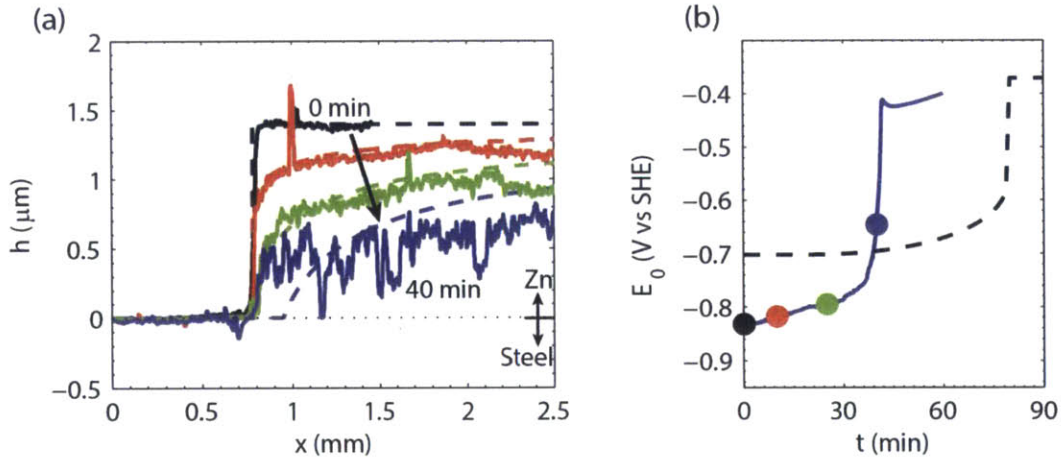

Figure 4.5 Comparison of (a) profilometry and (b) open circuit potential between model and experiments for pure zinc coating. Dashed lines show values predicted by the model.

The simulated corrosion potential took about 80 minutes to rise to the level of bare steel, while the experimentally measured corrosion potential took about 40, as shown in Figure 4.5 (b). The majority of the delay can be attributed to the loss in coating reactivity – if the average rate of zinc dissolution over the first 25 minutes had been maintained, complete coating dissolution would have occurred in approximately 68 minutes, in much closer agreement with model results. In addition, the experimentally measured open circuit potential was approximately 100 mV lower than that predicted by the model during the initial period of cathodic protection. This discrepancy, along with the slightly accelerated rate of coating dissolution compared to the simulation, suggests that the coating was initially somewhat more active than expected at the outset of the corrosion test.

The corrosion test on the aluminum coating exhibited significantly less dynamic behavior than that of the zinc coating, in accordance with the model prediction. The evolution of the height profiles and open circuit potential for the simulated and experimentally tested aluminum coatings are shown in Figure 4.6 (a) and (b). The open circuit potential decreased only by about 50 mV over the course of the corrosion test, in reasonable agreement with the prediction that it would stay almost constant. The relatively small difference here is most likely explained by the aluminum become increasingly active over time due to reduction of air-formed surface oxides. The steel showed significant corrosion damage, as would be expected due to the lack of cathodic protection. The aluminum was observed to corrode slightly faster than the steel, whereas the simulation predicted that the aluminum would corrode at approximately half the rate of the steel substrate. This mirrored the findings reported by Deshpande [5], in which the model underestimated the corrosion rate of the aluminum alloy/magnesium alloy by 30-50 percent, in that case attributed to the small galvanic mismatch between the two components. Since the corrosion potential of the aluminum and steel in this study were quite close (-0.41 V vs SHE for aluminum and -0.37 V vs SHE for steel), it is reasonable to expect some error in the calculated relative corrosion rates for the two metals.

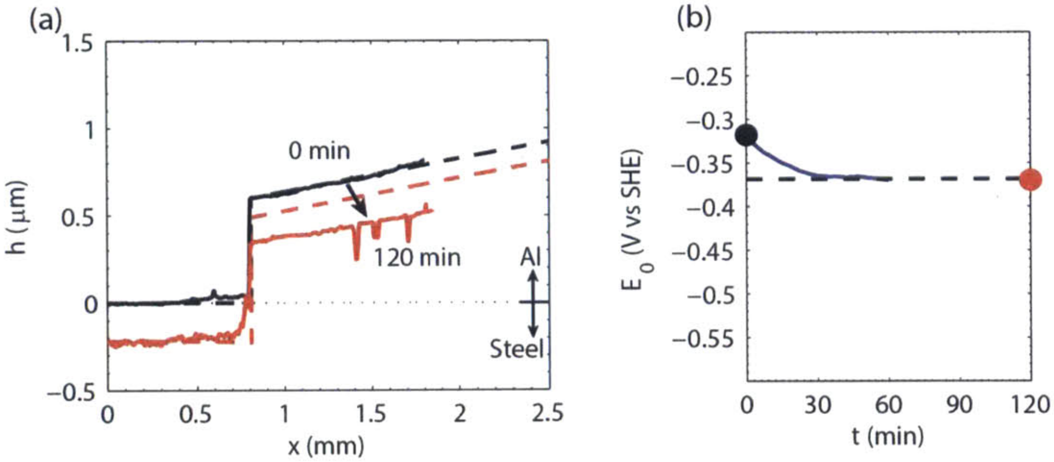

Figure 4.6 Comparison of (a) profilometry and (b) open circuit potential between model and experiments for pure aluminum coating. Dashed lines show values predicted by the model.

In spite of some small differences, the agreement between the model and the experiment shown in Figure 4.6 is quite reasonable for the aluminum coating. This, as well as the very good agreement seen earlier in the case of the Zn coating in Figure 4.5, are interpreted as an encouraging result for the simulation and evaluation of galvanic coatings, especially as a substitute for purely empirical approaches to the study of galvanic protection. In previous work [99] two of the authors have presented a methodology for design and optimization of compositionally graded corrosion coatings, in which the quality of a given coating structure is estimated based on finite element corrosion simulations. The fact that a single model presented in the current paper can capture the very different response of the two materials systems studied here, bodes well for the successful application of such computational methods to simulation and design of heterogeneous or composite corrosion coatings.

4.6 Conclusions

This chapter presents a direct comparison between time-dependent corrosion simulations and experimental measurements of zinc and aluminum coatings on steel, immersed in deaerated sulfuric acid electrolyte. The corrosion simulations employed in this chapter were generated by coupling a finite element model of charge and mass transfer in the electrolyte with time integration to calculate the associated change in geometry due to metal dissolution. Corrosion tests were performed on immersed coated steel samples, with continuous monitoring of the open circuit potential and periodic measurements of coating geometry via contact profilometry.

The simulated corrosion test on the zinc coating showed two defining characteristics – an initial period of low open circuit potential (~-0.7 V vs SHE) which rose sharply to match that of uncoated steel after 80 minutes, and preferential thinning of the zinc coating adjacent to the steel substrate. In the corrosion test, the distribution of zinc loss in the coating measured by profilometry was found to match the simulation quite, though the total rate of zinc dissolution was about 20 percent higher than predicted. The measured open circuit potential matched the behavior of the simulation, though the potential was approximately 100 mV lower than predicted during the initial period of cathodic protection. Divergence between the simulation and the corrosion test was observed after 40 minutes, at which point the remaining zinc coating became passive and ceased to provide cathodic protection to the steel.

The corrosion simulation of the aluminum coating was marked by low corrosion rates for both the aluminum and steel, a constant corrosion potential very close to that of uncoated steel, and corrosive attack on both the steel and the aluminum distributed evenly over the surface, with the aluminum dissolving at approximately half the rate of the exposed steel. The corrosion test again showed good qualitative agreement with the simulation, with the observed open circuit potential fairly constant and close to the corrosion potential of the steel, and even distribution of coating loss. The coating and substrate were observed to corrode at similar rates, in contrast to the model prediction.

Overall, the corrosion simulations on galvanic zinc and aluminum coatings in sulfuric acid presented in this chapter were quite successful at reproducing the distinctive qualitative corrosion behavior of the two coatings, and show reasonable quantitative agreement with potential and profilometry measurements. Further improvement of the predictive power of simulations will likely be based on improved understanding of the changing surface conditions of corroding metals, in order to capture phenomena such as active/passive transitions, the tendency for localization of corrosion, and the effects of electrolyte composition on surface reactivity.

5. Modeling localized corrosion of multilayer thin films through an effective medium approximation

5.1 Introduction

While the galvanic corrosion model presented in Chapter 4 was reasonably successful at capturing the relative corrosion behavior of pure zinc and aluminum, the limitations of the model for prediction of medium-term corrosion behavior, and dealing with localized corrosion, illustrate the difficulty of applying computational corrosion models real-world situations or complex geometries. Although localization is common or even critical to technologically-relevant corrosion problems, it is rarely treated computationally due to its complexity; there is a limited understanding of the surface chemistry involved in passive film formation and breakdown, and the inherently unstable nature of localized corrosion resists computational treatment by conventional continuum equations. Typically, localized corrosion occurs due to the formation of stable or metastable corrosion pits, which are sustained due to the concentrated electrolyte contained within the pit interior that renders them preferential sites for anodic metal dissolution [58]. What models do treat pitting corrosion generally break the problem into an initiation phase, in which a corrosion pit forms following passive film breakdown and rapid localized anodic dissolution of the metal, and a propagation phase, in which an actively corroding pit grows over time due to continued anodic activity [64,66,70]. The initiation of corrosion pits is an extremely challenging problem for deterministic computational methods, particularly as the conditions for initiating a corrosion pit are highly dependent on electrode heterogeneity and surface defects. On the other hand, many authors have successfully applied computational models to the problem of corrosion pit propagation, most commonly by solving field-based equations for diffusion of dissolved species within an individual corrosion pit of predefined geometry [68,70,72,106]. For instance, Laycock and White applied a finite element diffusion model to propagation of a preexisting corrosion pit in stainless steel, generating criteria for stable or metastable pit growth based on geometry and electrolyte composition, and predictions of pit morphology resulting from different applied potentials [70]. In a later work, Laycock et al. coupled this deterministic model to a stochastic model for pit initiation, showing good ability to predict pitting potentials based on chloride concentration and surface roughness [71].

While these approaches produce useful predictions in systems for which a relatively small number of discrete corrosion pits are expected to form, they suffer from several limitations. In particular, for materials with a high susceptibility to pitting in a given environment, corrosion damage may take the form of a large number of small and relatively unstable pits, which eventually produce an interconnected network of pores. This is particularly relevant in the case of sacrificial corrosion coatings, which are of vital industrial importance for protection of mild steel. Such coatings are designed to be sufficiently active to provide cathodic protection to the steel substrate, while also decreasing overall corrosion rates due to a moderate level of surface passivity. However, localized corrosion may degrade their effectiveness as barriers long before complete coating dissolution, resulting in an increase in corrosion rates over time due to the ability of dissolved O_2 and other reactive species to diffuse through the porous film to cathodically active sites on the substrate [107]. The importance of this effect is illustrated by a number of recent studies showing that functionally graded or multilayer coatings can often provide greatly improved corrosion protection to steel substrates, relative to monolithic coatings of equivalent thickness [12,24–26,80,108,109]. For instance, Fei and Wilcox demonstrated multilayered Zn/Ni coatings that increased protection time in the neutral salt spray test by an order of magnitude relative to pure Zn or Ni coatings [80], while Charrier et. al. showed that multilayer Al/Ti coatings have improved corrosion resistance based on potentiostatic polarization measurements and superior protection time in the salt spray test, relative to pure Al or pure Ti [12]. These improvements are most commonly attributed to the ability of multilayer coatings to resist through-going porosity due to synergy between corrosion resistant barrier layers, and more active layers that provide cathodic protection, resulting in a decrease in the overall corrosion rate [12,24,26,80].

In this chapter, we present an alternate, effective medium approach to modeling of localized corrosion. Our inspiration for this work derives from the observation that many other disciplines in the physical sciences face problems in which localization phenomena occur, but where average macroscopic properties inclusive of such localization are still of interest and must be modeled and designed for. For example, the effective mechanical properties of multiphase materials [110–115] can be approximated at the continuum level by effectively averaging over local heterogeneities. In such materials the deformation and failure is often a sequence of localization events, and yet mechanical "damage parameters" can be used to adjust effective local properties at the macroscale without focusing on the details of individual localization events [116,117]. In the field of corrosion, however, such techniques have not been widely explored, possibly due to the lack of detailed microscopic models of corrosion. Hinderliter et al. used an effective medium approximation to model organic corrosion coatings damaged through UV exposure and water infiltration, where the damaged sections of the coating were handed as RC equivalent circuits [118]. This model was able to replicate observed changed in EIS spectra for damaged coatings, but lacked any means to predict or simulate the damage process itself, or incorporate any continuous gradients in the degree of coating damage. Brown and Barnard applied a finite difference model to corrosion of an Al-Zn alloy coating, in which finite difference cells were permitted to be partially filled with electrolyte as corrosion damage penetrated the coating, with local diffusion rates adjusted accordingly [45,46]. The Al-Zn coatings simulated by this model showed a decrease in corrosion rate with microstructural refinement, in qualitative agreement with experimental observations; however, the procedure required the use finite difference cells much smaller than the microstructural features being used, and thus required detailed information on the 3D microstructure of the coating being modeled.

The goal of the model we present in this chapter, conversely, is to treat the corroding material as a continuum using an effective medium approximation, with the effects of microstructure handled through the introduction of a characteristic length scale parameter δ. This model offers a simple means of capturing the most relevant scale-dependent phenomena in a straightforward and flexible way, which can also be easily calibrated against a few simple experiments.

5.2 Model

The electrochemical model presented in this study calculates the distribution of potential and electrolyte concentration by solving field-based equations for mass transfer and overall charge balance. The corroding material is treated as a porous electrode with a continuously variable porosity given by the electrolyte fraction f_{elec}, which may take any positive value less than or equal to 1. Although the developments that follow are generally amenable to numerical implementation for arbitrary geometries and in arbitrary dimensions, without loss of generality we elect to present the model in a one-dimensional version here, as shown in Fig. 5.1 (a), with the corroding electrode on the left, adjacent an electrolyte region that represents a diffusion layer of fixed thickness, for which f_{elec} is fixed at 1 everywhere. Rates of anodic and cathodic reactions are determined by an electrolyte potential field ϕ, as well as the local composition of the electrolyte.

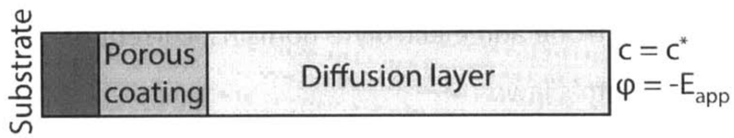

Figure 5.1 Schematic of 1-D modeling domain

To focus the discussion, and again as an example of the utility of the approach, we also treat a system that will be the focus of our experiments in a subsequent section, involving a corroding aluminum alloy coating over steel, in a salt water environment. A large number of dissolved species are expected to be present in the electrolyte during the corrosion process, including O_2, H^+, OH^-, Na^+, Cl^-, Al^{3+}, as well as metal-hydroxide and metal-chloride complexes. In order to fully calculate the composition of the electrolyte, the distribution of each of these species must be solved simultaneously, while accounting for both interfacial redox reactions and association/dissociation reactions within the electrolyte. Although this approach has been applied successfully in several cases [5,16], it is quite computationally demanding, and difficult to scale up to more complex systems. However, experimental work on pitting of aluminum has shown that in many cases, the primary factor determining susceptibility to pitting is the concentration of Cl^- ions, which are critical to disrupting the protective oxide film and preventing repassivation of existing pits [10]. Since Cl^- is the only anion present in significant quantities in the acidified pit interiors, due to electroneutrality the aggressiveness of the electrolyte can be approximately determined from the overall ionic charge density of the electrolyte. Thus in order to simplify the simulation, while still capturing the first-order concentration effects in a simple way, the ionic concentration of the electrolyte is parameterized by a single variable field $c_{\mathrm{Al}}(x)$ representing the total concentration of dissolved aluminum species, from which the concentration of Cl^- ions may be inferred. It is assumed that the dominant cathodic reaction is oxygen reduction, which may be diffusion or activation limited, and so the concentration of dissolved O_2 is tracked through an independent concentration field $c_{\mathrm{O}_2}(x)$, to produce a simplified description of electrolyte composition that permits approximation of both anodic and cathodic reaction rates, when combined with the potential $\phi(x)$.

5.2.1 Governing equations

Within the porous electrode and electrolyte domains, current density is considered to relate to potential through Ohm's law:

$$j = -\sigma_{\mathrm{eff}} \frac{\partial \phi}{\partial x} \tag{.51}$$

where the effective local conductivity σ_{eff} is approximated as:

$$\sigma_{\mathrm{eff}} = (f_{\mathrm{elec}})^2 (\sigma_0 + \Lambda c_{\mathrm{Al}}) \tag{5.2}$$

where σ_0 is the conductivity of the bulk solution and Λ is the molar conductivity of AlCl_3. The term $(f_{\mathrm{elec}})^2$ is applied to account for the decreased mobility of ions and tortuosity of diffusion pathways within the porous electrode; although it is a crude approximation, it has been applied successfully in corrosion modeling by other authors [45], and avoids issues such as percolation thresholds, which are by nature absent in this system.

Mass transport is assumed to occur primarily through Fickian diffusion within the diffusion layer, corrected in a similar way based on electrolyte fraction:

$$J_i = -D_{\mathrm{eff}} \frac{\partial c_i}{\partial x} \tag{5.3}$$

$$D_{i,\mathrm{eff}} = (f_{\mathrm{elec}})^2 D_i \tag{5.4}$$

where c_i and J_i are the concentration and flux of a given dissolved species, and D_i is the diffusion coefficient in the bulk solution.

Thus in the steady state:

$$\frac{\partial c_i}{\partial t} = -\frac{\partial J_i}{\partial x} + R_i = 0 \tag{5.5}$$

where R_i is the local generation rate of species i.

Interfacial charge transfer between the electrode and electrolyte are assumed to occur through two irreversible redox reactions:

$$\mathrm{Al(s) \rightarrow Al^{3+}(aq) + 3e^-} \tag{5.6}$$

$$\mathrm{O_2(g) + 2H_2O(aq) + 4e^- \rightarrow 4OH^-(aq)} \tag{5.7}$$

The metal dissolution reaction occurs solely within the porous electrode. It is assumed that the kinetic reaction rate R_k for a fully activated surface has an exponential dependence on potential, absent any effects due to concentration:

$$R_\mathrm{k} = k_\mathrm{0,a} \exp\left(\frac{E - E^0_\mathrm{ref,a}}{\beta_\mathrm{a}}\right) \tag{5.8}$$

$k_\mathrm{0,a}$ is the reaction rate constant, $E = -\phi$ is the electrode potential, $E^0_\mathrm{ref,a}$ is a baseline electrode potential, and β_a is the anodic Tafel parameter. Several modifications are applied to the reaction rate equation, to account for passivity, local surface area density, and concentration effects, to give a total reaction rate:

$$R_\mathrm{Al} = a_v \theta \left(\frac{c_\mathrm{sat} - c_\mathrm{Al}}{c_\mathrm{sat}}\right) R_\mathrm{k} \tag{5.9}$$

where a_v is the specific surface area, θ is the local fraction of pitting sites that are in the active state, and c_sat is concentration of dissolved aluminum species in the fully saturated electrolyte. For the porous electrode, the specific surface area is given by:

$$a_v = 4\nu_0(f_\mathrm{elec})(1 - f_\mathrm{elec}) + \left|\frac{\partial f_\mathrm{elec}}{\partial x}\right| \tag{5.10}$$

The first term gives the internal specific surface area, which is 0 for f_{elec} equal to 0 or 1, and has a maximum of ν_0 at $f_{\text{elec}} = 0.5$. The second term gives the added interfacial specific surface area due to changes in the electrolyte fraction. The quantity $1/\nu_0$ may be considered to be a characteristic length scale for the porous electrode following significant pitting.

To approximate the fraction of pitting sites that are in the active state, the local overpotential for pitting η_{pit} is calculated according to:

$$\eta_{\text{pit}} = E - E_{\text{pit}} - \alpha_{\text{pit}} \log\left(\frac{c_{\text{Cl}^-}}{c_{\text{Cl}_0^-}}\right) \tag{5.11}$$

where E_{pit} is the measured pitting potential for the material, $c_{\text{Cl}_0^-}$ is the chloride ion concentration in the bulk solution, $c_{\text{Cl}^-} = c_{\text{Cl}_0^-} + 3c_{\text{Al}}$ is the local chloride ion concentration, and α_{pit} is a parameter determining the effect of chloride ion concentration on the pitting potential. The logarithmic relation between chloride concentration and pitting potential of aluminum alloys has been demonstrated in a number of studies, and α_{pit} is generally found to have values in the range of 50-150 mV [123–125], and so a reasonable consensus value of 100 mV is used in the model. In addition, it is assumed that the available pitting sites have pitting potentials falling within a range of values with standard deviation γ_{pit}, so that the fraction of active pitting sites is given by:

$$\theta = \frac{\exp\left(\frac{\eta_{\text{pit}}}{\gamma_{\text{pit}}}\right)}{A_0 + \exp\left(\frac{\eta_{\text{pit}}}{\gamma_{\text{pit}}}\right)} \tag{5.12}$$

where A_0 is a constant fitting parameter.

The cathodic oxygen reduction reaction is assumed to under mixed diffusion-activation control, with first-order dependence on the concentration of dissolved oxygen:

$$R_{\text{O}_2} = -\nu c_{\text{O}_2} k_{0,\text{c}} \exp\left(\frac{(E - E^0_{\text{ref,c}})}{\beta_{\text{c}}}\right) \tag{5.13}$$

where $k_{0,\text{c}}$ is the reaction rate constant $E^0_{\text{ref,c}}$ is a baseline electrode potential, and β_{c} is the anodic Tafel parameter.

In order to maintain electroneutrality, the total density of local charge generation in the electrolyte is balanced by the ionic current flows determined through Ohm's law:

$$-4FR_{\mathrm{O}_2} + 3FR_{\mathrm{Al}} = \sigma_{\mathrm{eff}} \frac{\partial^2 \phi}{\partial x^2} \tag{5.14}$$

where F is the Faraday constant. Likewise, the steady state condition for each concentration field is determined through the balance of local generation or consumption of each species, and Fickian diffusion:

$$-D_{i,\mathrm{eff}} \frac{\partial^2 c_i}{\partial x^2} = R_i \tag{5.15}$$

The value of the various transport and solubility parameters used for model calculations are shown in Table 5.1.

Table 5.1 Electrolyte transport and solubility parameters used in the model

Parameter	Description	Value	Source
D_{Al}^0	Base diffusion coefficient for dissolved Al	$0.54 \times 10^{-9} \mathrm{m}^2/\mathrm{s}$	[44]
$D_{\mathrm{O}_2}^0$	Base diffusion coefficient for dissolved O^2	$2.4 \times 10^{-9} \mathrm{m}^2/\mathrm{s}$	[44]
σ_0	Conductivity of bulk solution (50 mM NaCl)	0.47 S/m	[44]
Λ	Molar conductivity of $AlCl_3$	0.039 m^2S/mol	[44]
$c_{\mathrm{Al,sat}}$	Solubility limit for dissolved Al species	3400 mol/m^3	
c_{Al}^*	Bulk concentration of dissolved Al species	0.001 mol/m^3	
$c_{\mathrm{O}_2}^*$	Bulk concentration of dissolved O_2	0.25 mol/m^3	[44]
x_{diff}	Diffusion layer thickness	$500 \times 10^{-6} \mathrm{m}$	

5.2.2 Boundary Conditions

At the substrate/film interface, dissolved oxygen is reduced according to Eq. (5.6), with the reaction rate given in Eq. (5.13). The reaction rate constant $k_{0,\mathrm{c}}$ is assumed to be significantly higher for the substrate than for the film, so that oxygen reduction is primarily diffusion-limited at the substrate. The associated boundary conditions are:

$$-\mathrm{D}_{\mathrm{O_2,eff}}\frac{\partial c_{\mathrm{O_2}}}{\partial x}(x=0) = -c_{\mathrm{O_2}}k_{0,\mathrm{c}}\exp\left(\frac{\left(E - E^0_{\mathrm{ref,c}}\right)}{\beta_{\mathrm{c}}}\right) \tag{5.16}$$

$$-D_{\mathrm{Al}}\frac{\partial c_{\mathrm{Al}}}{\partial x}(x=0) = 0 \tag{5.17}$$

$$-\sigma_{\mathrm{eff}}\frac{\partial \phi}{\partial x}(x=0) = -4Fc_{\mathrm{O_2}}k_{0,\mathrm{c}}\exp\left(\frac{\left(E - E^0_{\mathrm{ref,c}}\right)}{\beta_{\mathrm{c}}}\right) \tag{5.18}$$

At the diffusion layer/bulk electrolyte interface, corresponding to the right boundary in Figure 5.1, the concentration of dissolved oxygen and aluminum species are maintained at their bulk concentrations, and the electrolyte potential is held at a specified applied potential:

$$c_{\mathrm{Al}}(x=D) = c^*_{\mathrm{Al}} \tag{19}$$

$$c_{\mathrm{O_2}}(x=D) = c^*_{\mathrm{O_2}} \tag{20}$$

$$\phi(x=D) = -E_{\mathrm{app}} \tag{21}$$

5.3.1 Calibration of the model from cyclic voltammetry data

One of the objectives of the modeling approach presented in this chapter is to generate reasonable behavior for the corrosion behavior of aluminum alloy thin films, without the need for a detailed microscopic model of the material. In accordance with this principle, the kinetic parameters used to model a given film were extracted solely from cyclic voltammetry measurements. Aluminum alloy electrodeposits of three different compositions were used to test the model, which were deposited according to the procedures described in Chapter 2 of this thesis. For simplicity, the different electrodeposits will be denoted as AA1, AA2, and AA3, with corrosion resistance increasing in the order AA3 < AA2 < AA1. The electrodeposition procedures and compositions of the three films is summarized in Table 5.2.

Table 5.2 Aluminum alloys used in the model

Label	Electrodeposition Bath	j_{dep}	Composition
AA1	EMIC:AlCl$_3$ 2:1 + 0.02 M ZrCl$_4$	80 Am^{-2}	Al-6 at.% Zr
AA2	EMIC:AlCl$_3$ 2:1 + 0.02 M ZrCl$_4$ + 0.1 M ZnCl$_2$	40 Am^{-2}	Al-46 at.% Zn-8 at.% Zr
AA3	EMIC:AlCl$_3$ 2:1 + 0.02 M ZrCl$_4$ + 0.1 M ZnCl$_2$	80 Am^{-2}	Al-34 at.% Zn-5 at.% Zr

Figure 5.2 (a) shows a typical CV for an AA1 thin film in aerated 50 mM NaCl solution. The film was significantly activated during the first anodic scan, as can be seen by the significant decrease in the open circuit potential and increase in anodic dissolution on the returning cathodic scan, indicating a significant disruption of surface passivity during anodic polarization. The pitting potential was estimated as the potential at which the anodic current density surpassed 1 Am^{-2} on the initial anodic scan; in both cases, this point corresponded closely to the elbow visible on the second scan. This pitting potential E_{pit} is used for the calculation of pitting overpotential η_{pit} in Eq. (5.11). On the second and subsequent scans, the polarization response became much more consistent and showed evidence of significant residual anodic activity below the pitting potential measured on the first anodic scan, suggesting that local anodes activated during the first scan did not fully repassivate during the cathodic scan. This residual activity was found to have an excellent fit to an exponential relationship between potential and current density:

$$j_{\mathrm{a}} = k_{0,\mathrm{a}} \exp\left(\frac{E - E^0_{\mathrm{ref,a}}}{\beta_{\mathrm{a}}}\right) \tag{22}$$

$$j_{\mathrm{c}} = k_{0,\mathrm{c}} \exp\left(\frac{E - E^0_{\mathrm{ref}}}{\beta_{\mathrm{c}}}\right) \tag{23}$$

$$j_{\mathrm{net}} = j_{\mathrm{a}} - j_{\mathrm{c}} \tag{24}$$

where j_a, j_{c}, and j_{net} are the anodic, cathodic, and net current density, $j_{0,\mathrm{a}}$ and $j_{0,\mathrm{c}}$ are the anodic and cathodic current densities. The best fit value for these parameters was used as the kinetics of the metal dissolution reaction in the active state.

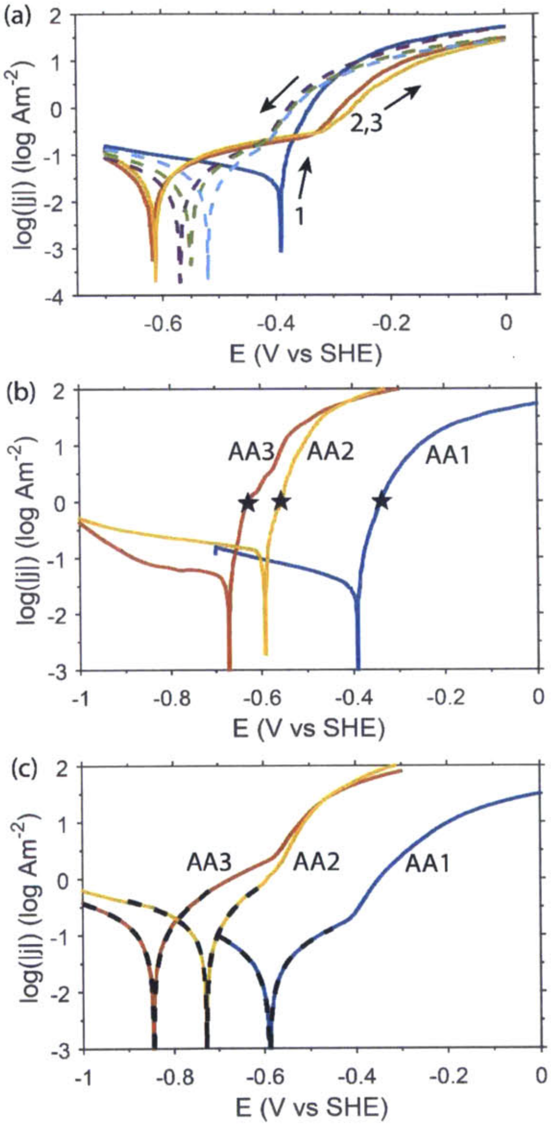

Figure 5.2 (a) Cyclic voltammogram showing three full cycles for alloy AA1. Solid lines mark anodic scans, and dashed lines mark cathodic scans. (b) Initial anodic scans for all three alloys. (c) Averaged second scans for all three alloys

The initial anodic polarization curves for each of the three alloys is shown in Figure 5.2 (b), with the calculated pitting potential for each marked with a star. The average of the second anodic and cathodic scan for each of the three alloys, with the best fit for the active dissolution kinetics marked with a dashed black line, is shown in Figure 5.2 (c). In all three cases, the average scans in Figure 5.2 (c) exhibit an excellent fit to exponential kinetics, as well as a visible elbow shaped feature near the pitting potential; this may be interpreted as the potential at which new anodic sites may be initiated in the film. However, it should be noted that the observed cathodic currents in Figure 5.2 (c) may be due to a range of cathodic reactions, including oxygen reduction, hydrogen evolution, and replating of dissolved metal ions. In addition, the cathodic current density tended to vary significantly between samples, and increase steadily with each scan as the surface became increasingly disturbed. Thus, despite the excellent exponential fit, the cathodic reaction rate in is certain to significantly overestimate the rate of the oxygen reduction reaction at steady state conditions. Thus, for the model identical values of $k_{0,\mathrm{c}} = 1.85 \times 10^{-10}$ mol/m^{2}s and $\beta_{\mathrm{c}} = -0.6$ V were used for calculation of the cathodic reaction rate in the model, for all three of the aluminum alloy coatings. These values should not be construed to represent a true measurement of the oxygen reduction kinetics. The kinetic parameters extracted from the polarization data and used in the model are summarized in Table 5.3.

Table 5.3

Materials specific electrochemical parameters used in model calculations.

Material	Parameter	Description	Value	Source
AA1	$k_{0,\mathrm{a}}$	Interfacial rate constant	3.21×10^{-13} mol/(m^{2}s)	Fit to CV
AA1	$E^0_{\mathrm{ref,a}}$	Reference potential for MDR	-1.6 V vs SHE	[44]
AA1	β_a	Anodic Tafel parameter	0.179 V	Fit to CV
AA1	E_pit	Pitting potential	-0.315 V vs SHE	Fit to CV
AA2	$k_{0,\mathrm{a}}$	Interfacial rate constant	3.14×10^{-7} mol/(m^{2}s)	Fit to CV
AA2	$E^0_{\mathrm{ref,a}}$	Reference potential for MDR	-0.76 V vs SHE	[44]
AA2	β_a	Anodic Tafel parameter	0.134 V	Fit to CV
AA2	E_pit	Pitting potential	-0.500 V vs SHE	Fit to CV
AA3	$k_{0,\mathrm{a}}$	Interfacial rate constant	1.76×10^{-6} mol/(m^{2}s)	Fit to CV
AA3	$E^0_{\mathrm{ref,a}}$	Reference potential for MDR	-0.76 V vs SHE	[44]
AA3	β_a	Anodic Tafel parameter	0.176 V	Fit to CV
AA3	E_pit	Pitting potential	-0.585 V vs SHE	Fit to CV
All	α_pit	Chloride concentration sensitivity parameter	0.1 V	[37–39]
All	γ_pit	Pitting transition width	0.05 V	Estimated from CV
All	δ	Characteristic length scale	2×10^{-6}m	Estimated from microstructure
Aluminum	$k_{0,\mathrm{c}}$	Interfacial rate constant for ORR	1.85×10^{-10}m/s	Estimated from corrosion rate
Steel	$k_{0,\mathrm{c}}$	Interfacial rate constant for ORR	1.85×10^{-4}m/s	Estimated from corrosion rate
All	$E^0_{\mathrm{ref,c}}$	Reference potential for ORR	1.22 V vs SHE	[44]
All	β_c	Tafel slope for ORR	-0.6 V	Estimated from corrosion rate

5.4.1 Calculation of steady state concentration and potential distributions

The above equations are solved on the 1-D domain shown schematically in Figure 5.1 using the COMSOL Multiphysics software using the LiveLink for Matlab package for scripted control of model setup and analysis. Each finite element solution gives the steady state distribution of potential and dissolved species for a specified applied potential E_app and electrode state, as parameterized by $f_{\text{elec}}(x)$. The typical behavior of the model is illustrated by the steady state solution in Figure 5.2, for a representative aluminum alloy film of 100 μm thickness, with $f_{\text{elec}} = 0.01$ to represent a nearly intact coating. The parameters used for the calculation were taken from the listed values for the alloy AA1, in Table 5.3. The film depicted in Figure 5.2 has been moderately anodically polarized, with E_{app} just high enough to induce localized corrosion. The calculated concentration distributions in Figure 5.2 (a) show significant concentration of dissolved aluminum species within the interior of the coating, while the concentration of dissolved O_2 drops off very quickly due to the limited diffusion within the intact coating. The concentrations within the diffusion layer, however, are quite flat and very close to the bulk concentrations, as diffusion through the intact coating is rate limiting for mass transport. A similar trend is seen in the gradient of electrolyte potential in Figure 5.2 (b). The potential within the diffusion layer is very close to the boundary potential $-E_{\text{app}}$, but increases approximately 70 mV within the coating due to the low mobility of dissolved ions, and net outward current density due to aluminum dissolution within the coating interior.

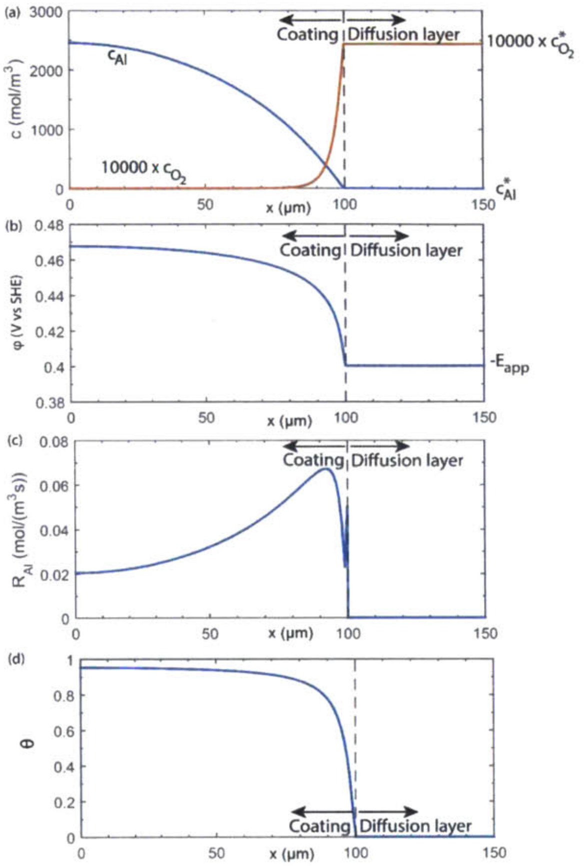

Figure 5.3 Typical steady state solution, for 100 μm AA1 film with $f_{\text{elec}} = 0.01$, showing calculated (a) concentration fields, (b) electrolyte potential, (c) aluminum dissolution rate, and (d) activity fraction within the interior of the coating.

The distribution of aluminum dissolution shown in Figure 5.3 (c) reflects contributions from the several factors included in Eq. (5.9). Due to the higher electrolyte concentration deeper in the coating, the fractional activity θ is increased due to higher values of η_{pit}, as is shown in Figure 5.3 (d). However, this effect is counteracted by charge and mass transport limitations. The kinetic dissolution current R_{k} is dependent on potential, and so decreases deeper within the coating due to IR potential drop. Likewise, the dissolution current decreases linearly to 0 as the value of c_{Al} approaches c_{sat}. The competition between these factors results in the peak in aluminum dissolution 10 μm into the coating in Figure 5.2 (c). Finally, the specific surface area a_{v} is constant throughout the interior of the coating, but has a high value at the coating surface due to the sharp gradient in electrolyte fraction. This is illustrated by the sharp peak in R_{Al} at the surface of the coating in Figure 5.3 (c).

5.4.2 Simulated polarization response of aluminum alloy film

Figure 5.4 shows the results of a simulated anodic polarization scan on an aluminum alloy film, using the parameter values listed for the alloy AA1 in Table 5.2. In order to generate the curve, the applied potential E_{app} was swept from -0.7 V vs SHE to 0 V vs SHE in increments of 10 mV, and a steady state solution calculated for each. The net current density at each potential was calculated based on the total rates of aluminum dissolution and oxygen reduction, to generate a complete polarization curve for the film. All solutions were calculated for a static $f_{\text{elec}} = 0.01$, and so does not take into account changes in the electrode geometry due to dissolution. The simulated film exhibits a passive to active transition at a potential of approximately -0.4 V vs SHE, visible in the rapid increase in anodic current density in Figure 5.4 (a), and increase in θ and electrolyte concentration in Figure 5.4 (b-c). This transition occurs approximately 50 mV below the value of E_{pit} maked on Figure 5.4 (a); this is because the value E_{pit} represents the threshold for pitting in the bulk solution, while in the interior of the coating the higher value of c_{Al} permits activation at a somewhat lower potential. This effect is self-reinforcing, in that a more concentrated electrolyte within the interior of the coating increases the overpotential for pitting, which subsequently increases the rate of Al dissolution. As a result the simulated polarization curve displays a much more rapid increase in current density over a small range of potential than would be found based on exponential dissolution kinetics alone.

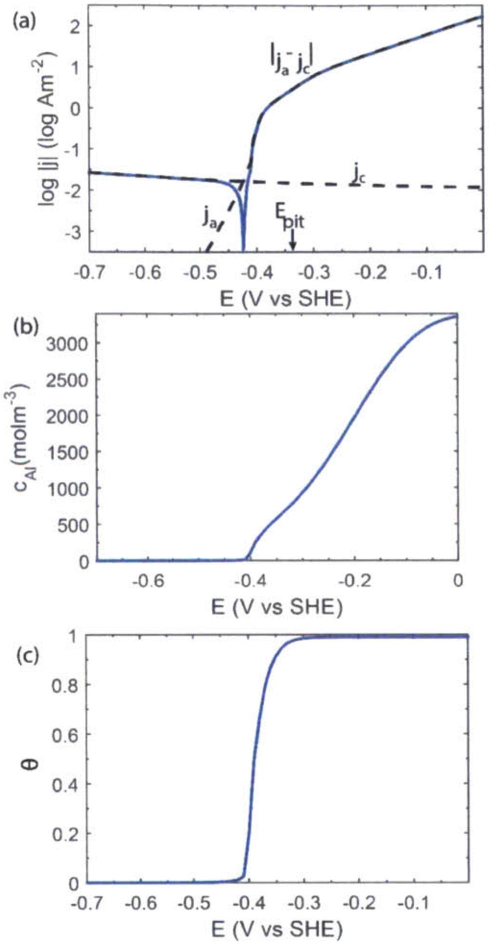

Figure 5.4 Polarization response of a 20 μm AA1 film, showing (a) calculated current density, (b) maximum aluminum concentration, and (c) average activity fraction as a function of potential.

5.4.3 Time-dependent corrosion simulations

In order to generate time-dependent corrosion simulations, steady state solutions such as those shown in Figure 5.1 are used to calculate instantaneous metal dissolution rates via Eq. (5.9), which are then integrated over time to produce time-dependent simulations of the corrosion process. The change in $f_{\mathrm{elec}}(x)$ over an individual time step Δt is given by:

$$\Delta f_{\mathrm{elec}} = R_{\mathrm{Al}} \frac{\rho_{\mathrm{Al}}}{A_{\mathrm{w}}} \Delta t \tag{5.22}$$

where ρ_{Al} and A_w are the density and atomic weight of aluminum. In order to minimize integration error, the size of the time step is adjusted each iteration such that the change in the corrosion potential is no greater than 5 mV. This procedure was found to produce simulations with less than 5% integration error in all cases.

In addition to loss of material through metal dissolution, it is to be expected that mechanical failure may occur under when an intact layer is undercut sufficiently by corrosion damage to the underlying material. This behavior is implemented in a straightforward manner by the model, though use of a threshold f_{c} representing the local electrolyte fraction at which the porous coating is no longer able to provide full mechanical support to layers above. Then, if at any point in the coating the local electrolyte fraction is greater than f_c, the maximum allowed electrolyte fraction for all of the coating exterior to that point is given by:

$$f_{\max} = \frac{f_{\mathrm{elec}} - f_{\mathrm{c}}}{1 - f_{\mathrm{c}}} \tag{5.23}$$

Under free corrosion conditions, due to electroneutrality the potential adjusts such that there is zero net interfacial current density. However, due to the positive feedbacks present in the model, in some situations there is no exact solution that produces zero net current density. Particularly in the case of highly intact coatings near the pitting potential, a very small increase in potential may cause a discontinuous transition to an activated state. Thus, in order to generate reliable and reproducible steady state solutions, the corrosion potential is selected according to this procedure:

1. The applied potential E_{app} is increased in increments of 5 mV, until a steady state solution with positive net current density is discovered
2. The potential E_{app} is decreased in increments of 1 mV, until a steady state solution with negative net current density is discovered
3. The calculated solution is taken from the weighted average of the two previous solutions, with the weighting chosen to satisfy the zero net current density condition

In conditions for which there is a single stable solution, the two solutions that are averaged together are very similar, so the effect of this procedure is negligible. Under conditions in which the two solutions represent an active state, with positive net current density, and a passive state, with negative net current density, the averaged solution will not, in general, be an exact solution to the governing equations of the model. Under this circumstance, this procedure converges very reliably to the same solution, consisting of the "least-active" activated state, and the passive state that can exist at the same potential.

5.4.4 Corrosion simulations of single and multilayer aluminum alloy coatings

To evaluate the effect of layered coatings, free corrosion simulations were performed on four coatings on steel substrates: two single layer coatings consisting of materials AA1 and AA3, and two bilayer coatings AA1/AA3 and AA3/AA1, where second material listed is on the outside. AA3 is significantly more active than AA1, and so is expected to be attacked preferentially. All simulated coatings were 8 μm in thickness, with the bilayers split evenly between the two materials. The simulation was performed with a starting porosity of $f_{\text{elec}} = 0.05$ throughout the coating; it was then allowed to evolve over time according to Eq. (5.22). Figure 5.5 (a) shows the evolution of the simulated corrosion potential for each of the four coatings over a period of up to 80 days, with an 'x' marking the predicted point of complete coating dissolution, if applicable, while Figure 5.5 (b) shows the total corrosion current density over the simulation for each.

The simulated AA3 single layer has the shortest life of the four coatings. The initial corrosion potential is -0.69 V vs SHE, increasing over 28 days to -0.65 V vs SHE, at which time the coating is fully dissolved and fails abruptly. The relatively rapid failure of the AA3 single layer may be attributed to galvanic coupling between the steel substrate and the porous coating; as can be seen from the calculated f_{elec} distributions in Figure 5.5 (c), significant damage is expected to quickly propagate through the full depth of the film, resulting in a decrease in the effectiveness of the coating at blocking diffusion of dissolved O_2 to the cathodically active steel surface. As a result the corrosion current density increases rapidly from the outset of the test, as can be seen in Figure 5.5 (b).

The simulated AA1 single layer, in contrast, has a very slow corrosion rate, and is largely intact at the end of the 80 day simulation period, as can be seen in the f_{elec} distribution in

Figure 5.5 (d). While the damage is spread fairly evenly throughout the depth of the coating, the overall corrosion rate is sufficiently low that it has not significantly degraded the properties of the coating. However, the low corrosion rate is partially explained by the poor cathodic protection supplied to the substrate. For instance, in the initial state of the corrosion simulation, the total anodic current density for the AA1 coating on steel is 0.021 Am^{-2}, which is divided between dissolution current density of 0.007 Am^{-2} for the AA1 layer, and 0.014 Am^{-2} for the steel substrate. Therefore the AA1 coating would not be expected to have a significant ability to protect any steel exposed at pores or defects in the coating. In addition, the AA1 coating would be eventually expected to fail mechanically due to undercutting and formation of voluminous iron oxides on the steel surface, though this behavior is not implemented in the model.

The corrosion potential of the simulated AA1/AA3 bilayer coating in Figure 5.5 (a) follows a similar progression to that of the AA3 coating with a reduced corrosion rate, starting at -0.68 V vs SHE initially and rising slowly to -0.65 V vs SHE at day 47, at which point the AA3 layer is fully dissolved, and the corrosion potential rises abruptly to that of the AA1 barrier layer, which has remained fully intact due to cathodic protection from the AA3 layer, as can be seen in the calculated values for f_{elec} shown in Figure 5.5 (e). The effect of the bilayer structure, however, is evident in the low corrosion current density in Figure 5.5 (b), compared to the AA3 single layer. While the corrosion rate of the AA3 single layer increases rapidly from the outset of the simulation, for the AA1/AA3 bilayer, the intact AA1 barrier layer prevents easy diffusion of dissolved O_2 to the steel as the AA3 layer becomes damaged, and so the corrosion rate reflects the much slower kinetics of O_2 reduction on the aluminum surface. The corrosion rate increases slightly, however, due the increase in surface area as the AA3 layer become increasingly porous, then decreases again as the porous AA3 layer dissolves fully. The full lifetime of the AA3 layer of the bilayer is 46 days, representing a 64 percent increase over the 28 day lifetime of the AA3 single layer despite being only half the thickness.

The corrosion potential of the AA3/AA1 bilayer is quite close to that of the AA3 single layer and AA1/AA3 bilayer, despite the fact that the AA3 layer is shielded from the electrolyte by the AA1 barrier. The low corrosion potential is due to dissolution of the sacrificial AA3 layer via diffusion through the barrier, which is possible to a sufficient degree to allow the AA3 layer to determine the overall potential of the system. This is illustrated by the calculated f_{elec} distributions in Figure 5.5 (f), which show that the initial material loss is expected to come entirely from the AA3 underlayer. In addition, while the corrosion rate of the AA1/AA3 bilayer shown in Figure 5.5 (b) is expected to increase slightly due to surface roughening, in the case of the AA3/AA1 bilayer the outer surface remains fully intact, and so the effective area for oxygen reduction does not increase, and the corrosion rate stays constant. The behavior changes dramatically, however, starting at day 57, at which point the AA3 underlayer reaches the threshold porosity $f_c = 0.8$ to initiate mechanical failure of the AA1 barrier. This results in the rapid increase in the corrosion current density in Figure 5.5 (b), and complete dissolution of the coating at day 61. Therefore, while the outer barrier AA3/AA1 bilayer is somewhat more effective at extending the life of the sacrificial AA3 layer than in the AA1/AA3 bilayer, while providing a similar degree of cathodic protection to the steel, the use of an outer barrier layer is also expected to increase the degree of localization of corrosion, and will tend to result in abrupt mechanical failure.

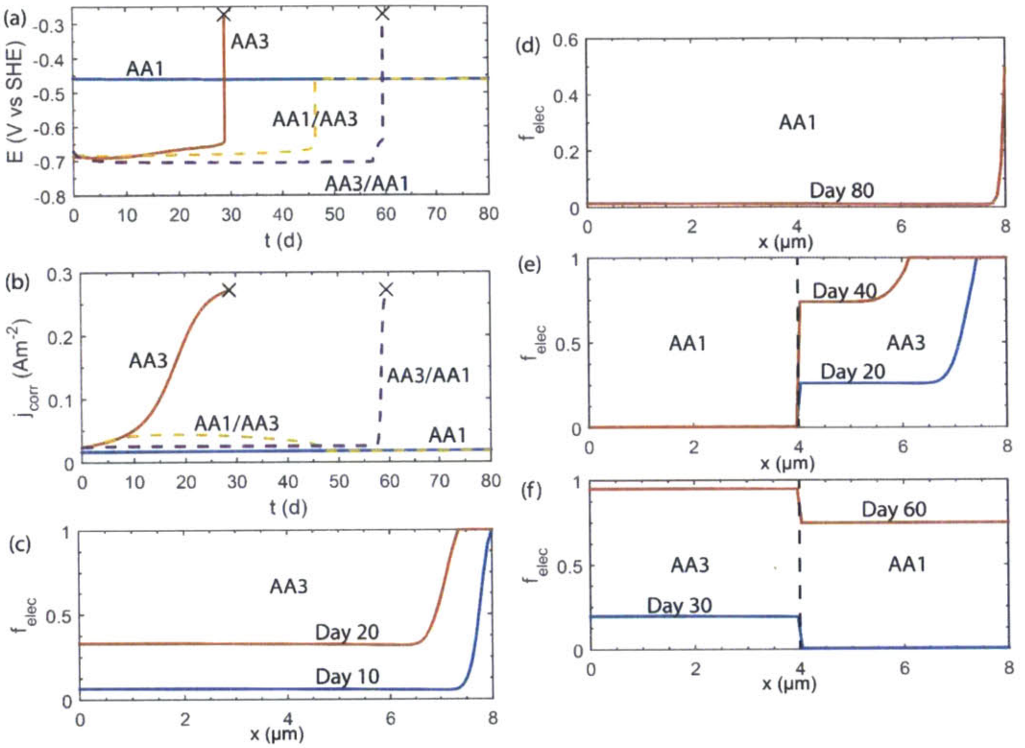

Figure 5.5 Corrosion simulations for selected single layer and bilayer coatings immersed in 50 mM NaCl solution. The corrosion potential and corrosion current density for all four coatings are shown in (a) and (b), and electrolyte fractions at selected times for each coating are shown in (c-f).

5.4.5 Optimization of aluminum alloy multilayer coatings

While the bilayer coatings described in Section 5.4.4 provide significantly improved performance relative to single layer coatings of equal thickness, there is no reason to expect that they represent the best possible multilayer coatings for protection of steel from the available materials. Thus, a simulated annealing algorithm similar to that described in Section 3.3.1 was applied, to generate coating structures that maximize the protection time in simulated immersion tests. Since the effectiveness of a corrosion coating at protecting steel is expected to decline precipitously with the loss of cathodic protection, the best estimate of the lifetime of the coatings is given by the simulated cathodic protection interval, for which the corrosion potential is maintained below -0.51 V vs SHE. The coating was considered to have a fixed thickness of 10 μm, which was divided into 20 layers of 0.5 μm each, so that a given design is described by a 20 element vector $\{x_1, x_2, \dots, x_{20}\}$, where each x_i takes the value of 1, 2, or 3 to correspond to AA1, AA2, or AA3, respectively. The simulated annealing algorithm was implemented according to the following steps:

1. Perform corrosion simulation on parent design X_p to calculate protection time t_p.
2. Mutate parent design by randomly selecting $\{i, j\} \in \{1, \ldots, 20\}$ such that $|i - j| \leq 5$. Generate candidate design X_c by changing layers i through j of the parent design X_p to a randomly selected different material.
3. Calculate protection time t_c for candidate design X_c.
4. Candidate replaces the parent for the next iteration with probability $\exp\left(\frac{t_\mathrm{c} - t_\mathrm{p}}{T}\right)$

where T is a temperature parameter that decreases with each iteration.

The optimization runs shown in this section were performed on a slightly older version of the model, which included an additional cathodic current density of 5×10^{-2}A/m^2 to simulate a situation in which the coating is required to provide a small amount of cathodic protection to nearby exposed substrate. While this does not significantly affect the ranking of different coatings or the design features of the optimized solutions, it does decrease the predicted coating lifetimes relative to those shown in the rest of this chapter. Figure 5.6 (a) shows the typical results of an optimization run, over 150 iterations. The solid line shows the value of the current parent design, while the dashed line shows the value of the tested candidates. The effect of the annealing is visible in the value of the parent design; over the first 50 iterations, a number of candidates are accepted that decrease the calculated protection time, and subsequently the algorithm becomes increasingly greedy as it converges toward a local optimum.

The optimized designs shown in Figure 5.6 (b-d) are based on two different conditions. The design OPT1 in Figure 5.6 (b) is the result of an optimization run for which the available materials are restricted to AA2 and AA3, both of which are possible to deposit from the same electrodeposition bath. Single bath electrodeposition is highly advantageous for reducing the cost of processing, and decreasing the chance of introducing inter-layer defects during bath changes, and so this optimization was intended to determine the best coating structure possible while retaining those advantages. The optimized structure appears to combine the beneficial effects of both of the bilayers described in Section 5.2.5; the outer barrier layer of AA2 decreases the initial corrosion rate, by preventing penetration of dissolved O_2 into the interior of the coating, until the onset of mechanical failure due to AA3 dissolution. At that point, the inner AA2 barrier similarly increases the lifespan of the remaining AA3 layer by preventing O_2 diffusion to the cathodically active steel surface.

For the optimized designs shown in Figure 5.6 (c-d), on the other hand, all three materials were permitted for use, and so the predicted lifetimes are significantly higher. The two designs represent the solutions of five different optimization runs; three of the runs converged to a design very similar to the three layer design of Figure 5.6 (c), while two converged to a design very similar to the four layer design of Figure 5.6 (d). While the design in Figure 5.6 (d) was scored slightly higher by the model, both designs are shown here as they represent substantially different strategies for multilayer coating design. The design OPT2 in Figure 5.6 (c) consists of three layers, with each layer more active than the one below it. As a result, the benefits of the design are similar to those for the AA1/AA3 bilayer described in Section 5.4.4. However, additional improvements are realized for the OPT2 design due to the thinner roughened surface layer at many parts of the corrosion process, as well as the partial conversion of the AA1 barrier to AA2, which is able to provide cathodic protection to the steel. The design OPT3 in Figure 5.6 (d), on the other hand, represents a combination of the strategies used in OPT1 and OPT2; the thick AA2 and AA3 layers cause the coating to dissolve in a top-down fashion, minimizing the available surface area and O_2 penetration to the steel, while the two separate AA1 layers decrease the corrosion rate of the AA2 layer in the same way as occurred the sandwich shaped OPT1 design. Overall, the results of the optimizations show that this modeling and optimization approach can discover non-obvious solutions with improved properties, that attempt to increase the protection time of the coating according to a variety of strategies.

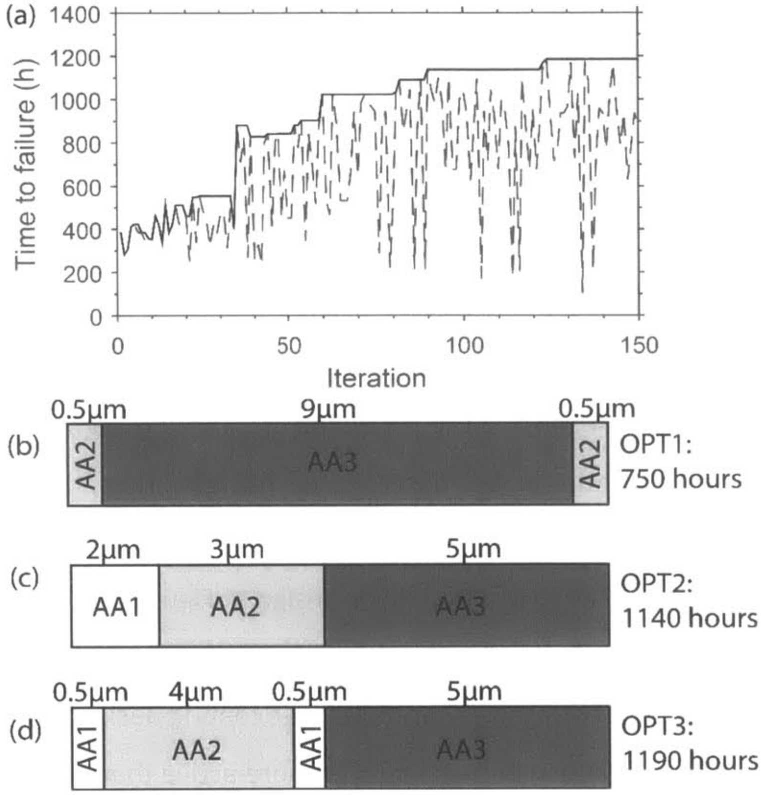

Figure 5.6 (a) Improvement in protection time over typical optimization run. Dashed line show values for tested candidates, while solid line shows value of parent design. (b) Optimized single bath design (AA2 and AA3 only). (c-d) Optimized dual bath designs (all materials).

5.5 Experimental validation of model predictions

5.5.5 Case Study 1: film thickness effect

It has been reported by several authors studying pitting corrosion of thin films that the pitting potential decreases with increasing film thickness and becomes closer to the repassivation potential, an effect generally attributed to the greater ease of forming persistent concentration gradients in thicker coatings [40,41]. Such behavior is intuitively reasonable, but cannot be captured by deterministic corrosion modeling that does not account for defects in the coating in some way; we are not aware of any theoretical elaboration of this effect in prior work, but our mean field model is intended to capture this kind of length-scale dependence of corrosion. In the present study, we studied the film thickness effect via potentiodynamic curves taken on AA1 electrodeposits with nominal thicknesses ranging from 0.5 to 25 μm. Although there was some variability between samples, in particular in the measured corrosion potential, there is a clear trend toward lower corrosion and pitting potentials with increasing film thickness. This is illustrated by representative polarization curves for 1 and 10 μm thick deposits in Fig. 5.7 (a). A compilation of corrosion and pitting potentials measured on seven different film thicknesses is assembled in Fig. 5.7 (c).

In order to evaluate the ability of the model to reproduce this phenomenon, simulated polarization curves were generated for Al-Zr films with thicknesses ranging from 0.1 to 100 μm, with a fixed porosity of 0.01. Increasing the thickness of the film was found to decrease the predicted corrosion and pitting potentials, as well as slightly increase the dissolution rate at high anodic polarizations; the simulated polarization curves for the 1 μm and 10 μm films, shown in Fig. 5.7 (b), are representative of this behavior. Although the difference in corrosion potential is much larger for the experimental polarization curves, the simulated curves are qualitatively similar, and, critically, capture a length-scale dependence that is intrinsically related to localized corrosion, without the need to simulate individual pits.

Fig. 5.7 (c) shows a quantitative comparison between experimental measurements and model predictions for pitting and corrosion potential, over the full range of tested film thicknesses, where the pitting potential is defined at the potential that produces a net anodic current of 1 Am^{-2}. The points in Fig. 5.7 (c) represent the average of experimentally measured values of E_{corr} and E_{pit} for two deposits at each thickness, while the dashed lines show the values predicted by the model.

First turning our attention to the pitting potentials, we observe quite good agreement between the experiments and the model, including two apparent regimes: a slow decrease in pitting potential for films of less than 5 μm, and a significantly faster exponential decrease with film thickness for thicker films. The first regime corresponds to films that are not thick enough to support significant concentration gradients; thus the predicted corrosion and pitting potentials remain close to the values in the bulk electrolyte. The second regime corresponds to films thick enough to support a concentrated electrolyte in the film interior as pits develop, which in turn allows persistent active dissolution to occur at lower overpotentials. This behavior corresponds well with reports showing that there is a threshold for stable pitting in aluminum at thicknesses in the range of 1-10 µm; pits that 1 µm or smaller tend to display metastable behavior and spontaneously repassivate, while pits 10 µm or larger contain sufficiently concentrated electrolyte in their interior for stable propagation even in the absence of applied potential [10].

The measured corrosion potentials in Fig. 5.7 (c) also show a clear decreasing trend with increasing film thickness, in reasonable agreement with the model prediction. The experimental corrosion potentials, however, were found to exhibit significantly more scatter and hysteresis than the pitting potentials. This may be due to the higher sensitivity of the corrosion potential on defects and surface condition; both anodic and cathodic polarization were found to generally result in a temporary decrease of 50 mV or more in the open circuit potential, presumably due to the presence of residual active anodic sites, while the measured pitting potential was generally found to be consistent to within 10-20 mV between duplicate samples or multiple scans on the same sample. In spite of the increased error, it is encouraging that the model captures the basic trend of the data, with reasonable quantitative agreement over most of the range of the experiments.

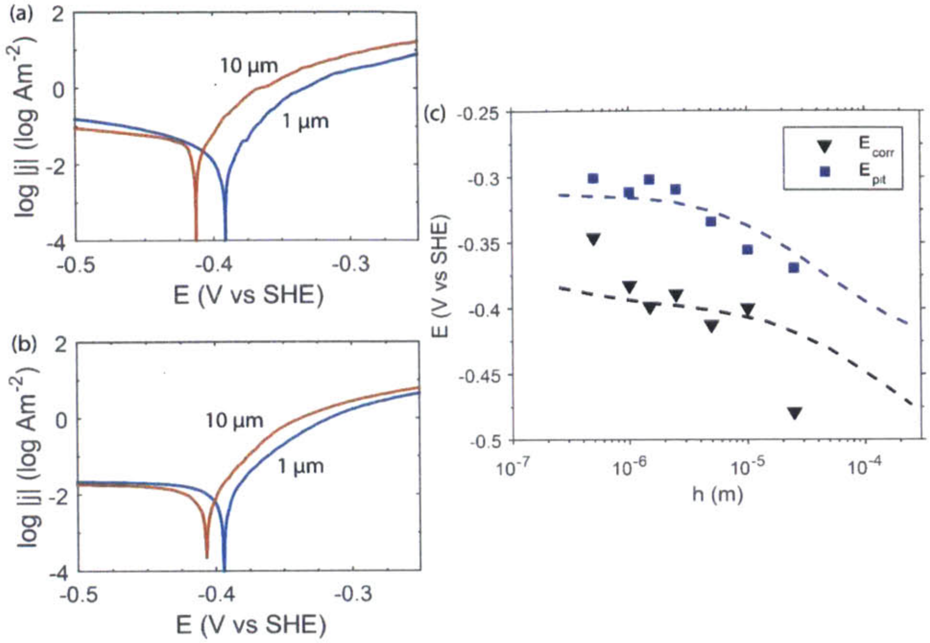

Figure 5.7 (a) Experimental polarization curves for AA1 films of different thicknesses. (b) Simulated polarization curves for AA1 films. (c) Corrosion and pitting potentials over a wide range of thicknesses. Dashed lines show model predictions.

5.5.2 Case Study 2: dissolution through a barrier

It has been widely observed in experiments that thin films provide imperfect barrier protection to underlying materials, due to the inevitable presence of pores and other defects. This is evidenced by the common finding that the corrosion potential of a substrate/coating pair or a multilayer coating tends to be closest to the material with the lowest corrosion potential of the individual materials, regardless of its position in the stack [19,21]. In the case where a more active material is occluded from the electrolyte by a layer of more noble material, the addition of the barrier typically does not significantly change the onset potential for the metal dissolution reaction, but instead limits the overall dissolution rate at higher anodic polarization due to mass transport limitations imposed by the barrier [21]. These phenomena are additional examples where conventional continuum corrosion modeling cannot be applied, and an important test case for the proposed effective medium modeling approach.

The solid black lines in Fig. 5.8 (a) show an experimental cyclic voltammogram (CV) for a two-layer electrodeposit, consisting of an AA3 layer deposited to 15 Ccm^{-2} beneath an AA1 barrier layer deposited to 15 Ccm^{-2}, taken at a scan rate of 1.667 mVs^{-1}. The dotted colored lines in Fig. 5.8 (a) show the experimental polarization curves for single layer AA1 and AA3 electrodeposits for comparison. On the first anodic scan, the corrosion potential is -0.61 V vs SHE, which is much closer to the potential of -0.68 V vs SHE measured for the AA3 underlayer than the potential of -0.39 V vs SHE for the AA1 barrier; even in the as-deposited condition, the corrosion potential is largely controlled by the dissolution of the active AA3 layer, apparently through pores and defects in the barrier. However, additional anodic polarization up to a potential of approximately -0.3 V vs SHE generates dramatically decreased current density for the bilayer coating relative to the AA3 single layer, suggesting that addition of the AA1 barrier does significantly limit the dissolution rate of the AA3 layer beneath, presumably due to mass transport limitations.

The apparent dominance of the underlayer is temporary; as the applied potential passes -0.3 V, marked by the point 1 in Fig. 5.8 (a), the anodic current density begins to increase rapidly, and closely resembles the polarization curve for the AA1 outer layer. This shift may be attributed to the onset of AA1 dissolution, which can proceed at the full expected rate since the AA1 layer is not subject to any mass transport restriction other than that imposed by the electrolyte diffusion layer. The effect of the AA1 dissolution is clearly evident on the returning cathodic scan; even as the potential is decreased below the pitting potential for the AA1 layer, the anodic current density is dramatically higher than it was on the forward scan, and much more closely resembles the curve for the AA3 layer, indicating that the corrosion damage to the AA1 layer during the anodic polarization substantially degraded its ability to act as a diffusion barrier. As the potential is decreased to the pitting potential of the AA3 underlayer, indicated by the point 2 in Fig. 5.8 (a), there is a second elbow visible in the polarization curve. The change of slope at this point suggests that the below this potential, new pits can no longer be initiated in the AA3 layer; instead anodic current observed below this point is likely due to residual activity in pits initiated during the anodic polarization.

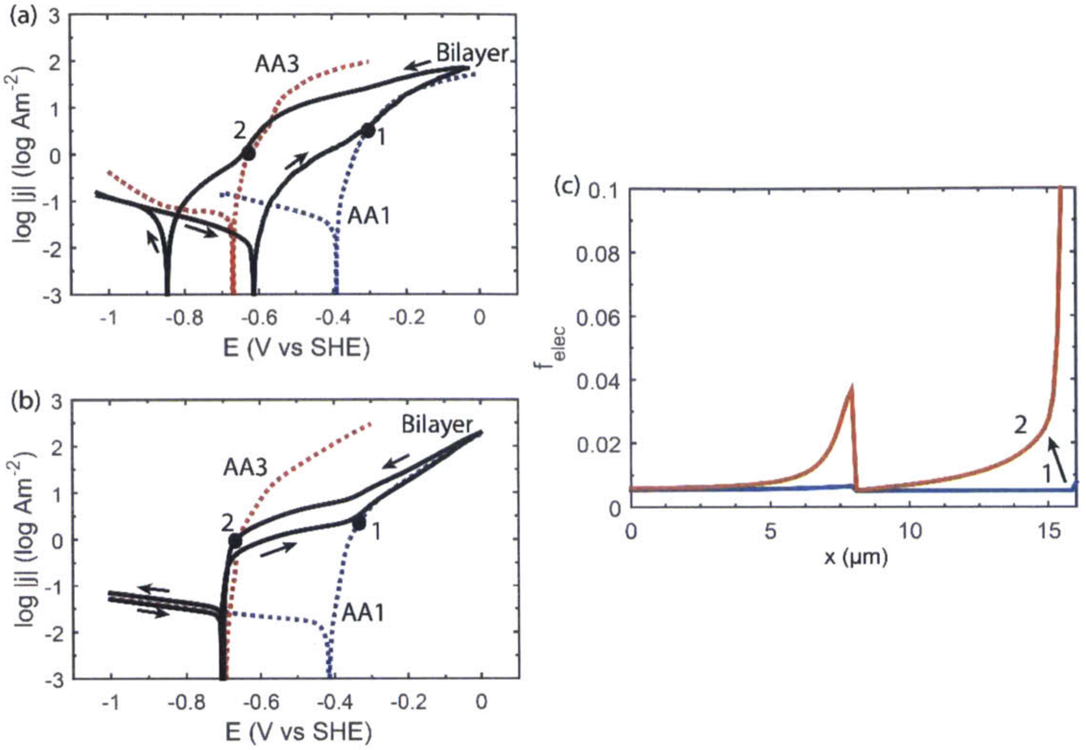

Figure 5.8 (a) Experimental CV for AA3/AA1 bilayer. (b) Simulated CV for AA3/AA1 bilayer. (c) Calculated f_{elec} distributions corresponding to points 1 and 2 in (b).

To evaluate the ability of the model to simulate the behavior observed in this experiment, a simulated cyclic voltammogram was calculated for the same nominal bilayer geometry consisting of 4 μm AA3 beneath 4 μm AA1. This simulation continuously updated the electrolyte fraction f_{elec} throughout the depth of the bilayer according to the Faraday equation Eq. (5.22), starting from an assumed constant value of $f_{\text{elec}} = 0.005$. To match the experimental conditions as closely as possible, the potential applied to the modeled bilayer was swept from -1 to 0 V vs SHE and back, at a scan rate of 1.667 mVs^{-1}.

The simulated CV for the bilayer is shown in Fig. 5.8 (b), along with simulated anodic polarization curves for single layer AA1 and AA3 films, which were calibrated to the same set of curves from the experiments in Fig. 5.8 (a). In agreement with the experimental curve in Fig. 5.8 (a), on the anodic scan the simulated CV has a corrosion potential quite close to the AA3 underlayer, combined with a significantly decreased anodic current density at moderate anodic polarization in the potential range -0.6 to -0.4 V VS SHE. This illustrates how critical it is to model such systems with electrolyte access to the underlayer even at extremely low nominal defect contents, and also captures the beneficial effect of a protective overlayer to slow the corrosion of exposed underlayer. The simulated CV also properly exhibits a rapid increase in corrosion rate coinciding with the onset of AA1 dissolution starting at -0.35 V vs SHE, labeled as point 1 in Fig. 5.8 (b), closely matching the curve for AA1 for higher potentials. Finally, the simulated CV also correctly exhibits a higher anodic current density on the returning cathodic scan due to damage to the AA1 barrier, though the increase is less dramatic than observed in the experiment.

Although the simulated CV shows good qualitative agreement with the experiment, there are a few notable discrepancies as well. On the initial anodic scan, the simulated corrosion potential is almost identical to that of the AA3 underlayer, while in the experiment the initial corrosion potential is approximately 60 mV higher than the AA3 single layer, suggesting that the model may somewhat overestimate the penetration of corrosion through the intact, as-deposited barrier layer. This difference may be traceable to the lack of a pitting initiation mechanism in the model; essentially by starting with a finite positive value for f_{elec} the model assumes that some degree of pitting initiation has already taken place.

A second deviation between the model prediction and the experiment can be seen in the cathodic curve, for which the model predicts a much smaller increase in current density than observed in the experiment. This discrepancy may be attributed to the predicted distribution of AA1 loss during the scan, as can be seen from the simulated distributions of f_{elec} in Fig. 5.8 (c), corresponding to the points 1 and 2 in Fig. 5.8 (b). Due to the very high expected current densities, and the limited rate of mass transport predicted by the model from the interior of the intact coating, the majority of predicted AA1 loss occurs from the very outer layer of the coating, and so at point 2, the value of f_{elec} at the base of the AA1 layer is almost unchanged from the initial value, resulting in a significant barrier for Al ion diffusion away from the AA3 layer. In fact, the damage to the AA1 layer during the experiment was due to formation of discrete through-going pits, which are significantly more effective at permitting mass transport through the barrier for an equivalent quantity of material loss. This discrepancy reflects a limitation to a fundamental assumption behind the model, which is that the effective diffusivity within the porous coating is solely dependent on the average porosity, while in reality larger corrosion pits formed under conditions of high anodic polarization are very likely to be more permissive of diffusion than a tortuous network of fine pores slowly formed under low anodic polarization [42]. This difference suggests that a more sophisticated approximation, which more explicitly incorporates the initiation and formation of corrosion pits, may be necessary to obtain good quantitative agreement under conditions of high anodic polarization.

Finally, the simulated CV predicts a very rapid cessation of anodic activity once the potential drops below the point 2 on the cathodic scan, while the experiment shows that a significant amount of residual activity remains, as was the case for the single layer CVs. The residual activity observed experimentally is likely due to the concentrated environment and precipitated aluminum salts within the interior of the coating [10], which is not accounted for by the model, which neglects corrosion product precipitation and solves for a steady state concentration distribution at each point. Thus the model does not account for the temporary persistence of concentration gradients formed at a higher potential, and does not capture this type of hysteresis.

Despite these discrepancies, overall the good qualitative agreement between the simulated and experimental CVs suggest that this modeling approach is able to provide a very reasonable approximation of the polarization response of a multilayer coating that can incorporate changes in geometry due to corrosion damage. It should be noted that the formulation of the model is not truly designed to account for the rapidly changing conditions involved in a CV measurement, or the different corrosion morphologies expected at very high anodic polarization. In general we expect that the fundamental assumptions of a uniformly porous structure, and electrolyte composition reasonably close to a steady state condition, will be much more appropriate under the slowly changing open-circuit or low polarization conditions representative of corrosion conditions in the field.

5.5.3 Case Study 3: Free corrosion

While the corrosion simulations generated by this model, such as were presented in Section 5.4, are not expected to produce quantitatively accurate predictions of coating lifetime, especially considering the importance of corrosion products in determining long term corrosion rates, it is hoped that the simulated coating lifetimes may be useful for ranking different coating designs, and as such have applicability as a design tool for development of multilayer corrosion coatings. In lieu of a detailed theoretical or empirical model of the effect of corrosion products, such a ranking is based on the general assumption that the overall effect of the corrosion products will be similar for all of the materials being compared, and so relative performance will be determined largely by geometric factors captured by the model.

In order to evaluate the protective ability of a wide range of coating configurations, immersion corrosion tests in naturally aerated 50 mM NaCl solution were performed on single layers of AA1, AA2, AA3, as well as six naïve multilayer coatings, consisting of two or four alternating layers of equal thickness, and the two optimized coatings OPT1 and OPT2 described in Section 5.4.5. All coatings were deposited to a total charge density of 30 Ccm^{-2}, for a nominal thickness of approximately 8 μm. For the immersion tests, each sample was immersed in a separate container with 200 mL electrolyte, and with the corrosion potential measured manually every 24 hours using a high-impedance voltmeter (Fluke) relative to a SSCE reference electrode. At 48 hour intervals, each sample was gently dipped in DI water for 10 seconds to remove excess corrosion products, and then reimmersed in freshly mixed electrolyte. Coating failure was evaluated according to two criteria. The first criterion is the cathodic protection time, calculated as the number of days for which the measured corrosion potential remained below -0.51 V vs SHE. This cutoff value was selected to provide 100 mV of cathodic polarization, relative to the measured corrosion potential of -0.41 V vs SHE for the bare steel substrate. The second criterion is the time to the emergence of visible red rust on 5% of the surface of the coating. In all cases, red rust was found to be fully suppressed throughout the cathodic protection interval, and so coating failure times were longer when evaluated according to the red rust criterion. A summary of the tested coatings, along with the predicted and observed protection times, is included in Table 5.4.

Table 5.4 List of electrodeposits used for immersion testing in 50 mM NaCl. Columns labeled t_{CP} refer to the cathodic protection time, while t_{RR} refers to the time until visible red rust on 5% of the coating surface.

Coating	E_{corr} (V vs SHE)	$t_{\mathrm{CP,experiment}}$ (days)	$t_{\mathrm{RR,experiment}}$ (days)	$t_{\mathrm{CP,model}}$ (days)
AA1	-0.396 V	0	2	0
AA2	-0.611 V	43	75	32
AA3	-0.582 V	36	37	29
AA1/AA3	-0.585 V	51	68	46
AA3/AA1	-0.568 V	56	65	59
AA2/AA3	-0.614 V	64	86	62
AA3/AA2	-0.617 V	65	73	59
AA2/AA3/AA2/AA3	-0.669 V	69	89	61
AA3/AA2/AA3/AA2	-0.631 V	51	59	53
OPT1	-0.623 V	68	74	100
OPT2	-0.571 V	45	90	89
Bare steel	-0.410 V	N/A	1 d	N/A

The measured corrosion potentials for the AA1 and AA3 single layers, and AA1/AA3, and AA3/AA1 bilayer coatings, are shown in Figure 5.9 (a), while images of the coatings at various points in the corrosion process are shown in Figure 5.9 (b-e). The four coatings shown in Figure 5.9 correspond to the simulated coatings described in Section 5.4.4, so that the experimental observations may be compared directly to the simulation results in Figure 5.5. The AA1 single layer had an initial corrosion potential of -0.40 V vs SHE, rising to a steady value of -0.38 V vs SHE over several days. As this is higher than the corrosion potential of bare steel, the AA1 coating is not expected to provide any cathodic protection to any exposed steel. Accordingly, small spots of visible red rust were observed to form on the surface of the coating after only 24 hours, spreading slowly with time, particularly around the edges and in areas where the coating had experienced visible damage, as can be seen in the images of the corroded coatings in Figure 5.9 (b).

The AA3 single layer, conversely, had a corrosion potential of -0.61 V vs SHE after 24 hours, rising slowly to -0.51 V vs SHE over 36 days, and so would be expected to provide effective cathodic protection during that entire interval. During this period, the corrosion damage to the AA3 layer was visibly inhomogeneous, as can be seen in the pictures of the corroded coating in Figure 5.9 (c); after 20 days, for instance, the coating had significantly receded from the edges of the sample, and the remaining coating exhibited a highly uneven distribution of corrosion products and surface appearance. This suggests that the corrosion of the coating proceeded in a highly localized manner, which tended to magnify the effect of small initial variations in corrosion susceptibility. Following the loss of cathodic protection on day 36, the potential rose abruptly to -0.36 V vs SHE over a single day, coinciding with rapid formation of red rust. Comparison of the corroded AA1 and AA3 single layer coatings in Figure 5.9 (b-c) illustrates the relative effects of barrier and cathodic protection. While the AA1 coating did not delay the initial formation of red rust, the intact barrier did significantly slow the overall corrosion rate, to a sufficient extent that the total area of red rust after 30 days was only slightly greater than that of the AA3 coating 3 days following the loss of cathodic protection.

The measured corrosion potentials for the AA1/AA3 and AA3/AA1 bilayer coatings in Figure 5.9 (a) both followed a similar progression to that of the AA3 single layer, with the measured period of cathodic protection significantly extended to 51 and 56 days, an increase of 38 and 51 percent, respectively. In both cases, the bilayers initially showed close visual resemblance to the single layer coatings forming their outer layers. The AA1/AA3 bilayer was rapidly covered with a mixture of dark and light gray corrosion products, while the AA3/AA1 bilayer was initially nearly white, with light gray patches slowly appearing and spreading across the surface over time, as can be seen in images of the corroded coatings in Figure 5.9 (d-e). However, the corrosion damage on the surface of the AA1/AA3 bilayer was nearly uniform in appearance, with the exception of a small area of AA1 visible where the AA3 layer had receded from the edges of the sample. The behavior of the two bilayers diverged dramatically as cathodic protection was lost, starting around day 50. In the case of the AA1/AA3 bilayer, the surface appearance did not change dramatically following the loss of cathodic protection, with a highly adherent film of corrosion products from the AA3 layer present over most of the surface. Red rust was observed to form slowly and uniformly across the surface starting on day 68, representing a delay of 17 days following the loss of cathodic protection. For the AA3/AA1 bilayer, on the other hand, the loss of cathodic protection coincided with dramatic mechanical failure of the AA1 barrier layer, resulting in the cracks and flaking visible in Figure 5.9 (e). Red rust was observed forming on day 65, a delay of 9 days following the loss of cathodic protection.

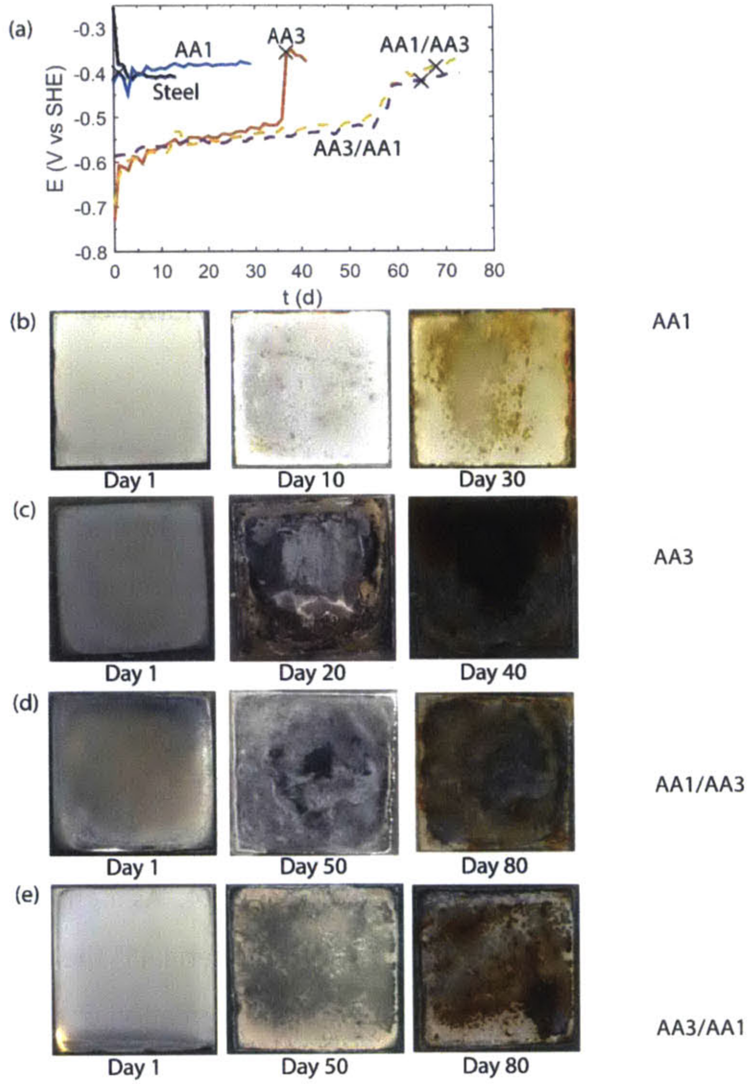

Figure 5.9 (a) Corrosion potentials for AA1, AA3, AA1/AA3, and AA3/AA1 coatings in 50 mM NaCl immersion. (b-e): Images of corroded coatings.

The experimental corrosion tests exhibit two significant quantitative deviations from the simulations. First, the measured corrosion potentials of the AA3 and bilayer coatings were found to be approximately 100 mV higher than the predicted value after 24 hours, and showed a greater increase over time prior to failure than the simulated coatings. One possible source of this discrepancy is changes in composition over time, due to dealloying and depletion of favorable sites for corrosion pit initiation. Experimental studies of Al-Zn alloy corrosion have shown that typically Zn is preferentially depleted over time, resulting in a decrease in anodic activity and corresponding increase in the corrosion potential [129]. Another possible explanation for the higher corrosion potentials is the role of precipitated corrosion products, which decrease the rates of both the anodic and cathodic reactions, and are vitally important in determining the service lifetime of corrosion coatings. The effect of corrosion products is included only in the reduced rate of oxygen reduction used by the model, relative to the cathodic currents measured in polarization curves; as a result the model neglects the effects of corrosion products on decreasing anodic activity, and predicts lower corrosion potentials than would be expected experimentally.

5.5.4 Prediction of coating lifetime

The comparison between the corrosion simulations and the immersion experiments in 5.5.3 suggests that despite the quantitative differences between model predictions and the observed corrosion potentials, the model is reasonably successful at capturing the relative corrosion behavior of different coating configurations, in particular the dramatic increase in performance due to composite coating structures.

A direct comparison between the predicted and measured coating lifetimes is presented in Figure 5.10, for the full set of coatings presented in Table 5.4. As mentioned in Section 5.5.3, the failure of each coating was assessed according to two criteria: (1) the loss of cathodic protection marked by $E_{\mathrm{corr}} > -0.51$ V vs SHE, and (2) the formation of red rust on 1% of the visible surface. The corrosion simulations, however, do not provide a way to distinguish between these two criteria, due to the lack of a way to estimate the effectiveness of the residual protection afforded by the remaining barrier layers and precipitated corrosion products. Therefore, the duration of cathodic protection is used as the coating lifetime predicted by the simulation, and compared to the measured cathodic protection interval in Figure 5.10 (a), and the time to red rust in Figure 5.10 (b).

Based on the results shown in Figure 5.10, it may be inferred that, all else equal, multilayer coatings generally have superior performance relative to single layer coatings of equal thickness. For instance, all of the tested multilayer coatings surpassed all of the monolithic coatings on measured cathodic protection time. The relative effectiveness at delaying the formation of red rust, on the other hand, was somewhat more mixed, with the most successful single layer coating, consisting of material AA2, performing comparably with the multilayer coatings as a group, and was the only coating to dramatically outperform the model prediction for time to red rust. It should be noted, however, that the material AA2 contained a significant nanocrystalline phase fraction, based on the results from Chapter 2, which may be partially responsible for the unexpectedly good performance.

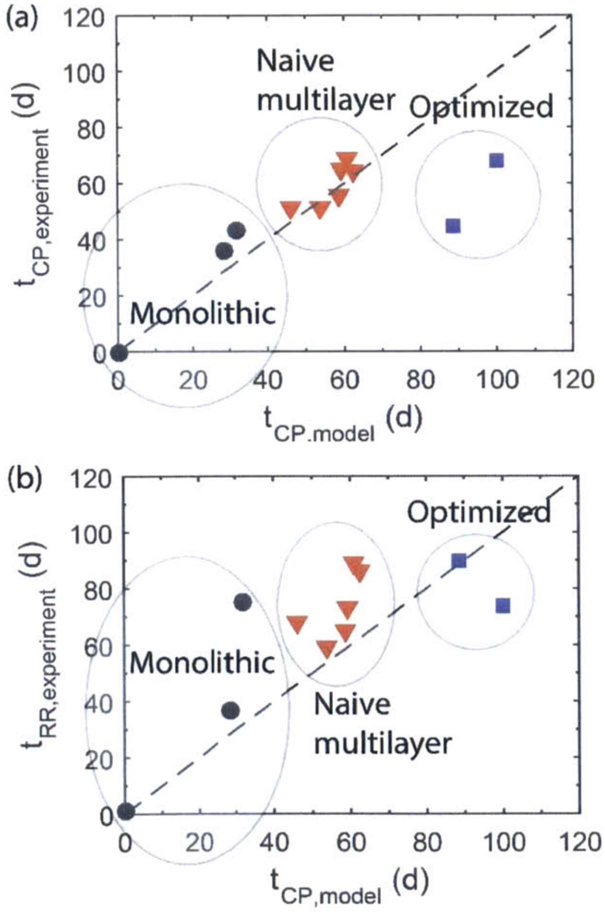

Figure 5.10 (a) Comparison between model prediction and measured cathodic protection interval. (b) Comparison between model prediction and time to red rust.

5.6 Conclusion

In this chapter, we present an effective medium approach to modeling localized corrosion. The proposed model treats the corroding material as a porous electrode with a continuously updated gradient of porosity, and adjusts the diffusion rates of dissolved ions accordingly using an effective medium approximation. Despite the simplicity of several of the approximations used in this model, it is successful at reproducing several phenomena that are particularly relevant to corrosion of multilayer thin films, including the effect of variation in film thickness on the pitting potential, and the undercutting corrosion of an active metal dissolving beneath a porous barrier layer. In addition, the model is able to generate time-dependent corrosion simulations, and shows good qualitative agreement with the comparative corrosion behavior of different coating configurations tested experimentally.

A principal objective for the modeling approach presented here is to demonstrate that a relatively simple 1-D model can produce useful predictions about the corrosion behavior of single and multilayer thin films, in a computationally tractable manner and without requiring extensive quantitative knowledge of the microstructure or corrosion mechanisms involved. One advantage of this approach is that it can be used to quickly calculate polarization curves for multilayer thin films, adjusted for varying degrees of corrosion damage. Standard finite element models of galvanic corrosion on 2-D or 3-D domains assume that the electrode behavior is the same as that of the bulk material consisting of the outermost material [3,8], and are thus difficult to apply to composite materials such as multilayer thin films, in which underlying materials present a meaningful contribution to the corrosion behavior. By generating straightforward and reasonable estimates of the polarization response of composite materials, the output of the 1-D effective medium model proposed here may allow application of galvanic corrosion models to a much wider range of materials. In particular, this modeling approach may be useful as a design tool for development of multilayer corrosion coatings, due to the ability to efficiently rank different coatings based on desired corrosion properties.

6. Conclusion

This thesis seeks to apply computational modeling techniques to the problem of simulating corrosion of multilayer corrosion coatings, with the ultimate goal of prediction of lifetimes for multilayer corrosion coatings under immersion conditions, and computational design of multilayer coatings with improved properties. To this end, the work presented in this thesis focuses on several areas, broadly split into (1) experimental work on electrodeposition of multilayer aluminum-zinc alloy coatings, (2) development of a 2-D time-dependent computational modeling of galvanic corrosion of multilayer coatings, and (3) development of a 1-D computational model of localized corrosion of multilayer coatings, using an effective medium approximation to model the porous electrode. The work done in each of these areas is described below in more detail.

6.1 Electrodeposition of aluminum-zinc alloy multilayer coatings

Aluminum-zinc alloys were selected as ideal candidates for use in multilayer corrosion coatings for protection of steel due to a number of factors, including low cost, good corrosion resistance, and ability to provide cathodic protection to steel. In addition, aluminum-zinc alloys can be efficiently from electrodeposited from a room temperature ionic liquid bath, with composition continuously modulated by variation in deposition current density. However, significant work was required to generate aluminum-zinc multilayers with good enough properties for practical use. In particular, binary aluminum-zinc electrodeposits show a very strong tendency for phase decomposition into an aluminum-rich matrix and zinc dendrite microstructure, resulting in significant degradation in mechanical properties and corrosion resistance, as well as making it difficult to produce distinct layers without through-going defects.

However, as described in Chapter 2, dramatic improvement in the properties of the aluminum-zinc coatings was produced by ternary alloying with the addition of Zr, which had been previously recognized as a grain-refining element for other aluminum alloys. The addition of Zr was found to significantly decrease the surface roughness and increase the compositional homogeneity and corrosion resistance of the electrodeposits, allowing acceptable coatings to be produced over a much wider range of composition. In addition, the addition of Zr was associated with the emergence of a nanocrystalline or amorphous phase in the high zinc coatings, resulting in a further increase in corrosion resistance relative to the coarse-grained Al-Zn-Zr deposits.

6.2 Computational model of galvanic corrosion

Chapter 3 of this thesis describes the development of a 2-D model of galvanic corrosion, as applied to a graded zinc-alloy coating on steel. In this model, steady state distributions of potential were calculated using the finite element method to solve field-based equations for charge and mass transport in the electrolyte; these steady state solutions were then used to calculate instantaneous metal dissolution rates, which were integrated over time to generate time-dependent corrosion simulations. The simulations indicated that a large potential improvement in lifetime for multilayer coatings can be realized by modest variation in coating properties between layers. This simulation tool was also coupled to a simulated annealing optimization algorithm to design coatings with maximized service lifetime. The predicted optimized coating consisted of a thin barrier layer and a thick sacrificial layer, increasing the delay before dissolution of the barrier exposes additional steel to the electrolyte.

The work presented in Chapter 4 describes an attempt to validate the output of the galvanic corrosion model on direct measurements of corrosion of pure zinc and aluminum coatings on steel in sulfuric acid solution. While the model was reasonably successful at capturing the qualitative differences between zinc and aluminum dissolution, it produced an imperfect quantitative description of the corrosion process. In particular, while distribution of metal loss in the zinc coating matched the model prediction quite well for the first 30 minutes, the zinc subsequently underwent a loss of surface reactivity and a shift to localized corrosion.

6.3 Computational model of localized corrosion

Chapter 5 of this thesis describes the development of 1-D model of localized corrosion of multilayer thin films, using an effective medium approximation to model the porous layers formed as corrosion damage occurs within the coating. The model uses a first-order approximation to capture the effect of electrolyte concentration within the interior of the coating, resulting in the active-passive behavior typical of pitting corrosion. The model was validated on experimental measurements of a number of phenomena specific to the localized corrosion of thin films, such as the effect of variation in film thickness, and the behavior of an active material dissolving through a more resistant barrier layer, and was shown to accurately reproduce the observed qualitative and quantitative trends. In addition, the 1-D model can be used to generate time-dependent corrosion simulations through integration of calculated steady-state metal dissolution rates. These corrosion simulations were shown have significant ability to predict the service life of different multilayer coating configurations in immersion conditions, though additional refinement is required to generate accurate quantitative predictions of the behavior, particularly in capturing the effects of precipitated corrosion products.

7. Directions for Future Work

The work presented in this thesis illustrates many of the limitations of preexisting computational models of corrosion, particularly as regards localized corrosion, and presents a novel approach to modeling localized corrosion of multilayer thin films using an effective medium approximation on a 1-D finite element domain. While the proposed modeling technique is successful at capturing a number of phenomena specific to corrosion of multilayer thin films, such as the effect of variation in length scales and dissolution through a barrier, there are a number of additional steps that can be taken to achieve good predictive ability in a quantitative sense. Of these, the following appear to be among the most promising for continuing model development and validation:

1. Corrosion products: Corrosion products are unquestionably critical to the long-term performance of corrosion coatings, particularly those with a high enough corrosion rate to provide meaningful cathodic protection. While the chemistry of corrosion products is very complex and not fully understood, a reasonable model could capture the approximate effects of corrosion products through a purely phenomenological approach, by for instance taking polarization curves or electrochemical impedance spectroscopy measurements over time on immersed samples over time.
2. Dealloying: In multiphase alloys, as more susceptible phases dissolve preferentially, the remaining material over time becomes increasingly corrosion resistant. This situation represents a promising area for application of an effective medium model, by expanding the local description to include fractions of multiple phases, as well as electrolyte. The approximations for local interfacial areas and effective mass transport rates are readily adaptable to inclusion of additional phases, and the phases initially present in the material can be calculated from XRD measurements in a straightforward way.
3. Multiscale modeling: The 1-D effective medium model described in Chapter 5 can be used to produce simulated polarization curves for multilayer coatings, which are adjusted based on degree of coating damage. Since such polarization curves represent the boundary conditions for 2-D galvanic corrosion models, such as described in

Chapters 3 and 4, the output from the 1-D model can be used to apply 2-D galvanic corrosion models to a much wider range of conditions.

4. Microscopic corrosion model: The 1-D effective medium model relies on a number of crude approximations for the relationship between local porosity and properties such as effective diffusion coefficients and specific surface area, where the effect of different microstructures is considered through the use of a single length parameter δ. A detailed microscopic model, which treats the porous coating in terms of an appropriate periodic or fractal microstructure, could produce significantly a more accurate and rigorous

References

[1] Z. Panossian, L. Mariaca, M. Morcillo, S. Flores, J. Rocha, J.J. Peña, et al., Steel cathodic protection afforded by zinc, aluminium and zinc/aluminium alloy coatings in the atmosphere, Surf. Coat. Technol. 190 (2005) 244–248. doi:10.1016/j.surfcoat.2004.04.023.

[2] L.A. Dobrzanski, K. Lukaszkowicz, A. Zarychta, L. Cunha, Corrosion resistance of multilayer coatings deposited by PVD techniques onto the brass substrate, J. Mater. Process. Technol. 164 (2005) 816–821. doi:10.1016/j.jmatprotec.2005.02.081.

[3] J. Fei, G.D. Wilcox, Electrodeposition of zinc–nickel compositionally modulated multilayer coatings and their corrosion behaviours, Surf. Coat. Technol. 200 (2006) 3533–3539. doi:10.1016/j.surfcoat.2004.08.183.

[4] W. Cai, C.A. Schuh, Tuning nanoscale grain size distribution in multilayered Al-Mn alloys, Scr. Mater. 66 (2012) 194–197. doi:10.1016/j.scriptamat.2011.10.040.

[5] K. Deshpande, Validated numerical modelling of galvanic corrosion for couples: Magnesium alloy (AE44)-mild steel and AE44-aluminium alloy (AA6063) in brine solution, Corros. Sci. 52 (2010) 3514–3522.

[6] C. Cai, Z. Zhang, F. Cao, Z. Gao, J. Zhang, C. Cao, Analysis of pitting corrosion behavior of pure Al in sodium chloride solution with the wavelet technique, J. Electroanal. Chem. 578 (2005) 143–150. doi:10.1016/j.jelechem.2004.12.032.

[7] M. Natesan, G. Venkatachari, N. Palaniswamy, Kinetics of atmospheric corrosion of mild steel, zinc, galvanized iron and aluminium at 10 exposure stations in India, Corros. Sci. 48 (2006) 3584–3608. doi:10.1016/j.corsci.2006.02.006.

[8] A.P. Yadav, H. Katayama, K. Noda, H. Masuda, A. Nishikata, T. Tsuru, Effect of Al on the galvanic ability of Zn–Al coating under thin layer of electrolyte, Electrochimica Acta. 52 (2007) 2411–2422. doi:10.1016/j.electacta.2006.08.050.

[9] A.E. Ares, L.M. Gassa, Corrosion susceptibility of Zn-Al alloys with different grains and dendritic microstructures in Nacl solutions, Corros. Sci. 59 (2012) 290–306. doi:10.1016/j.corsci.2012.03.015.

[10] S.J. Bull, A.M. Jones, Multilayer coatings for improved performance, Surf. Coat. Technol. 78 (1996) 173–184. doi:10.1016/0257-8972(94)02407-3.

[11] M. Bromark, M. Larsson, P. Hedenqvist, S. Hogmark, Wear of PVD Ti/TiN multilayer coatings, Surf. Coat. Technol. 90 (1997) 217–223. doi:10.1016/S0257-8972(96)03141-6.

[12] C. Charrier, P. Jacquot, E. Denisse, J.P. Millet, H. Mazille, Aluminium and Ti/Al multilayer PVD coatings for enhanced corrosion resistance, Surf. Coat. Technol. 90 (1997) 29–34. doi:10.1016/S0257-8972(96)03080-0.

[13] V.K.W. Grips, H.C. Barshilia, V.E. Selvi, Kalavati, K.S. Rajam, Electrochemical behavior of single layer CrN, TiN, TiAlN coatings and nanolayered TiAlN/CrN multilayer coatings prepared by reactive direct current magnetron sputtering, Thin Solid Films. 514 (2006) 204–211. doi:10.1016/j.tsf.2006.03.008.

[14] G. Wu, Fabrication of Al and Al/Ti coatings on magnesium alloy by sputtering, Mater. Lett. 61 (2007) 3815–3817. doi:10.1016/j.matlet.2006.12.082.

[15] A. Korhonen, Corrosion of Thin Hard Pvd Coatings, Vacuum. 45 (1994) 1031–1034. doi:10.1016/0042-207X(94)90015-9.

[16] C. Nee, W. Kim, R. Weil, Pulsed Electrodeposition of Ni-Mo Alloys, J. Electrochem. Soc. 135 (1988) 1100–1103. doi:10.1149/1.2095883.

[17] J.D. Jensen, D.R. Gabe, G.D. Wilcox, The practical realisation of zinc–iron CMA coatings, Surf. Coat. Technol. 105 (1998) 240–250. doi:10.1016/S0257-8972(98)00461-7.

[18] I. Kirilova, I. Ivanov, Corrosion behaviour of Zn–Co compositionally modulated multilayers electrodeposited from single and dual baths, J. Appl. Electrochem. 29 (1999) 1133–1137. doi:10.1023/A:1003675216529.

[19] K.S.R. Krishnan, K. Srinivasan, S. Mohan, Electrodeposition of compositionally modulated alloys - An overview, Trans. Inst. Met. Finish. 80 (2002) 46–48.

[20] I. Ivanov, I. Kirilova, Corrosion resistance of compositionally modulated multilayered Zn–Ni alloys deposited from a single bath, J. Appl. Electrochem. 33 (2003) 239–244. doi:10.1023/A:1024179032045.

[21] P. Ganesan, S.P. Kumaraguru, B.N. Popov, Development of compositionally modulated multilayer Zn-Ni deposits as replacement for cadmium, Surf. Coat. Technol. 201 (2007) 7896–7904. doi:10.1016/j.surfcoat.2007.03.033.

[22] A.J. Detor, C.A. Schuh, Tailoring and patterning the grain size of nanocrystalline alloys, Acta Mater. 55 (2007) 371–379. doi:10.1016/j.actamat.2006.08.032.

[23] A. Maciej, G. Nawrat, W. Simka, J. Piotrowski, Formation of compositionally modulated Zn–Ni alloy coatings on steel, Mater. Chem. Phys. 132 (2012) 1095–1102. doi:10.1016/j.matchemphys.2011.12.074.

[24] N. Boshkov, K. Petrov, G. Raichevski, Corrosion behavior and protective ability of multilayer Galvanic coatings of Zn and Zn–Mn alloys in sulfate containing medium, Surf. Coat. Technol. 200 (2006) 5995–6001. doi:10.1016/j.surfcoat.2005.10.002.

[25] M. Rahsepar, M.E. Bahrololoom, Corrosion study of Ni/Zn compositionally modulated multilayer coatings using electrochemical impedance spectroscopy, Corros. Sci. 51 (2009) 2537–2543. doi:10.1016/j.corsci.2009.06.030.

[26] M. Rahsepar, M.E. Bahrololoom, Study of surface roughness and corrosion performance of Ni/Zn-Fe and Zn-Fe/Ni compositionally modulated multilayer coatings, Surf. Coat. Technol. 204 (2009) 580–585. doi:10.1016/j.surfcoat.2009.08.036.

[27] M.R. Kalantary, G.D. Wilcox, D.R. Gabe, The production of compositionally modulated alloys by simulated high speed electrodeposition from a single solution, Electrochimica Acta. 40 (1995) 1609–1616.

[28] Y. Boonyongmaneerat, S. Saenapitak, K. Saengkiettiyut, Reverse pulse electrodeposition of Zn-Ni alloys from a chloride bath, J. Alloys Compd. 487 (2009) 479–482. doi:10.1016/j.jallcom.2009.07.163.

[29] N. Eliaz, K. Venkatakrishna, A.C. Hegde, Electroplating and characterization of Zn–Ni, Zn–Co and Zn–Ni–Co alloys, Surf. Coat. Technol. 205 (2010) 1969–1978. doi:10.1016/j.surfcoat.2010.08.077.

[30] K. Venkatakrishna, A.C. Hegde, Electrolytic preparation of cyclic multilayer Zn-Ni alloy coating using switching cathode current densities, J. Appl. Electrochem. 40 (2010) 2051–2059. doi:10.1007/s10800-010-0186-7.

[31] S. Yogesha, A. Chitharanjan Hegde, Optimization of deposition conditions for development of high corrosion resistant Zn–Fe multilayer coatings, J. Mater. Process. Technol. 211 (2011) 1409–1415. doi:10.1016/j.jmatprotec.2011.03.010.

[32] W. Lauwerens, A. De Boeck, M. Thijs, S. Claessens, M. Van Stappen, P. Steenackers, PVD Al-Ti and Al-Mn coatings for high temperature corrosion protection of sheet steel, Surf. Coat. Technol. 146 (2001) 27–32. doi:10.1016/S0257-8972(01)01468-2.

[33] H.C. Barshilia, M.S. Prakash, A. Poojari, K.S. Rajam, Corrosion behavior of nanolayered TiN/NbN multilayer coatings prepared by reactive direct current magnetron sputtering process, Thin Solid Films. 460 (2004) 133–142. doi:10.1016/j.tsf.2004.01.096.

[34] C. Wagner, Theoretical Analysis of the Current Density Distribution in Electrolytic Cells, J. Electrochem. Soc. 98 (1951) 116–128. doi:10.1149/1.2778113.

[35] X.G. Zhang, E.M. Valeriote, Galvanic protection of steel and galvanic corrosion of zinc under thin layer electrolytes, Corros. Sci. 34 (1993) 1957–1972. doi:10.1016/0010-938X(93)90053-J.
[36] K. Ogle, V. Baudu, L. Garrigues, X. Philippe, Localized Electrochemical Methods Applied to Cut Edge Corrosion, J. Electrochem. Soc. 147 (2000) 3654–3660. doi:10.1149/1.1393954.
[37] E. Tada, K. Sugawara, H. Kaneko, Distribution of pH during galvanic corrosion of a Zn/steel couple, Electrochimica Acta. 49 (2004) 1019–1026. doi:10.1016/j.electacta.2003.10.012.
[38] J. Waber, M. Rosenbluth, Mathematical Studies of Galvanic Corrosion .2. Coplanar Electrodes with One Electrode Infinitely Large and with Equal Polarization Parameters, J. Electrochem. Soc. 102 (1955) 344–353. doi:10.1149/1.2430058.
[39] E. Kennard, J. Waber, Mathematical Study of Galvanic Corrosion - Equal Coplanar Anode and Cathode with Unequal Polarization Parameters, J. Electrochem. Soc. 117 (1970) 880–&. doi:10.1149/1.2407662.
[40] E. McCafferty, Distribution of Potential and Current in Circular Corrosion Cells Having Unequal Polarization Parameters, J. Electrochem. Soc. 124 (1977) 1869–1878. doi:10.1149/1.2133178.
[41] S. Aoki, K. Kishimoto, Prediction of Galvanic Corrosion Rates by the Boundary Element Method, Math. Comput. Model. 15 (1991) 11–22. doi:10.1016/0895-7177(91)90049-D.
[42] J.M. Lee, Numerical analysis of galvanic corrosion of Zn/Fe interface beneath a thin electrolyte, Electrochimica Acta. 51 (2006) 3256–3260. doi:10.1016/j.electacta.2005.09.026.
[43] P. Doig, P.E.J. Flewitt, A Finite Difference Numerical Analysis of Galvanic Corrosion for Semi-Infinite Linear Coplanar Electrodes, J. Electrochem. Soc. 126 (1979) 2057–2063. doi:10.1149/1.2128861.
[44] C.R. Crowe, R.G. Kasper, Ionic Current Densities in the Nearfield of a Corroding Iron-Copper Galvanic Couple, J. Electrochem. Soc. 133 (1986) 879–887.
[45] S.G.R. Brown, N.C. Barnard, 3D computer simulation of the influence of microstructure on the cut edge corrosion behaviour of a zinc aluminium alloy galvanized steel, Corros. Sci. 48 (2006) 2291–2303. doi:10.1016/j.corsci.2005.08.015.
[46] N.C. Barnard, S.G.R. Brown, Modelling the relationship between microstructure of Galfan-type coated steel and cut-edge corrosion resistance incorporating diffusion of multiple species, Corros. Sci. 50 (2008) 2846–2857. doi:10.1016/j.corsci.2008.07.005.
[47] F. Thébault, B. Vuillemin, R. Oltra, K. Ogle, C. Allely, Investigation of self-healing mechanism on galvanized steels cut edges by coupling SVET and numerical modeling, Electrochimica Acta. 53 (2008) 5226–5234. doi:10.1016/j.electacta.2008.02.066.
[48] F. Thébault, B. Vuillemin, R. Oltra, C. Allely, K. Ogle, Reliability of numerical models for simulating galvanic corrosion processes, Electrochimica Acta. 82 (2012) 349–355. doi:10.1016/j.electacta.2012.04.068.
[49] K.B. Deshpande, Experimental investigation of galvanic corrosion: Comparison between SVET and immersion techniques, Corros. Sci. 52 (2010) 2819–2826. doi:10.1016/j.corsci.2010.04.023.
[50] M.S. Venkatraman, I.S. Cole, B. Emmanuel, Model for corrosion of metals covered with thin electrolyte layers: Pseudo-steady state diffusion of oxygen, Electrochimica Acta. 56 (2011) 7171–7179. doi:10.1016/j.electacta.2011.05.009.
[51] S.K. Thamida, Modeling and simulation of galvanic corrosion pit as a moving boundary problem, Comput. Mater. Sci. 65 (2012) 269–275. doi:10.1016/j.commatsci.2012.07.029.
[52] W. Sun, L. Wang, T. Wu, G. Liu, An arbitrary Lagrangian–Eulerian model for modelling the time-dependent evolution of crevice corrosion, Corros. Sci. (n.d.). doi:10.1016/j.corsci.2013.10.003.
[53] F. Thébault, B. Vuillemin, R. Oltra, C. Allely, K. Ogle, Protective mechanisms occurring on zinc coated steel cut-edges in immersion conditions, Electrochimica Acta. 56 (2011) 8347–8357. doi:10.1016/j.electacta.2011.07.016.

[54] J. Elvins, J.A. Spittle, D.A. Worsley, Microstructural changes in zinc aluminium alloy galvanising as a function of processing parameters and their influence on corrosion, Corros. Sci. 47 (2005) 2740–2759. doi:10.1016/j.corsci.2004.11.011.

[55] Y. Tan, Understanding the effects of electrode inhomogeneity and electrochemical heterogeneity on pitting corrosion initiation on bare electrode surfaces, Corros. Sci. 53 (2011) 1845–1864. doi:10.1016/j.corsci.2011.02.002.

[56] P. Pistorius, G. Burstein, Growth of Corrosion Pits on Stainless-Steel in Chloride Solution Containing Dilute Sulfate, Corros. Sci. 33 (1992) 1885–1897. doi:10.1016/0010-938X(92)90191-5.

[57] G.S. Frankel, Pitting Corrosion of Metals A Review of the Critical Factors, J. Electrochem. Soc. 145 (1998) 2186–2198. doi:10.1149/1.1838615.

[58] Z. Szklarska-Smialowska, Fitting corrosion of aluminum, Corros. Sci. 41 (1999) 1743–1767. doi:10.1016/S0010-938X(99)00012-8.

[59] E. McCafferty, Sequence of steps in the pitting of aluminum by chloride ions, Corros. Sci. 45 (2003) 1421–1438. doi:10.1016/S0010-938X(02)00231-7.

[60] G.T. Burstein, G.O. Ilevbare, The effect of specimen size on the measured fitting potential of stainless steel, Corros. Sci. 38 (1996) 2257–2265. doi:10.1016/S0010-938X(97)83146-0.

[61] T. Suter, H. Bohni, Microelectrodes for studies of localized corrosion processes, Electrochimica Acta. 43 (1998) 2843–2849. doi:10.1016/S0013-4686(98)00025-5.

[62] T. Shibata, T. Takeyama, Stochastic Theory of Pitting Corrosion, Corrosion. 33 (1977) 243–251. doi:10.5006/0010-9312-33.7.243.

[63] D. Williams, C. Westcott, M. Fleischmann, Stochastic-Models of Pitting Corrosion of Stainless-Steels .1. Modeling, J. Electrochem. Soc. 132 (1985) 1796–1804. doi:10.1149/1.2114220.

[64] S. Sharland, A Review of the Theoretical Modeling of Crevice and Pitting Corrosion, Corros. Sci. 27 (1987) 289–323. doi:10.1016/0010-938X(87)90024-2.

[65] B. Baroux, The kinetics of pit generation on stainless steels, Corros. Sci. 28 (1988) 969–986. doi:10.1016/0010-938X(88)90015-7.

[66] A. Valor, F. Caleyo, L. Alfonso, D. Rivas, J.M. Hallen, Stochastic modeling of pitting corrosion: A new model for initiation and growth of multiple corrosion pits, Corros. Sci. 49 (2007) 559–579. doi:10.1016/j.corsci.2006.05.049.

[67] N. Murer, R.G. Buchheit, Stochastic modeling of pitting corrosion in aluminum alloys, Corros. Sci. 69 (2013) 139–148. doi:10.1016/j.corsci.2012.11.034.

[68] S.M. Sharland, C.P. Jackson, A.J. Diver, A finite-element model of the propagation of corrosion crevices and pits, Corros. Sci. 29 (1989) 1149–1166. doi:10.1016/0010-938X(89)90051-6.

[69] J. Harb, R. Alkire, Transport and Reaction During Pitting Corrosion of Ni in 0.5m Nacl .1. Stagnant Fluid, J. Electrochem. Soc. 138 (1991) 2594–2600. doi:10.1149/1.2086022.

[70] N.J. Laycock, S.P. White, Computer Simulation of Single Pit Propagation in Stainless Steel under Potentiostatic Control, J. Electrochem. Soc. 148 (2001) B264–B275. doi:10.1149/1.1376119.

[71] N.J. Laycock, J.S. Noh, S.P. White, D.P. Krouse, Computer simulation of pitting potential measurements, Corros. Sci. 47 (2005) 3140–3177. doi:10.1016/j.corsci.2005.07.003.

[72] J. Xiao, S. Chaudhuri, Predictive modeling of localized corrosion: An application to aluminum alloys, Electrochimica Acta. 56 (2011) 5630–5641. doi:10.1016/j.electacta.2011.04.019.

[73] M. Baumgartner, H. Kaesche, Aluminum Pitting in Chloride Solutions - Morphology and Pit Growth-Kinetics, Corros. Sci. 31 (1990) 231–236. doi:10.1016/0010-938X(90)90112-I.

[74] S.-J. Pan, W.-T. Tsai, J.-K. Chang, I.-W. Sun, Co-deposition of Al-Zn on AZ91D magnesium alloy in AlCl3-1-ethyl-3-methylimidazolium chloride ionic liquid, Electrochimica Acta. 55 (2010) 2158–2162. doi:10.1016/j.electacta.2009.11.050.

[75] S.-J. Pan, W.-T. Tsai, I.-W. Sun, Electrodeposition of Al–Zn on Magnesium Alloy from ZnCl2-Containing Ionic Liquids, Electrochem. Solid-State Lett. 13 (2010) D69–D71. doi:10.1149/1.3447842.

[76] S. Ruan, C.A. Schuh, Electrodeposited Al-Mn alloys with microcrystalline, nanocrystalline, amorphous and nano-quasicrystalline structures, Acta Mater. 57 (2009) 3810–3822. doi:10.1016/j.actamat.2009.04.030.

[77] N. Peng, Y. He, H. Song, X. Yang, X. Cai, Effects of electrodeposited Zn nuclei on tunnel etching behavior of aluminum foil, Corros. Sci. 91 (2015) 213–219. doi:10.1016/j.corsci.2014.11.023.

[78] W. Chen, Q. Liu, Q. Liu, L. Zhu, L. Wang, A combinatorial study of the corrosion and mechanical properties of Zn–Al material library fabricated by ion beam sputtering, J. Alloys Compd. 459 (2008) 261–266. doi:10.1016/j.jallcom.2007.05.046.

[79] A. Bakkar, V. Neubert, Electrodeposition and corrosion characterisation of micro- and nano-crystalline aluminium from AlCl3/1-ethyl-3-methylimidazolium chloride ionic liquid, Electrochimica Acta. 103 (2013) 211–218. doi:10.1016/j.electacta.2013.03.198.

[80] J. Fei, G.D. Wilcox, Electrodeposition of zinc–nickel compositionally modulated multilayer coatings and their corrosion behaviours, Surf. Coat. Technol. 200 (2006) 3533–3539. doi:10.1016/j.surfcoat.2004.08.183.

[81] M. Rahsepar, M.E. Bahrololoom, Corrosion study of Ni/Zn compositionally modulated multilayer coatings using electrochemical impedance spectroscopy, Corros. Sci. 51 (2009) 2537–2543. doi:10.1016/j.corsci.2009.06.030.

[82] K.G. Boto, L.F.G. Williams, Rotating disc electrode studies of zinc corrosion, J. Electroanal. Chem. Interfacial Electrochem. 77 (1977) 1–20. doi:10.1016/S0022-0728(77)80315-X.

[83] V. Jovancicevic, J.O. Bockris, The Mechanism of Oxygen Reduction on Iron in Neutral Solutions, J. Electrochem. Soc. 133 (1986) 1797–1807.

[84] Tomas Prosek, Dominique Thierry, Claes Taxen, Jaroslav Maixner, Effect of cations on corrosion of zinc and carbon steel covered with chloride deposits under atmospheric conditions, Corros. Sci. 49 (2007) 2676–2693.

[85] K.R. Baldwin, M.J. Robinson, C.J.E. Smith, Corrosion rate measurements of electrodeposited zinc-nickel alloy coatings, Corros. Sci. 36 (1994) 1115–1131. doi:10.1016/0010-938X(94)90137-6.

[86] S.C. Dexter, Handbook of Oceanographic Engineering Materials, John Wiley & Sons, New York, NY, 1979.

[87] L.Y. Xu, X. Su, Y.F. Cheng, Effect of alternating current on cathodic protection on pipelines, Corros. Sci. 66 (2013) 263–268. doi:10.1016/j.corsci.2012.09.028.

[88] R. Sa-nguanmoo, E. Nisaratanaporn, Y. Boonyongmaneerat, Hot-dip galvanization with pulse-electrodeposited nickel pre-coatings, Corros. Sci. 53 (2011) 122–126. doi:10.1016/j.corsci.2010.09.031.

[89] E. Gazi, W.D. Seider, L.H. Ungar, A non-parametric Monte Carlo technique for controller verification, Automatica. 33 (1997) 901–906. doi:10.1016/S0005-1098(96)00227-0.

[90] S. Kirkpatrick, C.D. Gelatt, M.P. Vecchi, Optimization by Simulated Annealing, Science. 220 (1983) 671–680. doi:10.1126/science.220.4598.671.

[91] V. Černý, Thermodynamical approach to the traveling salesman problem: An efficient simulation algorithm, J. Optim. Theory Appl. 45 (1985) 41–51. doi:10.1007/BF00940812.

[92] N. Cretu, M.-I. Pop, Acoustic behavior design with simulated annealing, Comput. Mater. Sci. 44 (2009) 1312–1318. doi:10.1016/j.commatsci.2008.08.023.

[93] L. Lamberti, An efficient simulated annealing algorithm for design optimization of truss structures, Comput. Struct. 86 (2008) 1936–1953. doi:10.1016/j.compstruc.2008.02.004.

[94] V.M.F. Correia, C.M. Mota Soares, C.A. Mota Soares, Refined models for the optimal design of adaptive structures using simulated annealing, Compos. Struct. 54 (2001) 161–167. doi:10.1016/S0263-8223(01)00085-X.
[95] J.M. Simões Moita, V.M. Franco Correia, P.G. Martins, C.M. Mota Soares, C.A. Mota Soares, Optimal design in vibration control of adaptive structures using a simulated annealing algorithm, Compos. Struct. 75 (2006) 79–87. doi:10.1016/j.compstruct.2006.04.062.
[96] J.V. Martí, F. Gonzalez-Vidosa, V. Yepes, J. Alcalá, Design of prestressed concrete precast road bridges with hybrid simulated annealing, Eng. Struct. 48 (2013) 342–352. doi:10.1016/j.engstruct.2012.09.014.
[97] S. Bureerat, J. Limtragool, Structural topology optimisation using simulated annealing with multiresolution design variables, Finite Elem. Anal. Des. 44 (2008) 738–747. doi:10.1016/j.finel.2008.04.002.
[98] J.R. Medina, Estimation of incident and reflected waves using simulated annealing, J. Waterw. Port Coast. Ocean Eng.-Asce. 127 (2001) 213–221. doi:10.1061/(ASCE)0733-950X(2001)127:4(213).
[99] S.R. Cross, R. Woollam, S. Shademan, C.A. Schuh, Computational Design and Optimization of Multilayered and Functionally Graded Corrosion Coatings, Corros. Sci. (n.d.). doi:10.1016/j.corsci.2013.08.018.
[100] M. Stern, The Electrochemical Behavior, Including Hydrogen Overvoltage, of Iron in Acid Environments, J. Electrochem. Soc. 102 (1955) 609–616. doi:10.1149/1.2429923.
[101] A. Makrides, Dissolution of Iron in Sulfuric Acid and Ferric Sulfate Solutions, J. Electrochem. Soc. 107 (1960) 869–877. doi:10.1149/1.2427532.
[102] F. Thebault, B. Vuillemin, R. Oltra, C. Allely, K. Ogle, Protective mechanisms occurring on zinc coated steel cut-edges in immersion conditions, Electrochimica Acta. 56 (2011) 8347–8357.
[103] C.F. Baes, R.E. Mesmer, The Hydrolysis of Cations, John Wiley & Sons, 1976.
[104] A. Davydov, K.V. Rybalka, L.A. Beketaeva, G.R. Engelhardt, P. Jayaweera, D.D. Macdonald, The kinetics of hydrogen evolution and oxygen reduction on Alloy 22, Corros. Sci. 47 (2005) 195–215. doi:10.1016/j.corsci.2004.05.005.
[105] M. Pourbaix, Atlas of electrochemical equilibria in aqueous solutions, NACE, 1974.
[106] O. Guseva, P. Schmutz, T. Suter, O. von Trzebiatowski, Modelling of anodic dissolution of pure aluminium in sodium chloride, Electrochimica Acta. 54 (2009) 4514–4524. doi:10.1016/j.electacta.2009.03.048.
[107] J. Creus, H. Mazille, H. Idrissi, Porosity evaluation of protective coatings onto steel, through electrochemical techniques, Surf. Coat. Technol. 130 (2000) 224–232. doi:10.1016/S0257-8972(99)00659-3.
[108] I. Kirilova, I. Ivanov, Corrosion behaviour of Zn-Co compositionally modulated multilayers electrodeposited from single and dual baths, J. Appl. Electrochem. 29 (1999) 1133–1137. doi:10.1023/A:1003675216529.
[109] A. Maciej, G. Nawrat, W. Simka, J. Piotrowski, Formation of compositionally modulated Zn–Ni alloy coatings on steel, Mater. Chem. Phys. 132 (2012) 1095–1102. doi:10.1016/j.matchemphys.2011.12.074.
[110] Z. Hashin, S. Shtrikman, On Some Variational Principles in Anisotropic and Nonhomogeneous Elasticity, J. Mech. Phys. Solids. 10 (1962) 335–342. doi:10.1016/0022-5096(62)90004-2.
[111] P.P. Castañeda, The effective mechanical properties of nonlinear isotropic composites, J. Mech. Phys. Solids. 39 (1991) 45–71. doi:10.1016/0022-5096(91)90030-R.
[112] J.C. Michel, H. Moulinec, P. Suquet, Effective properties of composite materials with periodic microstructure: a computational approach, Comput. Methods Appl. Mech. Eng. 172 (1999) 109–143. doi:10.1016/S0045-7825(98)00227-8.

[113] A.P. Roberts, E.J. Garboczi, Elastic Properties of Model Porous Ceramics, J. Am. Ceram. Soc. 83 (2000) 3041–3048. doi:10.1111/j.1151-2916.2000.tb01680.x.

[114] Y.J. Liu, X.L. Chen, Evaluations of the effective material properties of carbon nanotube-based composites using a nanoscale representative volume element, Mech. Mater. 35 (2003) 69–81. doi:10.1016/S0167-6636(02)00200-4.

[115] G.D. Seidel, D.C. Lagoudas, Micromechanical analysis of the effective elastic properties of carbon nanotube reinforced composites, Mech. Mater. 38 (2006) 884–907. doi:10.1016/j.mechmat.2005.06.029.

[116] P.P. Camanho, C.G. Davila, M.F. de Moura, Numerical simulation of mixed-mode progressive delamination in composite materials, J. Compos. Mater. 37 (2003) 1415–1438. doi:10.1177/002199803034505.

[117] Z. Zou, S.R. Reid, S. Li, A continuum damage model for delaminations in laminated composites, J. Mech. Phys. Solids. 51 (2003) 333–356. doi:10.1016/S0022-5096(02)00075-3.

[118] B.R. Hinderliter, S.G. Croll, D.E. Tallman, Q. Su, G.P. Bierwagen, Interpretation of EIS data from accelerated exposure of coated metals based on modeling of coating physical properties, Electrochimica Acta. 51 (2006) 4505–4515. doi:10.1016/j.electacta.2005.12.047.

[119] S. Kirkpatrick, Classical Transport in Disordered Media: Scaling and Effective-Medium Theories, Phys. Rev. Lett. 27 (1971) 1722–1725. doi:10.1103/PhysRevLett.27.1722.

[120] D.E. Aspnes, J.B. Theeten, F. Hottier, Investigation of effective-medium models of microscopic surface roughness by spectroscopic ellipsometry, Phys. Rev. B. 20 (1979) 3292–3302. doi:10.1103/PhysRevB.20.3292.

[121] M. Bendsoe, N. Kikuchi, Generating Optimal Topologies in Structural Design Using a Homogenization Method, Comput. Methods Appl. Mech. Eng. 71 (1988) 197–224. doi:10.1016/0045-7825(88)90086-2.

[122] O. Sigmund, On the design of compliant mechanisms using topology optimization, Mech. Struct. Mach. 25 (1997) 493–524. doi:10.1080/08905459708945415.

[123] S. Pride, J. Scully, J. Hudson, Metastable Pitting of Aluminum and Criteria for the Transition to Stable Pit Growth, J. Electrochem. Soc. 141 (1994) 3028–3040. doi:10.1149/1.2059275.

[124] E. Mccafferty, The Electrode-Kinetics of Pit Initiation on Aluminum, Corros. Sci. 37 (1995) 481–492. doi:10.1016/0010-938X(94)00150-5.

[125] B. Zaid, D. Saidi, A. Benzaid, S. Hadji, Effects of pH and chloride concentration on pitting corrosion of AA6061 aluminum alloy, Corros. Sci. 50 (2008) 1841–1847. doi:10.1016/j.corsci.2008.03.006.

[126] G.S. Frankel, J.R. Scully, C.V. Jahnes, Repassivation of pits in aluminum thin films, J. Electrochem. Soc. 143 (1996) 1834–1840. doi:10.1149/1.1836912.

[127] M.P. Ryan, N.J. Laycock, H.S. Isaacs, R.C. Newman, Corrosion pits in thin films of stainless steel, J. Electrochem. Soc. 146 (1999) 91–97. doi:10.1149/1.1391569.

[128] L. Balázs, J.-F. Gouyet, Two-dimensional pitting corrosion of aluminium thin layers, Phys. Stat. Mech. Its Appl. 217 (1995) 319–338. doi:10.1016/0378-4371(95)00048-C.

[129] T.A. Lowe, G.G. Wallace, A.K. Neufeld, Insights into the cut edge corrosion of 55% Al-Zn metal coating on steel from simultaneous electrochemical polarization and localised pH sensing experiments, Corros. Sci. 55 (2012) 180–186. doi:10.1016/j.corsci.2011.10.015.